2014

Multifrequency Averaging in Power Electronic Systems

Fei Pan
University of Kentucky, feipanengineer@gmail.com

STUDENT AGREEMENT:

I represent that my thesis or dissertation and abstract are my original work. Proper attribution has been given to all outside sources. I understand that I am solely responsible for obtaining any needed copyright permissions. I have obtained needed written permission statement(s) from the owner(s) of each third-party copyrighted matter to be included in my work, allowing electronic distribution (if such use is not permitted by the fair use doctrine) which will be submitted to UKnowledge as Additional File.

I hereby grant to The University of Kentucky and its agents the irrevocable, non-exclusive, and royalty-free license to archive and make accessible my work in whole or in part in all forms of media, now or hereafter known. I agree that the document mentioned above may be made available immediately for worldwide access unless an embargo applies.

I retain all other ownership rights to the copyright of my work. I also retain the right to use in future works (such as articles or books) all or part of my work. I understand that I am free to register the copyright to my work.

REVIEW, APPROVAL AND ACCEPTANCE

The document mentioned above has been reviewed and accepted by the student's advisor, on behalf of the advisory committee, and by the Director of Graduate Studies (DGS), on behalf of the program; we verify that this is the final, approved version of the student's thesis including all changes required by the advisory committee. The undersigned agree to abide by the statements above.

Fei Pan, Student

Dr. Aaron M. Cramer, Major Professor

Dr. Cai-Cheng Lu, Director of Graduate Studies

MULTIFREQUENCY AVERAGING IN POWER ELECTRONIC SYSTEMS

DISSERTATION

A dissertation submitted in partial fulfillment of the requirement
for the degree of Doctor of Philosophy in Electrical Engineering
in the College of Engineering at the University of Kentucky

By

Fei Pan

Lexington, Kentucky

Co-Directors: Dr. Aaron M. Cramer, Assistant Professor of Electrical Engineering
and Dr. Bruce L. Walcott, Professor of Electrical Engineering

Lexington, Kentucky

2014

ABSTRACT OF DISSERTATION

MULTIFREQUENCY AVERAGING IN POWER ELECTRONIC SYSTEMS

Power electronic systems have been widely used in the electrical power processing for applications with power levels ranging from less than one watt in battery-operated portable devices to more than megawatts in the converters, inverters and rectifiers of the utility power systems. These systems typically involve the passive elements such as inductors, capacitors, and resistors, the switching electronic components such as IGBTs, MOSFETS, and diodes, and other electronic circuits. Multifrequency averaging is one of the widely used modeling and simulation techniques today for the analysis and design of power electronic systems. This technique is capable of providing the average behavior as well as the ripple behavior of power electronic systems. This work begins with the extension of multifrequency averaging to represent uniformly sampled PWM converters. A new multifrequency averaging method of solving an observed issue with model stability is proposed and validated. Multifrequency averaging can also be applied to study the instability phenomenon in power electronic systems. In particular, a reduced-order multifrequency averaging method, along with a genetic algorithm based procedure, is proposed in this work to estimate the regions of attraction of power electronic converters. The performance of this method is shown by comparing the accuracy and efficiency with the existing methods. Finally, a new continuous-time multifrequency averaging method of representing discrete-time systems is proposed. The proposed method is applied to model digitally controlled PWM converters. Simulation and hardware results show that the proposed method is capable of predicting the average behavior as well as the ripple behavior of the closed-loop systems. Future research in the area of multifrequency averaging is proposed.

KEYWORDS: Digital Control, Modeling, Power Electronic Systems,
Pulse Width Modulation, Stability

Fei Pan

Student's Signature

December 1st, 2014

Date

MULTIFREQUENCY AVERAGING IN POWER ELECTRONIC SYSTEMS

By

Fei Pan

Aaron M. Cramer
Co-Director of Dissertation

Bruce L. Walcott
Co-Director of Dissertation

Caicheng Lu
Director of Graduate Studies

December 1st, 2014

This dissertation is gratefully dedicated to my wife, Xinyue Gu.

ACKNOWLEDGEMENTS

I would like to thank my co-directors, Prof. Cramer and Prof. Walcott, for their most valuable guidance, encouragement, academic stimulus and generous help in this work. I am sincerely grateful to Dr. Loop for sharing his truthful and illuminating views on a number of issues related to the work. I would also like to show my gratitude to my committee members, Prof. Liao, Prof. Sottile and Prof. Lineberry, for their support and guidance on this work. My gratitude also goes to some of my colleagues, Hanling Chen, Mengmei Liu, Xiao Liu, Jing Shang and Yingying Liu. Their involvement in the experiment offers me convenience for this work. Finally, but definitely not the least, I owe sincere and earnest thankfulness to my dear wife, Xinyue Gu. This work would not have been possible without her support.

TABLE OF CONTENTS

LIST OF TABLES

LIST OF FIGURES

CHAPTER 1

INTRODUCTION

Power electronic systems have been widely used in the electrical power processing for applications with power levels ranging from less than one watt in battery-operated portable devices [1–5] to more than megawatts in the converters, inverters and rectifiers of the utility power systems [6–11]. These systems typically involve the passive elements such as inductors, capacitors, and resistors, the switching electronic components such as IGBTs, MOSFETS, and diodes, and other electronic circuits.

Previous work on the modeling and simulation has focused on the detailed models of power electronic systems (e.g., detailed switch-level models of PWM power electronic converters). These models (discrete-time models or continuous-time models) represent the on-off behavior of switching elements explicitly. They accurately describe the operation of the power electronic systems but generally require relatively long simulation run times (compared to averaged models) because the simulation time step is limited by the switching period. Also, the detailed models do not have constant equilibrium. Averaged models are time-invariant models that portray the average behavior of the power electronic systems without requiring excessive run times and have constant equilibrium. Such models have traditionally been constructed using state-space averaging method [12–15]. However, the successful application of such models has been limited to power electronic systems that satisfy a small ripple assumption (e.g., [16, 17]).

Herein, the multifrequency averaging, as one of the widely used modeling and simulation techniques today [18–29], is studied for the analysis and design of power electronic systems. The fundamental idea is to represent the state variables of power electronic systems using a truncated Fourier series [30]. This technique is capable

of providing the average behavior as well as the ripple behavior of power electronic systems.

This work begins with the extension of multifrequency averaging to representing uniformly sampled pulse-width-modulated (PWM) converters. In the past, multifrequency averaging has been studied for naturally sampled PWM where the modulation signal is compared with a sawtooth (or other carrier) signal to produce the gate control switching signal for the power electronic systems. In this setting, an algebraic equation must be solved at each time step. The approaches to solve for the switching time at which the modulation signal crosses the sawtooth carrier in each switching cycle are presented in [20, 24]. However, the switching times remain implicit and cannot be solved directly in these approaches. Uniformly sampled PWM implementation has attracted increasing interest because of the ease of digital implementation (e.g., [31–33]). Compared with analog implementations, digital implementations have lower sensitivity to parameter variation, higher design flexibility, and better communication capability [34–39]. The modulation signal in uniformly sampled PWM is sampled at the beginning of each switching period, and the sampled value is compared with the carrier signal. In this setting, the switching times do not depend on the ripple of the natural modulation signal explicitly; rather, it depends on what the value of the modulation signal at the beginning of the switching period. In this work, a method of representing uniformly sampled PWM converters using multifrequency averaging is proposed. The proposed method also addresses a numerical stability issue that is observed in multifrequency averaging representations of integrators. An associated solution is then developed to achieve stabilized integrators. The proposed method is demonstrated in simulation studies and validated experimentally using a uniformly sampled PWM buck converter. It is shown that the proposed method is capable of predicting the transient and steady-state behavior predicted by the detailed model.

To analyze the large-signal stability of nonlinear power electronic systems, it is necessary to set forth an effective method to estimate the region of attraction. The region of attraction is defined as a region for which all system trajectories starting within the region asymptotically approach the equilibrium point. Lyapunov techniques have been used to search for region of attraction estimates of power electronic systems [40–44]. These approaches rely on evaluating the values of carefully chosen scalar functions (Lyapunov functions) on state-space averaging models without numerically integrating the system trajectories. The state-space averaging models are capable of portraying the average behavior of power electronic systems. However, the small ripple assumption inherent to state-space averaging models can limit the applicability of these models. In this work, a reduced-order multifrequency averaging method is proposed to perform region of attraction estimation using Lyapunov techniques. The proposed reduced-order multifrequency averaging method is capable of representing the effects of switching ripple on the behavior of the system and is, therefore, more capable of predicting the influence of the switching ripple on the stability of the system. The proposed method in performing region of attraction estimation using Lyapunov techniques is demonstrated in simulation studies and validated experimentally using a naturally sampled PWM converter with constant power load. The use of the proposed models for region of attraction estimation is found to be more accurate than the use of state-space averaging models for power electronic converters in which the switching ripple is not negligible.

Discrete-time models have already been studied for the nonlinear dynamics of the discrete-time power electronic systems (e.g, digitally controlled PWM converters) [45–50]. These discrete-time approaches carefully describe the nonlinear dynamics but generally require long simulation run times (compared with averaged models) because the simulation time step of the discrete-time models is limited by the sampling period or the switching period. Continuous-time state-space averaged

models are capable of portraying the average behavior of the nonlinear dynamics of the discrete-time systems [51–55]. These approaches rely on the s-domain models of the discrete-time systems directly via approximation transformations (e.g., forward or backward Euler, bilinear). The resultant averaged models have been limited to discrete-time systems that satisfy a small ripple assumption. To describe the average behavior as well as the low-order components of the ripple behavior of the discrete-time systems, a continuous-time multifrequency averaging representation of the discrete-time systems is proposed in this work. The proposed method relies on the discrete-time multifrequency averaging representation of the discrete-time systems and approximation transformations (e.g., forward or backward Euler, bilinear) from discrete-time models to continuous-time models. The proposed method is demonstrated in simulation studies and validated experimentally using a digitally controlled PWM converter. It is shown that the proposed method is capable of predicting the transient and steady-state behavior predicted by the detailed model.

1.1 Applications of Dissertation

In this work, the multifrequency averaging method is extended to model and simulate uniformly sampled PWM converters and digitally controlled PWM converters. It is noted that the studies considered herein are for buck converters and that the results could be applied equally to other power electronic systems or even to other systems that exhibit periodic oscillation in steady state. The extension of the multifrequency averaging method makes the modeling and simulation of complicated power electronic systems highly accurate (compared to state-space averaged models) while highly numerically efficient (compared to detailed models). It helps designers gain better understanding of circuit operation, select appropriate circuit component types and values, choose control topologies, and estimate circuit performance. Further, the multifrequency averaging is applied to study the instability phenomenon in power

electronic systems. In particular, a reduced-order multifrequency averaging method, along with a genetic algorithm based procedure, is proposed in this work to estimate the regions of attraction of power electronic systems. Such a procedure provides the region of attraction estimates with sufficient accuracy and efficiency, rather than working directly with detailed models. It helps design power electronic systems with high robustness and reliability, where the circuit performance will meet specifications even with anticipated perturbations in operation conditions.

1.2 Organization of Dissertation

The organization of the dissertation is as follows. The background and literature review are presented in Chapter 2. A multifrequency averaging method for representing uniformly sampled PWM converters is proposed in Chapter 3. A reduced-order multifrequency averaging method is proposed in Chapter 4 to perform region of attraction estimation using Lyapunov techniques. A method of continuous-time multifrequency averaging representation of discrete-time systems is proposed in Chapter 5 and is used to model digitally controlled PWM converters. A concluding summary and areas of future work are provided in Chapter 6. The results of stability analysis in Chapter 3 are provided in Appendices A–B. The mixed-Kronecker-product property that is useful for deriving the continuous-time multifrequency averaging representation of discrete-time systems in Chapter 5 is proved in Appendix C. The hardware prototype used for the experimental validations of this work is described in Appendix D.

CHAPTER 2

BACKGROUND AND LITERATURE REVIEW

In this chapter, background information related to this work is presented, and related literature is reviewed. The remainder of this chapter is organized as follows. The state-space averaging method for modeling power electronic systems is introduced in Section 2.1. It is followed by Section 2.2 in which the multifrequency averaging method is introduced and several properties of partial-Fourier-series are described. For comparison, discrete-time models are described in Section 2.3. The structures and schemes of feedback control are presented in Section 2.4. Stability in power electronic systems is briefly introduced in Section 2.5.

2.1 State-Space Averaging

Power electronic systems typically involve the passive elements such as inductors, capacitors, and resistors, the switching electronic components such as IGBTs, MOSFETS, and diodes, and other electronic circuits. Detailed switch-level models of power electronic systems represent the on-off behavior of the switching elements explicitly. Such models can be discrete-time models or continuous-time models. They accurately describe the operation of power electronic systems but generally require relatively long run times (compared to averaged models) because the simulation time step is limited by the switching period. Also, the detailed models do not have constant equilibrium points.

The state-space averaged (SSA) models are simplified approximate models exacted from the detailed models through averaging over one switching cycle [12, 13]. Such models are time-invariant models that portray the average behavior of the power electronic systems without requiring excessive run times and have constant equilibrium points.

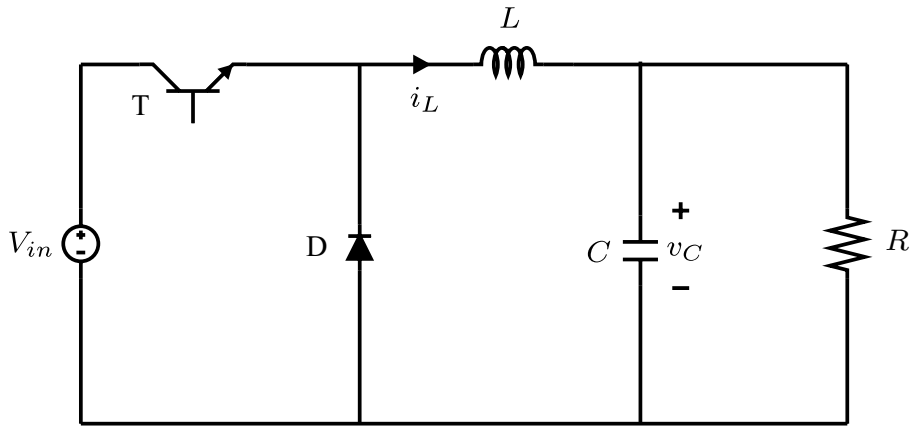

Figure 2.1: A simple buck converter.

Herein, a simple open-loop buck converter shown in Figure 2.1 is used to illustrate the SSA method. It is assumed that the buck converter is operating in continuous conduction mode, i.e., one and only one of the switches are conducting at all times. The detailed model of the buck converter is given as

$$L\frac{di_L}{dt} = qV_{in} - v_C \tag{2.1}$$

$$C\frac{dv_C}{dt} = i_L - \frac{v_C}{R} \tag{2.2}$$

where q is the switching function that takes values of zero and one corresponding to the transistor being open (off) or closed (on). Without loss of generality, one set of differential equations can be constructed to describe the detailed model of the buck converter considering the on-off behavior of the transistor:

$$\dot{\mathbf{x}} = q(A_1\mathbf{x} + B_1\mathbf{u}) + (1-q)(A_2\mathbf{x} + B_2\mathbf{u}) \tag{2.3}$$

where state vector $\mathbf{x}$, input vector $\mathbf{u}$, state matrices A_1 and A_2, and input matrices B_1 and B_2 are given by the following, respectively,

$$\mathbf{x} = \begin{bmatrix} i_L & v_C \end{bmatrix}^{\mathrm{T}} \tag{2.4}$$

$$\mathbf{u} = \begin{bmatrix} V_{in} & 0 \end{bmatrix}^{\mathrm{T}} \tag{2.5}$$

$$A_1 = A_2 = \begin{bmatrix} 0 & -\frac{1}{L} \\ \frac{1}{C} & -\frac{1}{RC} \end{bmatrix} \tag{2.6}$$

$$B_1 = \begin{bmatrix} \frac{1}{L} & 0 \\ 0 & 0 \end{bmatrix} \tag{2.7}$$

$$B_2 = \begin{bmatrix} 0 & 0 \\ 0 & 0 \end{bmatrix}. \tag{2.8}$$

A lagged running average is defined in [56] to describe the percentage of "on-time" of the switching function $q(t)$ in each switching cycle T such that

$$d(t) = \frac{1}{T}\int_{t-T}^{T} q(\tau)d\tau \tag{2.9}$$

and $d(t)$ is referred to as the continuous duty cycle. Likewise, the local averages of $\mathbf{x}$ and $\mathbf{u}$ are defined in [56] as

$$\bar{\mathbf{x}} = \frac{1}{T}\int_{t-T}^{T} \mathbf{x}(\tau)d\tau \tag{2.10}$$

$$\bar{\mathbf{u}} = \frac{1}{T}\int_{t-T}^{T} \mathbf{u}(\tau)d\tau. \tag{2.11}$$

The SSA model which describes the average behavior is derived in [13] by averaging the detailed model (2.3), such that

$$\dot{\bar{\mathbf{x}}} = \overline{q(A_1\mathbf{x} + B_1\mathbf{u})} + \overline{(1-q)(A_2\mathbf{x} + B_2\mathbf{u})} \tag{2.12}$$

$$= (A_1 - A_2)\overline{q\mathbf{x}} + (B_1 - B_2)\overline{q\mathbf{u}} + A_2\bar{\mathbf{x}} + B_2\bar{\mathbf{u}}. \tag{2.13}$$

The average of a product (i.e., $\overline{q\mathbf{x}}$ and $\overline{q\mathbf{u}}$ in (2.13)) is generally not the product of the averages. Under reasonable assumptions [13], it is possible to approximate the averages such that

$$\overline{q\mathbf{x}} \approx \bar{q}\bar{\mathbf{x}} = d\bar{\mathbf{x}} \tag{2.14}$$

$$\overline{q\mathbf{u}} \approx \bar{q}\bar{\mathbf{u}} = d\bar{\mathbf{u}}. \tag{2.15}$$

These approximations lead to the simplification of the SSA model in (2.13)

$$\dot{\bar{\mathbf{x}}} = (A_1 - A_2)d\bar{\mathbf{x}} + (B_1 - B_2)d\bar{\mathbf{u}} + A_2\bar{\mathbf{x}} + B_2\bar{\mathbf{u}}. \tag{2.16}$$

Rearranging the above simplification into the standard linear continuous state-space expression results in the basic SSA model:

$$\dot{\bar{\mathbf{x}}} = (dA_1 + (1-d)A_2)\bar{\mathbf{x}} + (dB_1 + (1-d)B_2)\bar{\mathbf{u}}. \tag{2.17}$$

It can be simplified as

$$\dot{\bar{\mathbf{x}}} = \bar{A}\bar{\mathbf{x}} + \bar{B}\bar{\mathbf{u}}. \tag{2.18}$$

where the matrices $\bar{A}$ and $\bar{B}$ are defined by

$$\bar{A} = dA_1 + (1-d)A_2 \tag{2.19}$$

$$\bar{B} = dB_1 + (1-d)B_2. \tag{2.20}$$

If the switching function $q(t)$ is periodic with period T, then the continuous duty cycle $d(t)$ is fixed at a constant value D. The resultant SSA models are time-invariant and can be applied to solve for the steady-state equilibrium point by setting the derivatives in (2.18) to zero. The SSA models also lead to much more efficient simulations (compared to detailed models) of the power electronic systems without requiring excessive run times, because the simulation time step in not limited by the switching period in the time-invariant models.

The SSA models have been studied as a convenient starting point to analyze and design various nonlinear controllers in power electronic systems [51–53]. In [51], a Lyapunov-based control which relies on the SSA models of the switched power converters is proposed to design globally stabilizing controls that include adaptive schemes for handling uncertain nominal parameters. In [52], the SSA method is used for designing stabilizing nonlinear proportional-integral feedback controllers which regulate to a constant set-point value either the average output inductor current, the average input inductor current, or the average transfer capacitor voltage of pulse-width modulation controlled Ćuk converter. Several nonlinear control algorithms based on SSA models of the power converters are experimentally compared in [53] for real physical applications. Recently, the SSA models have been studied specifically to design and analyze discrete-time controllers (e.g., digital controllers) [54, 55]. These approaches start from the linearized model of the converter power stage and the continuous-time controller. The discrete-time model is derived form the SSA model of the controller using discretization approximations (e.g., forward or backward Euler, bilinear). However, these averaged models do not account for the influence of the modulators on the dynamics of the controllers. To address this problem, an alternative formulation of the SSA model is presented in [57]. This approach yields a linearized small-signal representation of the power converter circuit, where the on-time, as well as the off-time of the pulse-width modulation signal are treated as distinct control

inputs. However, the successful application of the SSA models has been limited to power electronic systems that satisfy a small ripple assumption (e.g., [16, 17]).

2.2 Multifrequency Averaging

It has been shown in the previous subsection that the small ripple assumption nature of the SSA models precludes their application to power electronic systems where large ripple may be exhibited (e.g., quasi-resonant converters [58]).

For analysis of power electronic systems exhibiting large ripple, a generalized state-space-averaging (GSSA) method is proposed in [30]. The fundamental idea is to represent state variables using a truncated Fourier series. This approach predicts the average behavior as well as low-order components of the ripple behavior and can be applied directly to a number of different types of power electronic systems. In [18], the GSSA method is applied to study the basic dc-dc topologies, such as the buck, boost, buck-boost and Ćuk. This approach is extended in [59] to modeling zero-current switching quasi-resonant buck converter and and zero-voltage switching quasi-resonant boost converter where the natural frequency of the quasi-resonant tank is of the same order as the switching frequency and large ripple may exhibit. GSSA method can also be applied to analyze complex power electronic systems, such as multiconverter dc power electronic systems [22, 60], three-phase inverters [61] and ac distribution systems [62].

Conceptually similar approaches to GSSA have been coined multifrequency averaging (MFA) and dynamic phasors. In [20], MFA takes into account interactions between harmonics and produces accurate estimates of the state variables in a boost converter. It also presents a method to condense the averaged models to lower order by exploiting certain structural features. MFA modeling is applied advantageously to a multiple-input buck-boost converter in [24]. Therein, the MFA modeling has been shown to be capable of capturing overall behavior, particularly in closed-loop cases

when duty cycle command ripple may be presented. This approach is extended in [29] by identifying and presenting a systematic set of rules to automatically construct the MFA model for any PWM dc-dc converter of an arbitrary order and complexity. This automatic approach can be used to develop computer programs that systematically generate high-accurate time-invariant models for PWM dc-dc converters. In [25], a linear time-invariant model of a single-phase four-quadrant PWM converter is derived based on MFA approach. The proposed model is shown to be applicable for direct calculation of steady-state equilibrium and small-signal analysis. Extensions of MFA method have also been applied to other power electronic systems, such as converters [28], inverters [26,27] and rectifiers [23]. Other studies involve the stability assessment of MFA models [21,63]. It is shown in [21] that an MFA model of a Ćuk converter, as well as other PWM converter topologies, with a fixed duty cycle and a finite switching frequency is asymptotically stable. In [63], by applying MFA, the feedback duty cycle is treated as a function of the open-loop duty cycle. This function indicates whether a stationary duty cycle exists in the closed-loop configuration. The ideas of MFA are refined for other applications in [64–67], and often referred to as dynamic phasors.

In order to use the MFA method to study the power electronic systems, it is necessary to explore the properties of partial-Fourier-series approximations. These properties are discussed in the subsections below.

2.2.1 MFA Representation

According to the averaging method presented in [20,30], a quasiperiodic signal $x(t)$ can be approximated by a partial Fourier series. This series can be expressed as either

a trigonometric Fourier series (TFS) or an exponential Fourier series (EFS):

$$x(t) \approx x_0(t) + \sum_{k=1}^{K} (x_{kc}(t)\cos(k\omega t) + x_{ks}(t)\sin(k\omega t)) \tag{2.21}$$

$$= \sum_{k=-K}^{K} \langle x \rangle_k(t) e^{jk\omega t} \tag{2.22}$$

where $x_0(t)$, $x_{kc}(t)$, and $x_{ks}(t)$ are real-valued TFS coefficients referred to as the index-0, index-kc, and index-ks averages, respectively, $\langle x \rangle_k(t)$ is a complex-valued EFS coefficient referred to as the index-k average, and ω is the switching angular frequency. This series is a Kth-order approximation of $x(t)$. While the approximation improves as K increases, it is shown in [24] that values of one or two are sufficient with very modest improvement for larger K. An average vector of length $(2K+1)$ can be constructed from the TFS coefficients in (2.21):

$$\mathbf{x} = [x_0 \; x_{1c} \; x_{1s} \; \ldots \; x_{Kc} \; x_{Ks}]^{\mathrm{T}}. \tag{2.23}$$

With this vector, (2.21) can be reconstructed as $x(t) \approx \boldsymbol{\theta}^{\mathrm{T}}(t)\mathbf{x}$, where $\boldsymbol{\theta}(t)$ is defined as

$$\boldsymbol{\theta}(t) = [1 \; \cos(\omega t) \; \sin(\omega t) \; \ldots \; \cos(K\omega t) \; \sin(K\omega t)]^{\mathrm{T}}. \tag{2.24}$$

2.2.2 Relationship Between Fourier Series Representations

Suppose a signal $x(t)$ is approximated by the Kth-order series in (2.21) and (2.22). By Euler's formula, the relationship between the TFS and EFS coefficients can be

expressed as

$$\langle x_0 \rangle = x_0 \tag{2.25}$$

$$\langle x \rangle_k = \frac{1}{2} x_{kc} - \frac{j}{2} x_{ks} \tag{2.26}$$

$$\langle x \rangle_{-k} = \frac{1}{2} x_{kc} + \frac{j}{2} x_{ks}. \tag{2.27}$$

2.2.3 Average of Product and Quotient

Often, the mathematical model of a converter involves the product of two signals (e.g., a switching function and a voltage or a current [68]). Suppose two signals $x(t)$ and $y(t)$ are approximated by Kth-order series and the corresponding average vectors are denoted $\mathbf{x}$ and $\mathbf{y}$, respectively. A Kth-order approximation of the product of these signals can be constructed by computing the product of the approximations of the multiplicand and multiplier and neglecting higher order terms:

$$z(t) = x(t)y(t) \approx \sum_{k=-K}^{K} \langle x \rangle_k e^{jk\omega t} \sum_{k=-K}^{K} \langle y \rangle_k e^{jk\omega t} \approx \sum_{k=-K}^{K} \langle z \rangle_k e^{jk\omega t}. \tag{2.28}$$

A discrete convolution relationship can be used to calculate the index-k average of the product [30]:

$$\langle z \rangle_k = \sum_l \langle x \rangle_l \langle y \rangle_{k-l} \tag{2.29}$$

where the sum is taken over all integers l that lie on the interval for which the indices $\langle x \rangle_l$ and $\langle y \rangle_{k-l}$ are defined. Using the relationships between the TFS and

EFS coefficients in (2.25)–(2.27), it can be shown that

$$z_0 = x_0 y_0 + \sum_{l=1}^{K} \left(\frac{1}{2} x_{lc} y_{lc} + \frac{1}{2} x_{ls} y_{ls} \right) \tag{2.30}$$

$$\begin{aligned} z_{kc} = {} & x_0 y_{kc} + x_{kc} y_0 + \sum_{l=-K+k}^{-1} \left(\frac{1}{2} x_{-lc} y_{(k-l)c} + \frac{1}{2} x_{-ls} y_{(k-l)s} \right) \\ & + \sum_{l=1}^{k-1} \left(\frac{1}{2} x_{lc} y_{(k-l)c} - \frac{1}{2} x_{ls} y_{(k-l)s} \right) + \sum_{l=k+1}^{K} \left(\frac{1}{2} x_{lc} y_{(-k+l)c} + \frac{1}{2} x_{ls} y_{(-k+l)s} \right) \end{aligned} \tag{2.31}$$

$$\begin{aligned} z_{ks} = {} & x_0 y_{ks} + x_{ks} y_0 + \sum_{l=-K+k}^{-1} \left(\frac{1}{2} x_{-lc} y_{(k-l)s} - \frac{1}{2} x_{-ls} y_{(k-l)c} \right) \\ & + \sum_{l=1}^{k-1} \left(\frac{1}{2} x_{lc} y_{(k-l)s} + \frac{1}{2} x_{ls} y_{(k-l)c} \right) + \sum_{l=k+1}^{K} \left(-\frac{1}{2} x_{lc} y_{(-k+l)s} + \frac{1}{2} x_{ls} y_{(-k+l)c} \right). \end{aligned} \tag{2.32}$$

For notational simplicity, a $(2K+1) \times (2K+1)$ matrix $\mathbf{\Phi}$ associated with $\mathbf{x}$ is defined such that the average vector $\mathbf{z}$ can be represented as

$$\mathbf{z} = \mathbf{\Phi}(\mathbf{x})\mathbf{y}. \tag{2.33}$$

In a special case where $x(t)$, $y(t)$ and the product $z(t)$ are approximated by a first-order series, the matrix $\mathbf{\Phi}(\mathbf{x})$ can be expressed as

$$\mathbf{\Phi}(\mathbf{x}) = \begin{bmatrix} x_0 & \frac{1}{2} x_{1c} & \frac{1}{2} x_{1s} \\ x_{1c} & x_0 & 0 \\ x_{1s} & 0 & x_0 \end{bmatrix}. \tag{2.34}$$

Quotients can be represented similarly. Given Kth-order approximated signals $z(t)$, $x(t)$, and the quotient $y(t) = z(t)/x(t)$, utilizing the relationship for the average of a product results in the following expression for the average of a quotient:

$$\mathbf{y} = \mathbf{\Phi}(\mathbf{x})^{-1}\mathbf{z}. \tag{2.35}$$

It is noted that $y(t)$ may not be approximated by a Kth-order Fourier series in the case that $\mathbf{\Phi}(\mathbf{x})$ is not invertible.

2.2.4 Average of Time Derivative

Suppose a signal $x(t)$ is approximated with a Kth-order series. Differentiating with respect to time yields

$$\begin{aligned}\frac{dx}{dt} \approx \frac{dx_0}{dt} &+ \sum_{k=1}^{K}(k\omega x_{ks}\cos(k\omega t) - k\omega x_{kc}\sin(k\omega t)) \\ &+ \sum_{k=1}^{K}\left(\frac{dx_{kc}}{dt}\cos(k\omega t) + \frac{dx_{ks}}{dt}\sin(k\omega t)\right). \end{aligned} \tag{2.36}$$

If $\frac{dx}{dt}$ is approximated with a Kth-order series represented by average vector $\mathbf{\frac{dx}{dt}}$, then

$$\mathbf{\frac{dx}{dt}} = \frac{d\mathbf{x}}{dt} + \mathbf{Tx} \tag{2.37}$$

where $\frac{d\mathbf{x}}{dt}$ is the time derivative of the average vector $\mathbf{x}$ and $\mathbf{T}$ is a $(2K+1)\times(2K+1)$ matrix that is zero everywhere except for $\mathbf{T}_{2k,2k+1} = k\omega$ and $\mathbf{T}_{2k+1,2k} = -k\omega$ for $k \in \{1, 2, \ldots, K\}$.

2.2.5 Average of Switching Function

A switching function q which controls the switching of power electronic systems takes values of zero and one corresponding to the switch being open or closed, respectively. For a switching function that becomes one at the beginning of the switching period and has a constant duty cycle D, the index-0, index-kc and index-ks averages are

given by

$$q_0 = D \tag{2.38}$$

$$q_{kc} = \frac{1}{k\pi}\sin(2\pi kD) \tag{2.39}$$

$$q_{ks} = \frac{1}{k\pi}(1 - \cos(2\pi kD)). \tag{2.40}$$

These averages are constants for open-loop operation at constant duty cycle. It has been shown in [20] that for slowly varying duty cycle (whether varied in open-loop or closed-loop), the same expressions can be used with D replaced by the time-varying duty cycle.

2.3 Discrete-Time Models

Discrete-time models have been studied for modeling power electronic systems [45, 46, 48, 69–71]. In [69], discrete-time models are derived to account for the effects of sampling due to the pulse-width modulators and standard analog controllers. Extensions of this approach to study various analog control techniques are described in [46, 48]. In [70, 71], the discrete-time models have been successfully used to study the nonlinear dynamics of switching power electronic converters, such as bifurcations, strange attractors, and routes to chaos. These models are typical sampled-data models that naturally represent the periodic behavior of the systems and have been shown to be more accurate than the averaged models. The widespread application of these approaches has been limited because of the involvement of matrix exponentials. Bilinear discrete-time models are utilized in [49] to retain necessary accuracy of these sampled-data models with less complexity by applying first-order approximations to the matrix exponentials. However, these models are not able to describe the behavior of the systems when the switching instants are not positioned at the beginning of the switching cycle. To address this problem, an exact small-signal z-domain model

is proposed in [32] that correctly takes into account sampling, modulator effects and delays in the discrete-time controller loop. This approach has been shown to be directly applicable to digitally controlled converters where the analog-digital sampling instants can occur at any time during a switching period. In [50], this small-signal z-domain model is extended to modeling any constant-frequency PWM converter. Recently, the applications of these approaches have extended to discrete-time analysis and modeling of digitally controlled power electronic systems [72–76]. However, these discrete-time models require relatively long simulation run times (compared to averaged models) because the simulation time step is limited by the sampling rate.

2.4 Feedback Control

Feedback control has been used for output regulations of power electronic systems. With feedback control, the operation of the switching would adjust automatically to ensure that the system would return to the operating point after disturbances (e.g., a fast disturbance such as noise pulses, a large disturbance such as loss of load or variations in the components, or a continuous small disturbance such as ripple) [77].

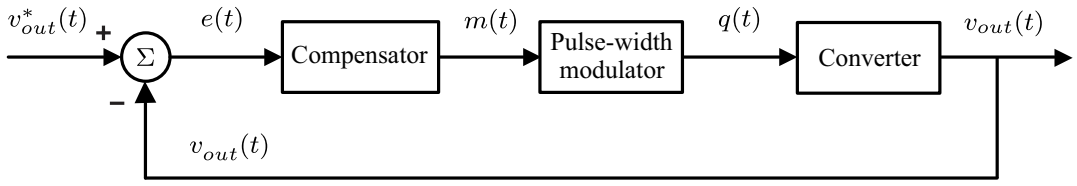

Figure 2.2: The diagram of a closed-loop PWM converter.

For a voltage-mode closed-loop PWM converter shown in Figure 2.2, the feedback controller is often developed based on the architecture where the converter output voltage $v_{out}(t)$ is compared with the reference voltage $v^*_{out}(t)$ and fed into the compensator for computing the modulation signal $m(t)$. The modulation signal gener-

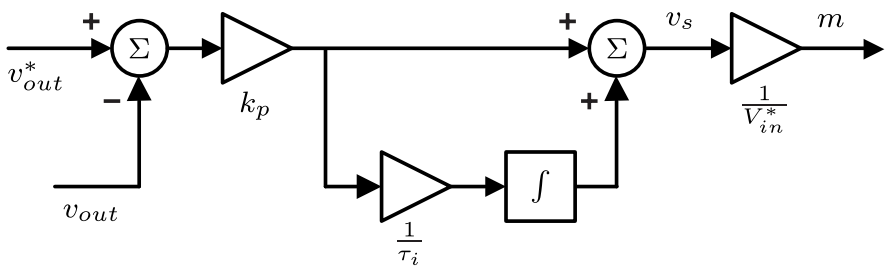

Figure 2.3: A simple PI compensator.

ates the switching signal $q(t)$ via the pulse-width modulator, which in turn controls the switching of the converter. Most of the controllers so far reported in literature employ such a voltage-mode control principle [78–81]. In [78], a versatile power converter controller is designed to provide dual outputs using voltage-mode regulation. The key features of this design are its low-power dissipation, reconfigurability, use of either delay or voltage feedback, and multiple outputs. In [79], the architecture of a digital PWM controller for application in multiphase voltage regulation modules is presented. Therein, passive current sharing and transient response of the voltage regulation module are analyzed. A scheme for sensing a combination of the output voltage and output current with a single low-resolution window analog-to-digital converter is proposed. An improved topology named the multiphase coupled-buck converter is proposed in [80]. This approach uses the existing coupled inductor windings to form an active clamping circuit between interleaved channels to solve the voltage spike problem in voltage regulation modules. In [81], a novel switching-capacitor PWM converter is proposed. The converter is a combination of a switching-capacitor converter and a PWM converter and is suitable for both voltage regulator module and voltage regulator down application.

2.4.1 Compensator

Conventional PID compensators are commonly used to regulate the output voltage of converters due to their simplicity and flexibility of design (e.g., [82–84]). A simple

PI compensator, such as that depicted in Figure 2.3, is often sufficient to meet performance requirements. This compensator calculates the modulation signal $m(t)$ in order to regulate the output voltage using the output voltage error as the input to the compensator. The PI compensator is described as

$$v_s = k_p(v^*_{out} - v_{out}) + e \tag{2.41}$$

$$\frac{de}{dt} = \frac{k_p(v^*_{out} - v_{out})}{\tau_i} \tag{2.42}$$

$$m = \frac{v_s}{V^*_{in}} \tag{2.43}$$

where k_p and τ_i are control parameters and V^*_{in} is the nominal value of the input voltage V_{in}.

2.4.2 Pulse-Width Modulator

In feedback control of power electronic systems, it is necessary to represent the relationship between the modulation signal $m(t)$ and the switching function $q(t)$.

Naturally sampled PWM is traditionally an analog technique where the modulation signal is compared with a carrier signal (e.g., a sawtooth function) as shown in Figure 2.4. The switching function is the result of this comparison. MFA modeling has been studied for such implementation. In [20], the switching function produced by this modulation scheme is approximated by a partial Fourier series. The switching time at which the modulation signal crosses the sawtooth carrier in each switching cycle is solved indirectly within the simulation by introducing an additional state variable and driving an error function to zero. In [24], it is argued that this approach does not account for a potential phase shift in the carrier signal. Therein, a similar set of nonlinear equations is derived for determining the MFA representation of the switching signal, and it is suggested that one iteration of Newton's method with an initial guess corresponding to zero command ripple is sufficient to solve the nonlinear

equation. However, the switching times in [20] and [24] remain implicit and cannot be solved directly.

Uniformly sampled PWM has attracted increasing interest because of the ease of digital implementation (e.g., [31–33]). In this setting as depicted in Figure 2.4, the modulation signal is regularly sampled at the beginning of the switching period before being compared with the carrier and stored in a shadow register for use during that period (e.g, [85]). For trailing edge modulation, the switching functions produced by these two PWM sampling techniques are shown in Figure 2.5. In naturally sampled PWM, the edges of switching function $q_n(t)$ are determined by crossings of the instantaneous modulation signal $m(t)$ and the carrier signal $c(t)$. In uniformly sampled PWM, the switching instant does not depend on the ripple of modulation signal explicitly; rather, it depends on the value of modulation signal at the beginning of the switching cycle. However, this PWM sampling technique produces a delay in switching function $q_u(t)$. It has been shown in [86] that the delay can be significant when the modulation depth or the ratio of modulation signal frequency to carrier signal frequency increases. Typically, $m(t)$ would change relatively slowly with respect to the switching frequency and have a small switching frequency ripple component, in which case uniformly sampled PWM is very similar in performance to naturally sampled PWM.

2.4.3 Digital Feedback Controller

Traditionally, feedback controllers have been implemented with analog circuits (e.g., [68, 87, 88]) . Recently, digital controllers have attracted increasing interest due to the rapid evolution of digital integrated circuit technologies applied to signal processors, analog to digital converters and digital to analog converters [89–91]. Compared with analog controllers, digital controllers have higher robustness, reliability and flexibility, lower power consumption, and better ability to employ sophisticated control

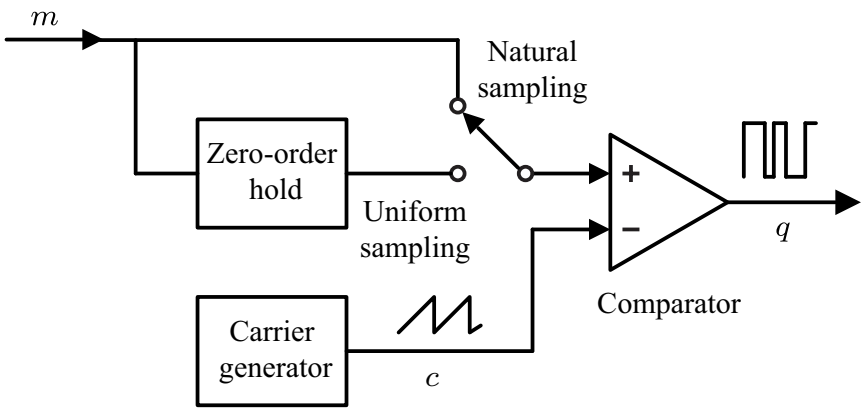

Figure 2.4: Two PWM sampling techniques.

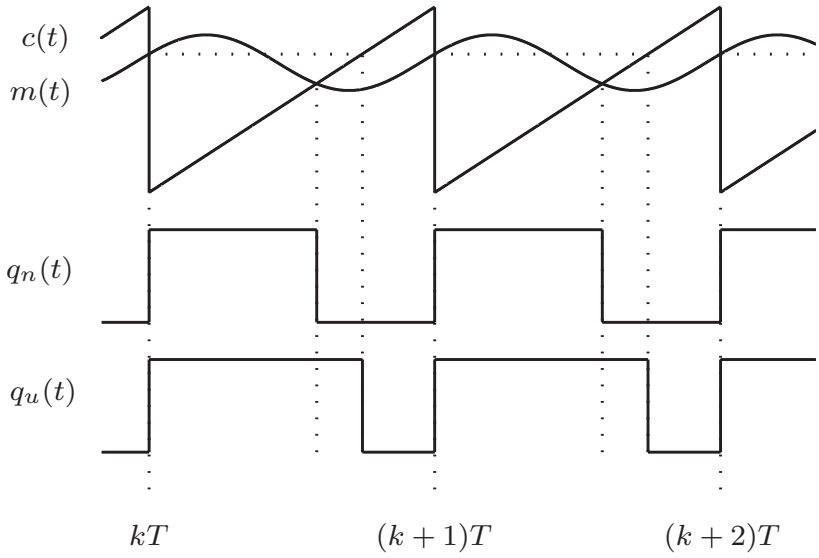

Figure 2.5: Natural sampling versus uniform sampling.

schemes [34–39]. In [34], a complete digital PWM controller IC with feedforward compensation of the input voltage is described. Therein, the feedforward compensation is accomplished through a delay-line digital PWM where the cell delay is made inversely proportional to the input voltage. A voltage mode digital controller for low-power high-frequency dc-dc switch-mode power supplies is proposed in [35]. Such a controller has fast transient response, approaching the physical limitations of a given power stage. A digital current-model control technique is studies in [36]. Therein, a

digital current-mode control technique for dc-dc converters is proposed and its digital implementation is described. The computational burden on the DSP is less compared to other methods of digital current-mode control because a simpler duty ratio control law is implemented here. More sophisticated control schemes are explored in [37–39]. In [37], a digital pulse-width modulation/pulse-frequency modulation (PWM/PFM) controller with input voltage feedforward for synchronous dc-dc buck converters is described. The controller includes automatic PWM/PFM mode switching and effective synchronous operation with a minimum number of active components and without the need for current sensing in PFM mode of operation. A high-frequency digital controller that includes an optimized analog-digital converter with a novel formulation of digital error value based on target clock frequency and converter output voltage is presented in [38]. An online closed-loop compensator autotuning digital power controller is proposed in [39]. This approach is relatively simple, does not require the knowledge and/or measurement of the power stage or closed-loop frequency response, and does not depend on conventional deign methods and the associated rule-of-thumb design criteria.

2.5 Stability in Power Electronic Systems

In many power electronic systems, power electronic converters are used for many functions such as to supply power to buses or as point-of-load converters. As control technology has improved, these converters have become more tightly regulated with high bandwidth and good robustness properties to mitigate the possible propagation of disturbances from the power supply to the load. A consequence of this improvement in control is that these converters are likely to behave as constant power loads and exhibit negative small signal impedance at their input terminals, which can cause instability problems for such systems [92, 93].

2.5.1 Local Stability

To study the instability phenomenon in nonlinear power electronic systems, linearized (small-signal) average models can be developed around the equilibrium points, and the local stability can be investigated considering the small-signal information [94–98]. These approaches are capable of predicting the existence of stable steady-state equilibrium points. Nevertheless, the small-signal nature precludes the use of these approaches for large-signal stability analysis of power electronic systems.

2.5.2 Large-Signal Stability

To study the large-signal stability of nonlinear power electronic systems, it is necessary to set forth an effective method to estimate the region of attraction. The region of attraction is defined as a region for which all system trajectories starting within the region asymptotically approach the equilibrium point. A traditional approach to deal with transient stability analysis and ROA estimation of power electronics systems is with gridding-based methods in which numerical integration of the nonlinear differential equations describing the system is performed. This method provides an accurate description of transient phenomena, but its computational cost can limit application (e.g., excluding real-time transient stability assessment) and significantly constrain the number of cases which can be analyzed.

The closest equilibrium point (UEP) method, the controlling UEP method and the boundary of stability region based controlling UEP method are alternative direct approaches to large signal stability analysis. These approaches provide conservative ROA estimates of power systems without numerical integrating the system trajectories [99–101]. However, the computation burden for these methods remains large. Bifurcation analysis is used in [102] to analyze the dynamics of the input voltage on the stability of a dc/dc converter. In particular, the range of input voltage is found

where the dc/dc converter remains stable. However, this method does not yield an ROA estimate.

Lyapunov techniques have been used to search for ROA estimates of power electronic systems [40–44]. These approaches rely on evaluating the values of carefully chosen scalar functions (Lyapunov functions) on SSA models without numerically integrating the system trajectories. The SSA models are capable of portraying the average behavior of power electronic systems. However, the small ripple assumption inherent to SSA models can limit the applicability of these models [19].

CHAPTER 3

MULTIFREQUENCY AVERAGING IN UNIFORMLY SAMPLED PWM CONVERTERS

It has been shown in Section 2.4.2 that the MFA models have been studied for naturally sampled PWM in power electronic systems. In this chapter, the MFA method is extended by making the following contributions: 1) A method of representing uniformly sampled PWM converters using MFA is proposed. 2) A model stability problem associated with traditional MFA models is observed and described. 3) A solution to the observed stability problem is proposed. The remainder of this chapter is organized as follows. The MFA model of a buck converter and a PI compensator for the converter are described in Sections 3.1 and 3.2, respectively. Also, the MFA representation of the switching function in a uniformly sampled PWM converter is provided in Section 3.2. In Section 3.3, a stability issue associated with integrators in MFA models is explored, and a solution is proposed. Simulation studies demonstrating the proposed model during transient and steady-state intervals and frequency-domain analysis are presented in Section 3.4. Experimental validation is described in Section 3.5. A concluding summary and remarks are provided in Section 3.6.

3.1 MFA Model of Buck Converter

Unlike the simple buck converter shown in Figure 2.1, a practical buck converter involves the equivalent series resistances for the inductor and the capacitor. In this section, the MFA model of a practical buck converter shown in Figure 3.1 is set forth. It is assumed that the buck converter is operating in continuous conduction mode.

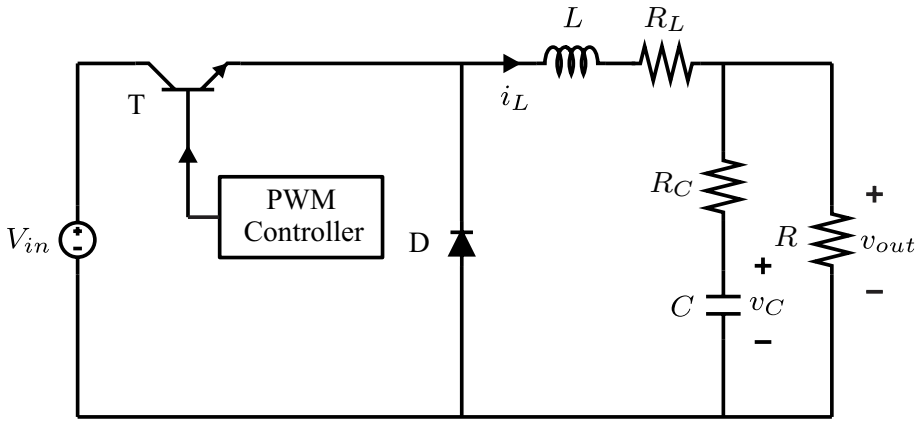

Figure 3.1: A practical buck converter.

The detailed model of the converter is given as

$$L\frac{di_L}{dt} = qV_{in} - R_L i_L - v_{out} \tag{3.1}$$

$$C\frac{dv_C}{dt} = i_L - \frac{v_{out}}{R} \tag{3.2}$$

$$v_{out} = \frac{R}{R + R_C}(v_C + R_C i_L) \tag{3.3}$$

where q is the switching function that represents the transistor state. If each signal is approximated by a Kth-order series, then applying the properties in Sections 2.2.1–2.2.4 yields the following MFA model:

$$L(\frac{d\mathbf{i}_L}{dt} + \mathbf{T}\mathbf{i}_L) = \mathbf{q}V_{in} - R_L\mathbf{i}_L - \mathbf{v}_{out} \tag{3.4}$$

$$C(\frac{d\mathbf{v}_C}{dt} + \mathbf{T}\mathbf{v}_C) = \mathbf{i}_L - \frac{\mathbf{v}_{out}}{R} \tag{3.5}$$

$$\mathbf{v}_{out} = \frac{R}{R + R_C}(\mathbf{v}_C + R_C\mathbf{i}_L). \tag{3.6}$$

It is noted that, unlike the boost converter [20], this model does not involve the product of two time-varying signals. There are circumstances in which the buck converter model may include such products. Examples include the case when the

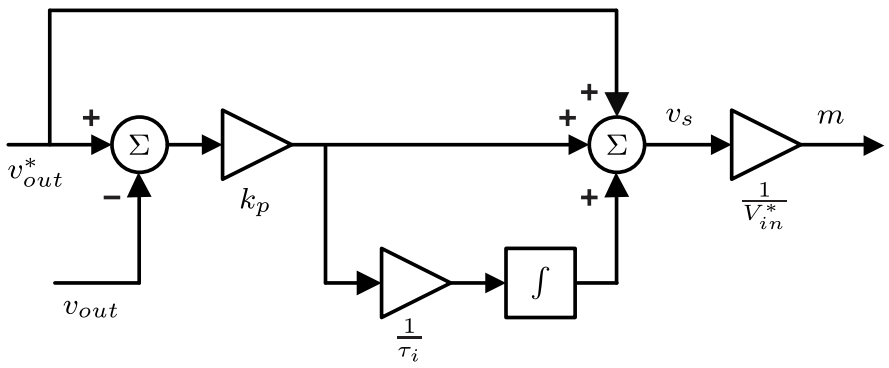

Figure 3.2: PI compensator with feedforward voltage command v^*_{out}.

input voltage source has series resistance and the case when parasitic voltage drops in the semiconductor elements are represented (e.g., [29]).

3.2 MFA Model of Feedback Controller

It has been shown in Section 2.4.1 that the conventional PID compensator is commonly used to regulate the output voltage of a converter due to its simplicity and flexibility of design. A simple PI compensator, such as that depicted in Figure 2.3, is often sufficient to meet performance requirements. Herein, a feedforward voltage command v^*_{out} is used as the input to this simple PI compensator to provide faster dynamic response during start-up transient. Such compensator is depicted in Figure 3.2 and the detailed model can be described as

$$v_s = v^*_{out} + k_p(v^*_{out} - v_{out}) + e \tag{3.7}$$

$$\frac{de}{dt} = \frac{k_p(v^*_{out} - v_{out})}{\tau_i} \tag{3.8}$$

$$m = \frac{v_s}{V^*_{in}} \tag{3.9}$$

where k_p and τ_i are control parameters and V^*_{in} is the nominal value of the input voltage V_{in}.

If each signal is approximated by a Kth-order series, then applying the properties in Sections 2.2.1–2.2.4 yields the following MFA model of this compensator:

$$\mathbf{v}_s = \mathbf{v}^*_{out} + k_p(\mathbf{v}^*_{out} - \mathbf{v}_{out}) + \mathbf{e} \tag{3.10}$$

$$\frac{d\mathbf{e}}{dt} + \mathbf{T}\mathbf{e} = \frac{k_p(\mathbf{v}^*_{out} - \mathbf{v}_{out})}{\tau_i} \tag{3.11}$$

$$\mathbf{m} = \frac{\mathbf{v}_s}{V^*_{in}}. \tag{3.12}$$

In order to complete the model of the closed-loop buck converter, it is necessary to represent the relationship between the modulation signal $m(t)$ and the switching function $q(t)$. Herein, uniformly sampled PWM described in Section 2.4.2 is considered. With uniformly sampled PWM, the modulation signal is regularly sampled at the beginning of the switching period before being compared with the carrier and stored in a shadow register for use during that period (e.g, [85]). It has been shown in Figure 2.4 that the switching instant in uniformly sampled PWM does not depend on the ripple of modulation signal explicitly; rather, it depends on the value of modulation signal at the beginning of the switching cycle.

MFA representation of the relationship between the modulation signal and the switching function in naturally sampled PWM has been studied in [20, 24]. In [20], an algebraic equation describing the duty cycle D of the switching function $q_n(t)$ in terms of m_0, m_{1c} and m_{1s} is proposed. An integral controller is used to solve for D dynamically. This approach introduces an extraneous state variable and is only valid for first-order approximations. In [24], the relationships between the modulation signal and the switching function are explored from a different perspective. Therein, higher order approximations are treated as well as alternative carrier functions. It is also suggested that the solution to the algebraic equation describing the intersection of the modulation signal and the carrier function can be approximated satisfactorily with a single Newton step with an initial guess corresponding to zero ripple. It can be

shown that the relationships that are described therein are equivalent to (2.38)–(2.40) when the instantaneous value of $\mathbf{m}$ is used to calculate D.

Multifrequency averaging does not involve the algebraic complexity associated with uniformly sampled PWM. If the modulation signal is represented as

$$m(t) \approx m_0 + \sum_{k=1}^{K} (m_{kc} \cos(k\omega t) + m_{ks} \sin(k\omega t)) \tag{3.13}$$

then the value of $m(t)$ at the beginning of the switching period (the value that is used by the PWM implementation) is

$$D \approx m_0 + \sum_{k=1}^{K} m_{kc}. \tag{3.14}$$

Application of (2.38)–(2.40) yields the average vector $\mathbf{q}$. While each of the means of averaging the switching function essentially depends on the components of the average vector changing relatively slowly with respect to the switching frequency, this can be particularly noticeable when comparing detailed and averaged models of the uniformly sampled implementation. This is due to the effects of the sampling shown in Figure 2.4.

3.3 Integrator Stabilization

In this section, a numerical issue associated with the MFA approach to modeling integrators is investigated, and an alternative method of modeling integrators is proposed. Consider the integrator described by

$$\frac{dx}{dt} = u(t). \tag{3.15}$$

Table 3.1: Integrator Parameters

ω	1000π rad/s	x_0	0
$u_{1c}^{(i)}$	0.2	$u_{1c}^{(f)}$	0.2
$u_{1s}^{(i)}$	0.2	$u_{1s}^{(f)}$	0.3

If both $x(t)$ and $u(t)$ are approximated by first-order series, then the relationship between the average vectors is

$$\frac{d\mathbf{x}}{dt} = \mathbf{A}\mathbf{x} + \mathbf{u} \tag{3.16}$$

where $\mathbf{A} = -\mathbf{T}$ (from (2.37)) is given by

$$\mathbf{A} = \begin{bmatrix} 0 & 0 & 0 \\ 0 & 0 & -\omega \\ 0 & \omega & 0 \end{bmatrix}. \tag{3.17}$$

The eigenvalues of $\mathbf{A}$ are 0, $j\omega$, and $-j\omega$. Consider such an MFA integrator implementation that is initially operating in steady state while excited by a signal with no dc component represented by $\mathbf{u}^{(i)} = [0\ u_{1c}^{(i)}\ u_{1s}^{(i)}]^{\mathrm{T}}$, where $u_{1c}^{(i)}$ and $u_{1s}^{(i)}$ are constants. The steady-state equilibrium point associated with such an input is $\mathbf{x} = [x_0\ -\frac{u_{1s}^{(i)}}{\omega}\ \frac{u_{1c}^{(i)}}{\omega}]^{\mathrm{T}}$ where x_0 is arbitrary and is related to the initial output of the integrator. At the time $t = 0$ s, the input signal is changed such that $\mathbf{u}^{(f)} = [0\ u_{1c}^{(f)}\ u_{1s}^{(f)}]^{\mathrm{T}}$, where $u_{1c}^{(f)} = u_{1c}^{(i)}$ to ensure that $u(t)$ is continuous. The results of simulating such a situation are shown in Figure 3.3 and Figure 3.4 for the parameters given in Table 3.1. In Figure 3.3, it can be seen that the reconstructed series $x(t)$ corresponding to the average vector $\mathbf{x}$ is identical to the results of a detailed (DET) model of the integrator (i.e., the direct integration of $u(t)$). In Figure 3.4, it can be seen that the elements of $\mathbf{x}$ are initially constant. However, when the input average vector $\mathbf{u}$ is changed, the elements of $\mathbf{x}$ begin to oscillate. Furthermore, the steady-state result $x(t)$ has a dc offset, while the x_0 average in Figure 3.4 does not exhibit this offset. This oscillation is unexpected

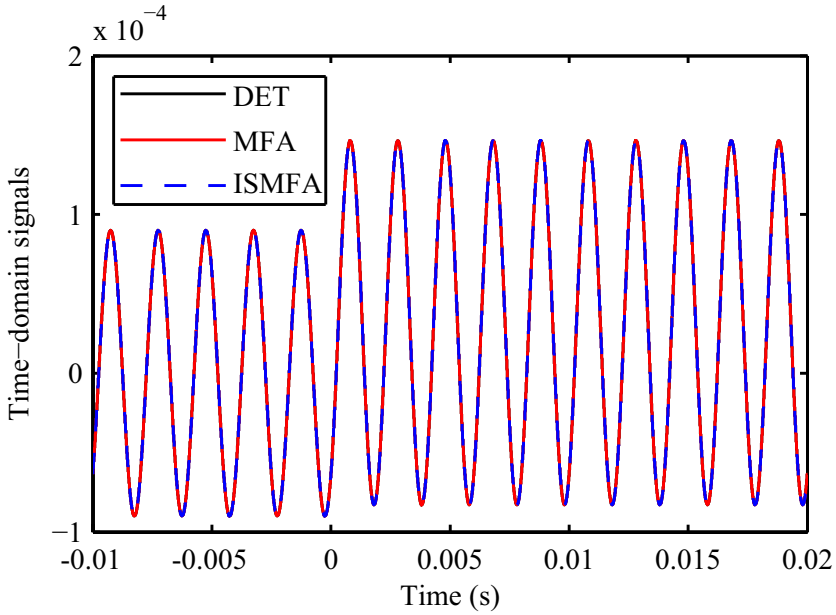

Figure 3.3: Time-domain signals of DET, MFA, and ISMFA models of integrator where $x(t) \approx \boldsymbol{\theta}^{\mathrm{T}}(t)\mathbf{x}$ and $\hat{x}(t) \approx \boldsymbol{\theta}^{\mathrm{T}}(t)\hat{\mathbf{x}}$.

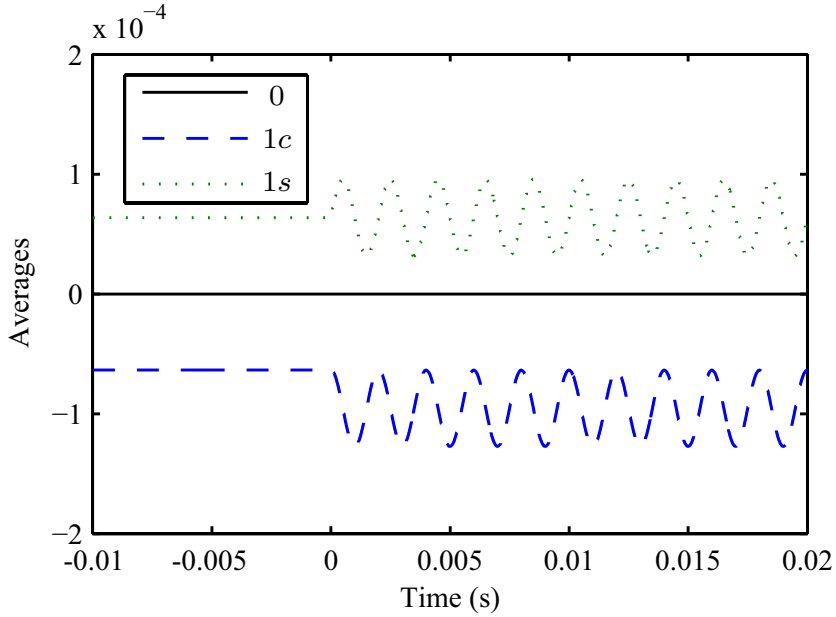

Figure 3.4: Elements of $\mathbf{x}$ for MFA model of integrator.

in an average-value model in which the state variables are expected to take constant values in steady state. This property of average-value models is useful from both a simulation [103] and a control design perspective [104].

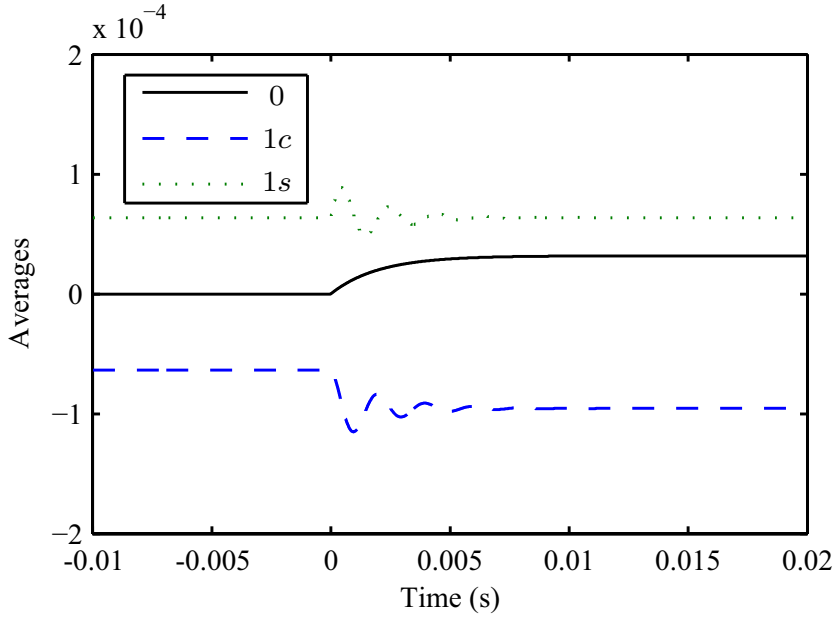

Figure 3.5: Elements of $\hat{\mathbf{x}}$ for ISMFA model of integrator.

An approach to stabilizing this behavior in MFA models resulting in integrator-stabilized MFA (ISMFA) models is described below. Instead of using (3.16) to represent the integrator, the integrator is represented as

$$\frac{d\hat{\mathbf{x}}}{dt} = (\mathbf{A} + \mathbf{K}(t))\hat{\mathbf{x}} + \mathbf{u} \tag{3.18}$$

where $\mathbf{K}(t)$ is a time-varying feedback matrix, which is defined as

$$\mathbf{K}(t) = \begin{bmatrix} 0 & K_{1c}\cos(\omega t) & K_{1s}\sin(\omega t) \\ 0 & -K_{1c} & 0 \\ 0 & 0 & -K_{1s} \end{bmatrix} \tag{3.19}$$

and K_{1c} and K_{1s} are time-varying parameters used to dampen the system. Suppose an error variable $e(t)$ is used to represent the difference between the output values of the MFA integrator and the ISMFA integrator, i.e., $e(t) = x - \hat{x}$. Further, suppose that the two integrator models have the same initial state such that $e(t_0) = x(t_0) - \hat{x}(t_0) = 0$.

Differentiating $e(t)$ with respect to time yields

$$\frac{de}{dt} = \frac{d}{dt}(x - \hat{x}) = \frac{d\boldsymbol{\theta}^{\mathrm{T}}}{dt}(\mathbf{x} - \hat{\mathbf{x}}) + \boldsymbol{\theta}^{\mathrm{T}}(t)\frac{d}{dt}(\mathbf{x} - \hat{\mathbf{x}}). \tag{3.20}$$

It can be shown that for arbitrary input vector, the time derivative of $e(t)$ is zero at all times. Therefore, the ISMFA model of the integrator will result in time-domain predictions for the output of the integrator that are identical to the predictions of the MFA model. The notation $\hat{\mathbf{x}}$ is used here to differentiate the state variables of the MFA and ISMFA models, but this notation is not used below. The following text discusses the ISMFA model, and the state variable vector for the ISMFA model is referred to as $\mathbf{x}$.

Given the possibility of introducing the state feedback shown in (3.18) without affecting the time-domain predictions of the model, it is possible to select K_{1c} and K_{1s} to stabilize the integrator behavior. If the input average vector has constant values for u_{1c} and u_{1s}, the steady-state values of the state average vector are

$$x_{1c} = -\frac{u_{1s}}{\omega} \tag{3.21}$$

$$x_{1s} = \frac{u_{1c}}{\omega}. \tag{3.22}$$

A measure of distance to these steady-state values can be defined as

$$V = \Delta_1^2 + \Delta_2^2 \tag{3.23}$$

where

$$\Delta_1 = u_{1c} - \omega x_{1s} \tag{3.24}$$

$$\Delta_2 = u_{1s} + \omega x_{1c}. \tag{3.25}$$

Differentiation of these measures with respect to time (and assuming the input vector is constant) yields the following state equations:

$$\frac{d}{dt}\begin{bmatrix}\Delta_1\\ \Delta_2\end{bmatrix} = \begin{bmatrix}-K_{1s} & -\omega\\ \omega & -K_{1c}\end{bmatrix}\begin{bmatrix}\Delta_1\\ \Delta_2\end{bmatrix} + \begin{bmatrix}K_{1s} & 0\\ 0 & K_{1c}\end{bmatrix}\begin{bmatrix}u_{1c}\\ u_{1s}\end{bmatrix}. \tag{3.26}$$

Using these state equations, the time derivative of the function V can be calculated as

$$\dot{V} = 2\Delta_1\omega x_{1s}K_{1s} - 2\Delta_2\omega x_{1c}K_{1c}. \tag{3.27}$$

If K_{1c} and K_{1s} are chosen such that

$$2\omega x_{1s}K_{1s} = -\alpha\Delta_1 \tag{3.28}$$

$$2\omega x_{1c}K_{1c} = \alpha\Delta_2 \tag{3.29}$$

where α is a positive constant, then

$$\dot{V} = -\alpha(\Delta_1^2 + \Delta_2^2) = -\alpha V \tag{3.30}$$

and the distance measure would decay exponentially.

Practical constaints prevent the satisfaction of (3.28) and (3.29) in every case (e.g., small values of x_{1c} and x_{1s}). In this case, the magnitudes of K_{1s} and K_{1c} can be bounded by a large positive constant M. This can be accomplished by defining a threshold parameter as

$$\epsilon = \frac{\alpha}{2M}. \tag{3.31}$$

Then, practical solutions for K_{1c} and K_{1s} can be expressed as

$$K_{1c} = \frac{\alpha}{2} \begin{cases} \frac{\Delta_2}{\omega x_{1c}}, & |\omega x_{1c}| > \epsilon |\Delta_2| \\ \frac{\text{sign}(\Delta_2 x_{1c})}{\epsilon}, & \text{otherwise} \end{cases} \tag{3.32}$$

$$K_{1s} = -\frac{\alpha}{2} \begin{cases} \frac{\Delta_1}{\omega x_{1s}}, & |\omega x_{1s}| > \epsilon |\Delta_1| \\ \frac{\text{sign}(\Delta_1 x_{1s})}{\epsilon}, & \text{otherwise.} \end{cases} \tag{3.33}$$

The ISMFA model of the integrator is simulated using the same input as described above with $\alpha = 10^3$ s^{-1} and $\epsilon = 10^{-2}$. It can be seen in Figure 3.3 that the reconstructed output of the integrator model is identical to that of the detailed model and the MFA model. Figure 3.5 shows the elements of the average vector for the ISMFA model of the integrator. It can be seen that the elements of the average vector are initially in steady state (in the same way as the MFA model). However, when the change in integrator input occurs, the elements associated with the ISMFA model experience a transient change, ultimately settling into steady-state values. The time constant associated with this transient change is controlled by the value of α and can be adjusted accordingly.

3.4 Simulation Studies

A number of simulation studies were conducted to demonstrate the proposed ISMFA method. In particular, the buck converter shown in Figure 3.1 with the feedback controller shown in Figure 3.2 and the parameters given in Table 3.2 is studied. A detailed model, an MFA model, and an ISMFA model of the converter are constructed. For the ISMFA model, the stabilization parameters are given as $\alpha = 10^6$ s^{-1} and $\epsilon = 10^{-2}$.

Table 3.2: Parameters of Dc/Dc Buck Converter

V_{in}	250 V	L	1.52 mH	R	6 Ω
V_{in}^*	250 V	R_L	35 mΩ	k_p	0.0708
v_{out}^*	150 V	C	167 µF	τ_i	0.001
f	10 kHz	R_C	50 mΩ		

3.4.1 Time-Domain Comparison of ISMFA Models with Various Approximation Orders

The accuracy of a partial Fourier series can be increased by increasing the number of terms in the series, i.e., K. It has been found in [24] that values of one or two are generally sufficient to represent the switching harmonics. In Figure 3.6, the inductor current and capacitor voltage for a detailed model and an ISMFA model of orders zero, one, and two are shown. Table 3.3 compares the dc value and peak-peak (p-p) value of inductor current and capacitor voltage and simulation runtimes in each model. The simulation for each model is carried out on a personal computer (Intel(R) Core(TM) i7-3770 CPU @ 3.40 GHz, 8.00 GB RAM, 64-bit Operating System). It can be seen that the zeroth-order ISMFA model correctly predicts the average value of the signals. The second-order model more carefully approximates the detailed model than the first-order model, but both of the higher order models accurately predict the nature of the harmonics in the waveforms. Therefore, the observation in [24] that a first- or second-order model is sufficient is also confirmed here. It can be observed that the detailed model takes 5 times more simulation runtimes than the ISMFA models and the higher order ISMFA model takes longer simulation runtimes than the lower order ISMFA model.

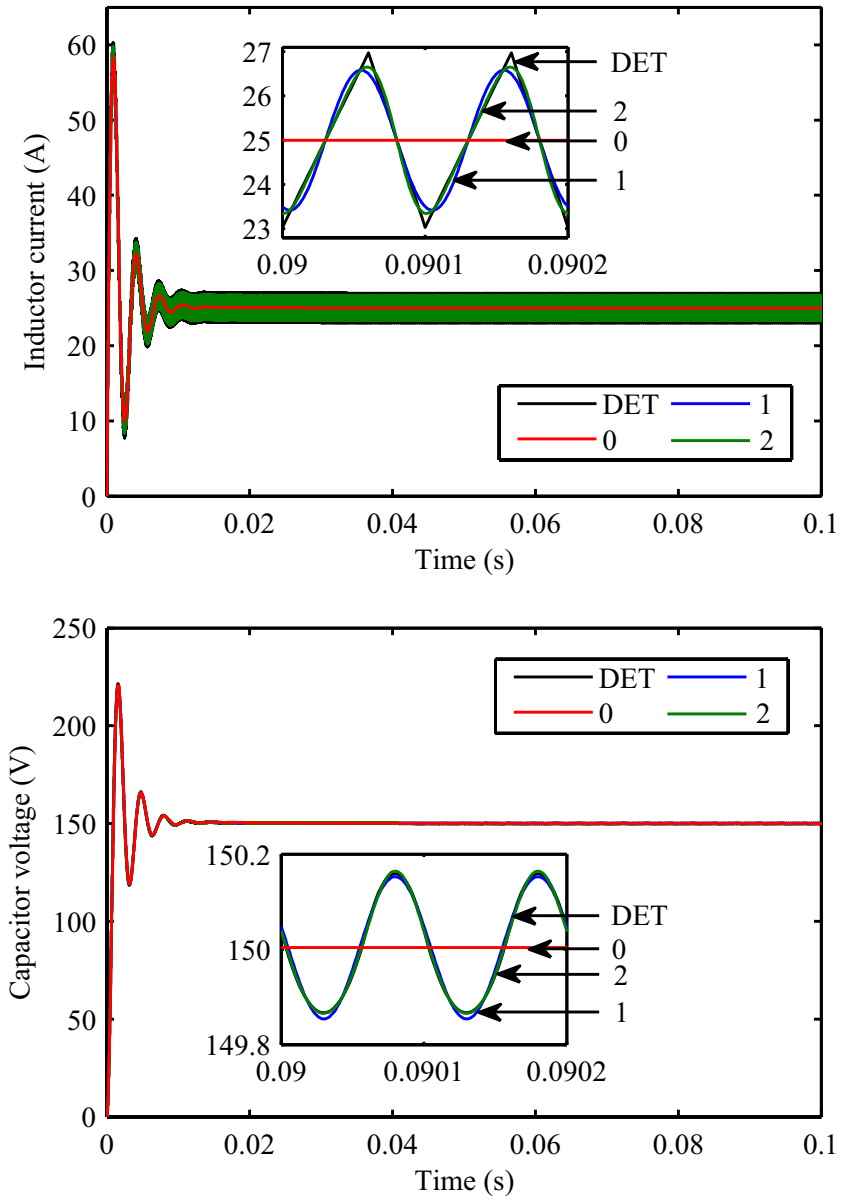

Figure 3.6: Simulation results of inductor current and capacitor voltage for detailed (DET) and ISMFA models of orders 0, 1, and 2.

3.4.2 Time-Domain Comparison of MFA and ISMFA Models

While the justification for introducing the ISMFA model presented in Section 3.3 was demonstrated with a simple integrator, an example in which the MFA model demonstrates unstable behavior is presented below. Simulation results showing the initial startup transient are shown in Figure 3.7–3.9. It can be seen that both the

Table 3.3: Comparison of dc value and peak-peak (P-P) value of inductor current and capacitor voltage and simulation runtimes for detailed (DET) and ISMFA models of orders 0, 1, and 2.

Models	Inductor current (A)		Capacitor voltage (V)		Runtimes (s)
	DC	P-P	DC	P-P	
DET	25.00	3.94	150.00	0.30	1.4490
0	25.00	0	150.00	0	0.0406
1	25.00	3.16	150.00	0.30	0.1778
2	25.00	3.30	150.00	0.30	0.2704

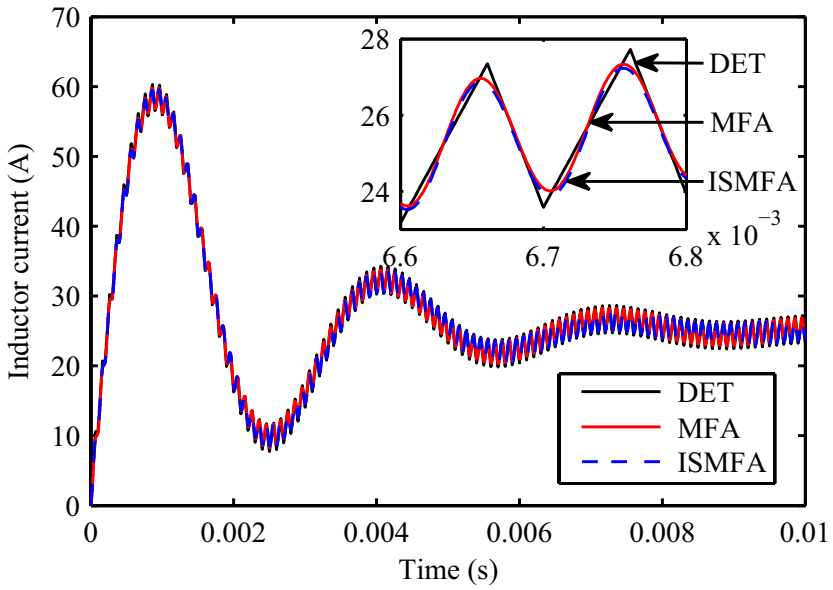

Figure 3.7: Simulation results of startup transient inductor current for detailed (DET), (first-order) MFA, and ISMFA models.

(first-order) MFA and ISMFA models accurately predict the inductor current and capacitor voltage with respect to the detailed model. It can be observed that close agreement exists between the duty cycle as predicted by the ISMFA and detailed models. These waveforms are depicted over a longer period of time in Figure 3.10–3.12. It can be seen that the MFA model begins to oscillate over time and becomes unstable. This instability is not observed in either the detailed model or the ISMFA model. It is attributed to the integrator instability described in Section 3.3.

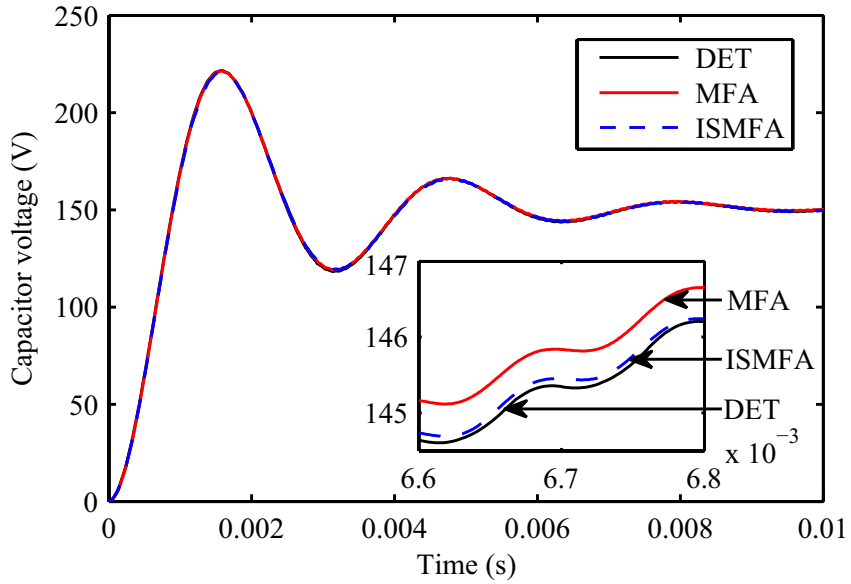

Figure 3.8: Simulation results of startup transient capacitor voltage for detailed (DET), (first-order) MFA, and ISMFA models.

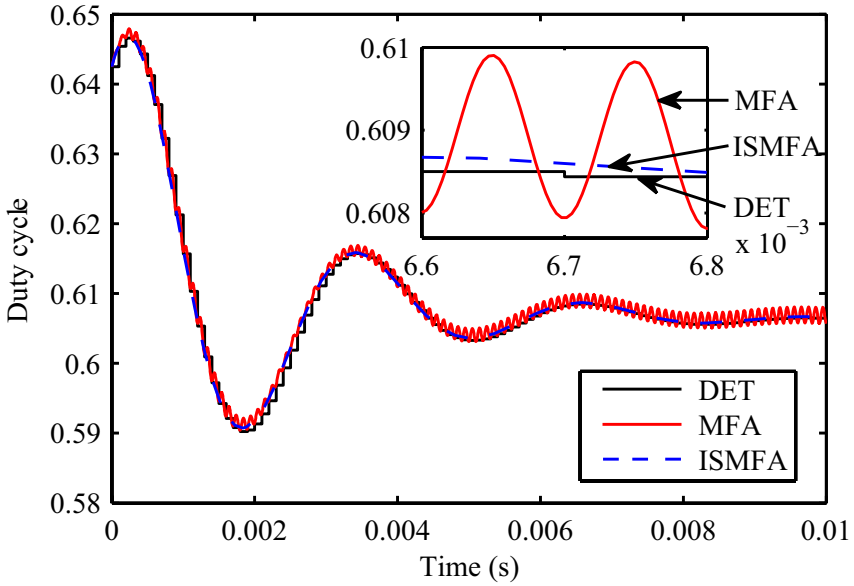

Figure 3.9: Simulation results of startup transient duty cycle for detailed (DET), (first-order) MFA, and ISMFA models.

To further understand the nature of the instability of the MFA model observed in Figure 3.10–3.12, the MFA model is linearized about the equilibrium point. The resulting Jacobian matrix is provided in Appendix A. It can be observed that one pair

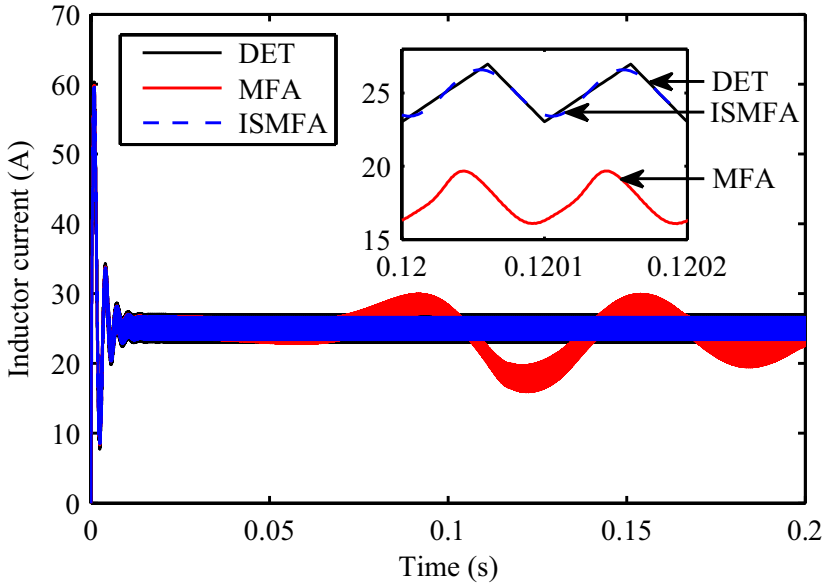

Figure 3.10: Simulation results of steady-state inductor current for detailed (DET), (first-order) MFA, and ISMFA models.

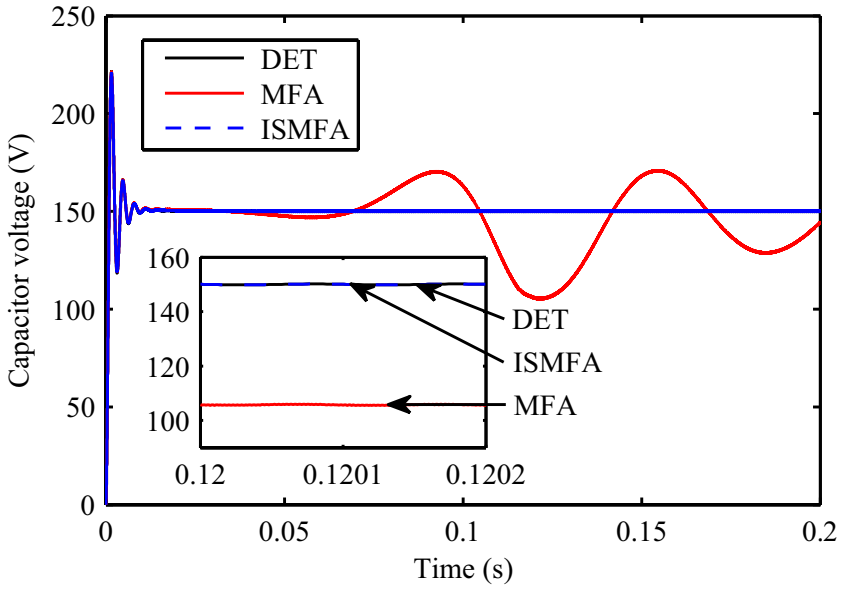

Figure 3.11: Simulation results of steady-state capacitor voltage for detailed (DET), (first-order) MFA, and ISMFA models.

of eigenvalues of the resulting Jacobian matrix lies in the right half plane, indicating that the MFA model is unstable. The ISMFA model has the same equilibrium point, but the time-varying nature of the feedback matrix in (3.19) causes the Jacobian

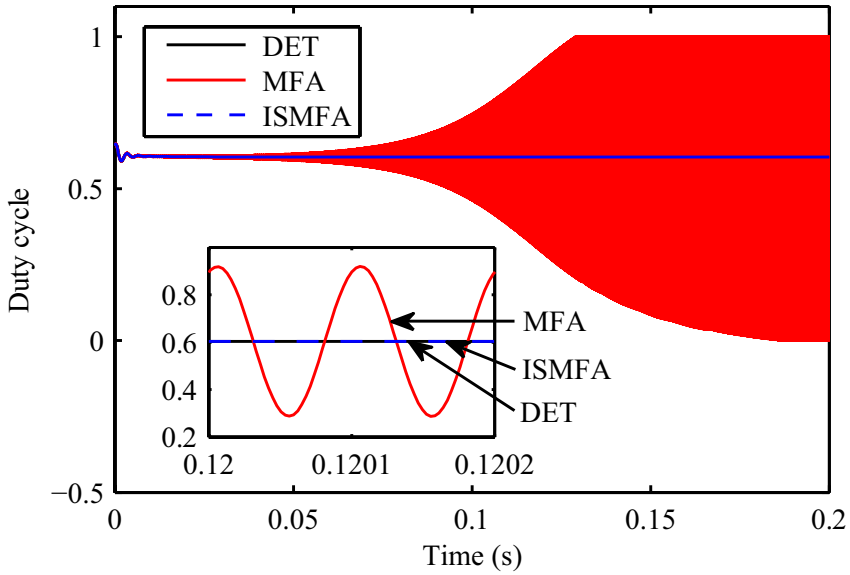

Figure 3.12: Simulation results of steady-state duty cycle for detailed (DET), (first-order) MFA, and ISMFA models.

matrix to depend on t, which yields

$$\mathbf{J}(\theta) = \mathbf{A}_0 + \cos(\theta)\mathbf{A}_1 + \sin(\theta)\mathbf{A}_2, \tag{3.34}$$

where $\mathbf{A}_0$, $\mathbf{A}_1$, and $\mathbf{A}_2$ are constant matrices provided in Appendix B and $\theta = \omega t$. As θ is varied such that $\cos(\theta)$ and $\sin(\theta)$ lie in $[-1, 1]$, the Jacobian matrix can be shown to be a convex combination of four constant matrices, i.e.,

$$\mathbf{J}(\theta) = \alpha_1(\theta)\mathbf{J}_1 + \alpha_2(\theta)\mathbf{J}_2 + \alpha_3(\theta)\mathbf{J}_3 + \alpha_4(\theta)\mathbf{J}_4, \tag{3.35}$$

where $\mathbf{J}_1$, $\mathbf{J}_2$, $\mathbf{J}_3$ and $\mathbf{J}_4$ are given by the following:

$$\begin{cases} \mathbf{J}_1 = \mathbf{A}_0 + \mathbf{A}_1 + \mathbf{A}_2 & \mathbf{J}_3 = \mathbf{A}_0 - \mathbf{A}_1 + \mathbf{A}_2 \\ \mathbf{J}_2 = \mathbf{A}_0 + \mathbf{A}_1 - \mathbf{A}_2 & \mathbf{J}_4 = \mathbf{A}_0 - \mathbf{A}_1 - \mathbf{A}_2 \end{cases} \tag{3.36}$$

If there exists a symmetric, positive definite matrix $\mathbf{P}$ that satisfies

$$\mathbf{J}_i^{\mathrm{T}}\mathbf{P} + \mathbf{P}\mathbf{J}_i < 0 \qquad \forall i \in \{1, 2, 3, 4\} \tag{3.37}$$

it can be shown that $\mathbf{J}(\theta)^{\mathrm{T}}\mathbf{P} + \mathbf{P}\mathbf{J}(\theta)$ is negative definite. Such a matrix $\mathbf{P}$ can be found by solving a linear matrix inequality problem, and a solution is given in Appendix B. Therefore, the ISMFA model is locally asymptotically stable about the equilibrium point.

3.4.3 Frequency-Domain Analysis

The frequency-domain characteristics associated with the proposed ISMFA are examined by considering the open-loop control-to-output behavior. In particular, perturbations to the modulation signal are introduced to either the dc-component (m_0) or to the first-order cosine component (m_{1c}). These perturbations represent low-frequency perturbations and perturbations about the switching frequency, respectively. Perturbations between 1 Hz and 1 kHz are injected into the detailed, SSA, and ISMFA models and the subsequent output voltage perturbations are extracted using the method described in [105]. The resulting magnitude and phase responses are shown in Figure 3.13 and Figure 3.14. It is observed that both the SSA and ISMFA models are capable of predicting the response of the system to perturbations in the dc component. However, only the ISMFA model can predict the response to perturbations to the first-order component, representing perturbations about the switching frequency. The erratic behavior exhibited by the SSA model in Figure 3.14 is due to the fact that the perturbation to the first-order component of the modulation signal is introduced as an equivalent higher frequency perturbation into the SSA model. This higher frequency perturbation exceeds the bandwidth of the SSA model, and therefore, it is unable to predict the response of the system to such perturbations.

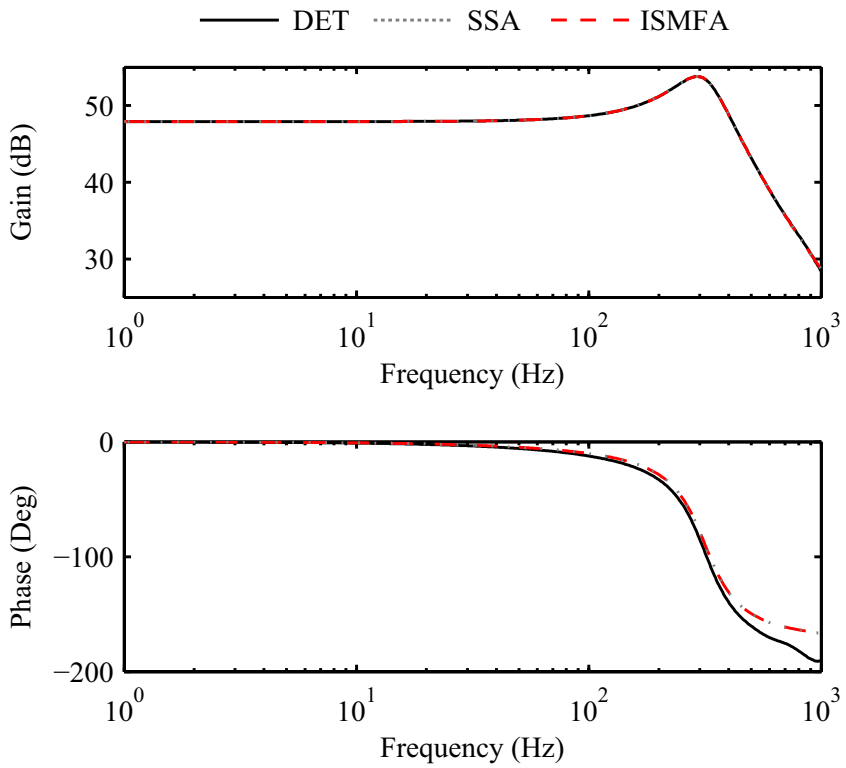

Figure 3.13: Gain and phase of responses to perturbations in the dc component of detailed (DET), SSA, and ISMFA models.

3.5 Experimental Validation

In order to validate the ISMFA model, a uniformly sampled PWM buck converter with the parameters given in Table 3.2 is studied experimentally. The control is implemented in a TMS320F28335 microcontroller. The PI control is implemented by sampling the output voltage at 100 kHz, which is sufficiently fast that the continuous representation in Figure 3.2 is appropriate. The 10 kHz uniformly sampled PWM is implemented using a shadow register to implement the zero-order hold depicted in Figure 2.4. A step load resistance change from 7.481 Ω to 6.622 Ω is applied, and the inductor current and output voltage are measured experimentally and compared with the simulation output of a detailed model and a first-order ISMFA model. This comparison is shown in Figure 3.15. It can be seen that the inductor current pre-

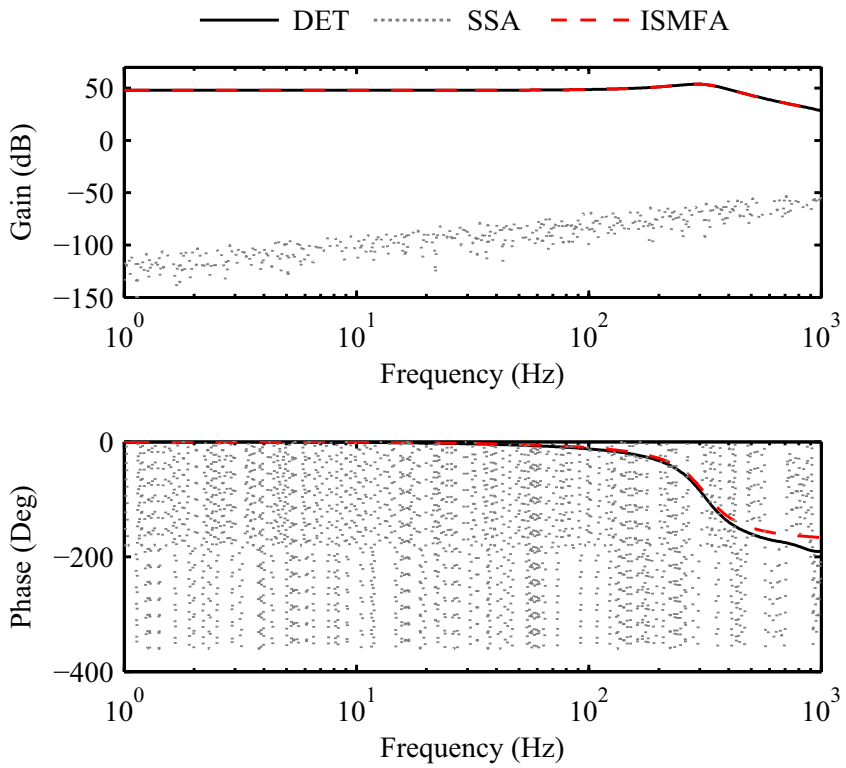

Figure 3.14: Gain and phase of responses to perturbations to the first-order component of detailed (DET), SSA, and ISMFA models.

dicted by the ISMFA model matches the experimentally measured inductor current very well. There appears to be a small shift between the measured and simulated output voltages. This minor discrepancy is likely due to small differences between parameter values in the simulation model and the actual converter and does not seem to significantly affect the accuracy of the model. It is noted that small deviations (e.g. switch bounce when switching load) can degrade the ability of the simulation models (both detailed and ISMFA) to predict the behavior of the converter exactly.

3.6 Conclusion

The ISMFA method of representing uniformly sampled PWM converters is proposed. Furthermore, an observed issue with model stability is described, and this issue is

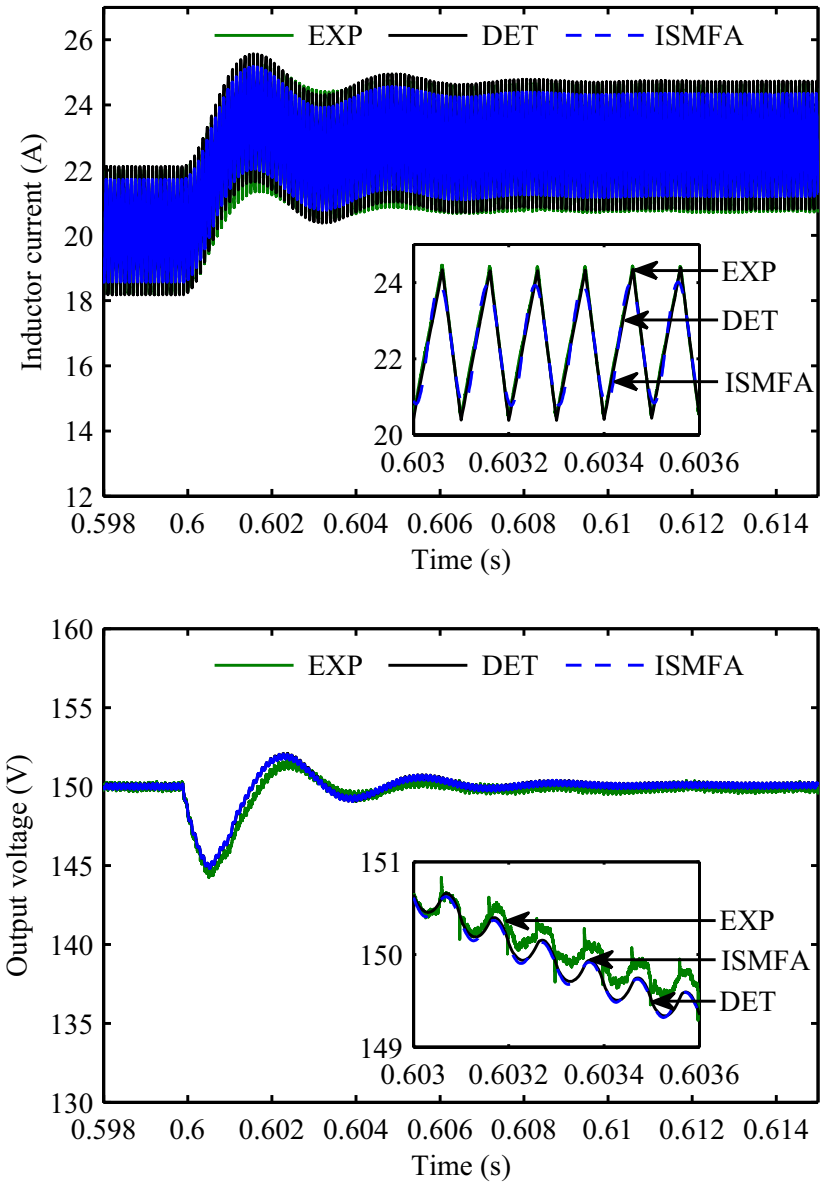

Figure 3.15: Step load change experimental (EXP) and simulation results for detailed (DET) and (first-order) ISMFA models. The experimental measurements are low-pass filtered with a time constant of 2 μs to remove measurement noise.

addressed by the proposed method. Simulation results of both transient and steady-state responses show that the proposed model provides an accurate prediction of system behavior and its small-signal behavior. The proposed model is validated experimentally by consideration of step load changes with a uniformly sampled dc-dc PWM buck converter. It is shown that the proposed ISMFA model is capable of

predicting the transient and steady-state behavior predicted by the detailed model and measured experimentally.

CHAPTER 4

MULTIFREQUENCY AVERAGING IN REGION OF ATTRACTION ESTIMATION OF POWER ELECTRONIC SYSTEMS

In this chapter, an reduced-order MFA (RMFA) model is proposed to perform ROA estimation of power electronic systems. Such a model allows the effects of switching harmonics to be included in the model without increasing the model order, permitting the effects of switching ripple to be considered in stability analysis. The contributions of this work are (i) the proposal to use RMFA models to perform ROA estimation in power electronic systems, (ii) demonstration of the failure of traditional ROA estimation using an SSA model by counterexample, (iii) demonstration of the success of the proposed method by exhaustive gridding, and (iv) experimental validation of the results. It is noted that the case study considered herein is for a buck converter and that the results could be applied equally to other power electronic systems or even to other systems that exhibit periodic oscillation in steady state.

The remainder of this chapter is organized as follows. Background results associated with ROA estimation are set forth in Section 4.1. Likewise, relevant details about the MFA modeling approach are presented in Section 4.2. The RMFA modeling approach is described in Section 4.3. The use of RMFA models for ROA estimation is proposed in Section 4.4. A buck converter with a constant power load and a controller is used for a case study and is detailed in Section 4.5. The simulation and experimental results associated with the case study are provided and discussed in Section 4.6. A concluding summary is provided in Section 4.7.

4.1 Region of Attraction Estimation

Herein, a dynamical autonomous system that satisfies

$$\frac{d\mathbf{x}}{dt} = \mathbf{f}(\mathbf{x}) \tag{4.1}$$

is considered, where $\mathbf{x} \in \mathbb{R}^n$ and $\mathbf{f} : \mathbb{R}^n \to \mathbb{R}^n$. It is also assumed that $\mathbf{f}$ satisfies the standard conditions for the existence and uniqueness of solutions to (4.1) given an initial condition $\mathbf{x}(t_0) = \mathbf{x}_0$ [106]. A solution $\mathbf{x}(t)$ of (4.1) corresponding to a curve in the state space as time varies from t_0 to infinity is generally referred to as a trajectory. An equilibrium point of (4.1) is defined as a point $\mathbf{x}_{\text{eq}} \in \mathbb{R}^n$ such that

$$\mathbf{0} = \mathbf{f}(\mathbf{x}_{\text{eq}}). \tag{4.2}$$

Without loss of generality, it is assumed that the equilibrium point of interest occurs at $\mathbf{x}_{\text{eq}} = \mathbf{0}$.

The ROA of an asymptotically stable equilibrium point is the set of initial states from which the system trajectories tend asymptotically towards the equilibrium point. Gridding-based techniques can be used to approximate the ROA by sampling points in the neighborhood of the equilibrium point. However, the high computational cost limits the application of these techniques. This creates a need for efficient techniques for constructing an ROA estimate. An ROA estimate is an invariant set of initial states from which the system trajectories tend asymptotically towards the equilibrium point. An ROA estimate is a subset of the ROA, and is often represented by a contour level of a positive definite function, e.g, a Lyapunov function.

Lyapunov's second method utilizes Lyapunov functions to determine the stability of the system described in (4.1) without explicitly integrating the differential equations. A Lyapunov function candidate, $V : \mathbb{R}^n \to \mathbb{R}$, must be locally positive

definite in some neighborhood B_r around the equilibrium point such that $V(\mathbf{x}) \geq 0$ for $\forall \mathbf{x} \in B_r$ with equality if and only if $\mathbf{x} = \mathbf{0}$. Assuming $V(\mathbf{x})$ is differentiable, if its derivative with respect to time evaluated along trajectories of (4.1), i.e.,

$$\dot{V}(\mathbf{x}) = \frac{dV(\mathbf{x})}{dt} = \frac{dV}{d\mathbf{x}}\frac{d\mathbf{x}}{dt} = \frac{dV}{d\mathbf{x}}\mathbf{f}(\mathbf{x}) \tag{4.3}$$

is locally negative definite in B_r, then the equilibrium point is asymptotically stable and all trajectories starting in B_r asymptotically converge to the equilibrium point. The functions $V(\mathbf{x})$ and $\dot{V}(\mathbf{x})$ are referred to as the Lyapunov function and the Lyapunov derivative, respectively.

Lasalle's principle yields sufficient conditions for a region to be an ROA estimate. Herein, a region defined in the form of

$$D(V, c) = \{\mathbf{x} \in \mathbb{R}^n : V(\mathbf{x}) \leq c\} \tag{4.4}$$

is considered, where $V(\mathbf{x})$ is a Lyapunov function and c is a Lyapunov function contour value. If $\dot{V}(\mathbf{x}) \leq 0$ for $\forall \mathbf{x} \in D(V, c)$, any trajectory starting within the region of $D(V, c)$ tends to the largest invariant set inside U, i.e.,

$$U = \left\{\mathbf{x} \in D(V, c) : \dot{V}(\mathbf{x}) = 0\right\}. \tag{4.5}$$

In particular, if U contains no invariant sets other than $\mathbf{x}_{eq}$, then $\mathbf{x}_{eq}$ is asymptotically stable and $D(V, c)$ is a subset of the ROA.

In order to use this approach for ROA estimation, an appropriate Lyapunov function must be identified. If the system described in (4.1) were linear, then the ROA of a stable equilibrium point would be the entire state space. The general case of a nonlinear system is considered herein. The problem of finding a Lyapunov function of such a nonlinear system that captures the nonlinear behavior of $\mathbf{f}$ around the

equilibrium point is highly nontrivial [107, 108]. A simple approach for deriving an appropriate Lyapunov function is referred to as a Jacobian diagonalization. First, the system is linearized about the equilibrium point:

$$\frac{d\mathbf{x}}{dt} = \mathbf{J}\mathbf{x} + \mathbf{f}_{\text{h.o.t}}(\mathbf{x}), \tag{4.6}$$

where $\mathbf{J}$ is the Jacobian matrix of f evaluated at the origin and $\mathbf{f}_{\text{h.o.t}}$ contains only higher order terms in $\mathbf{x}$. Practically, higher order terms are simply neglected in the linearized approximation in the neighborhood of the origin. The linearization only captures the local behavior of the state space around the equilibrium point. Nonetheless, it is sufficient for finding an ROA estimate where the dynamical autonomous system behaves similarly to its linearized approximation for small range motions.

If the Jacobian matrix is assumed to be diagonalizable, the eigenvalue decomposition can be expressed as

$$\mathbf{J} = \mathbf{S}\mathbf{\Lambda}\mathbf{S}^{-1}, \tag{4.7}$$

where $\mathbf{S} \in \mathbb{C}^{n\times n}$ and $\mathbf{\Lambda} \in \mathbb{C}^{n\times n}$ is a diagonal matrix where each diagonal entry is a corresponding eigenvalue of $\mathbf{J}$. If a state transformation $\mathbf{z} = \mathbf{S}^{-1}\mathbf{x}$ is considered, the linearized model can be expressed as

$$\frac{d\mathbf{z}}{dt} = \mathbf{\Lambda}\mathbf{z}. \tag{4.8}$$

A simple positive definite quadratic Lyapunov candidate function can be constructed $V(\mathbf{z}) = \mathbf{z}^{\text{H}}\mathbf{z}$ [109], where the superscript H is the complex conjugate transpose. The derivative of $V(\mathbf{z})$ with respect to time evaluated along trajectories yields

$$\frac{dV(\mathbf{z})}{dt} = \frac{d}{dt}\left(\mathbf{z}^{\text{H}}\mathbf{z}\right) = \mathbf{z}^{\text{H}}\left(\mathbf{\Lambda}^{\text{H}} + \mathbf{\Lambda}\right)\mathbf{z} = 2\mathbf{z}^{\text{H}}\text{Re}(\mathbf{\Lambda})\mathbf{z}. \tag{4.9}$$

It can be observed that the Lyapunov derivative is negative definite if the real parts of the diagonal entries of $\mathbf{\Lambda}$ are negative (they are the real parts of the eigenvalues of $\mathbf{A}$), which is true for an asymptotically stable equilibrium point. The resulting Lyapunov function in terms of $\mathbf{x}$ is

$$V(\mathbf{x}) = \mathbf{x}^{\mathrm{T}}\mathbf{S}^{-\mathrm{H}}\mathbf{S}^{-1}\mathbf{x}. \tag{4.10}$$

Given a Lyapunov function $V(\mathbf{x})$, the problem of finding the largest contour value c that bounds an ROA estimate is formulated as an optimization problem:

$$c = \min\left\{V(\mathbf{x}) : \dot{V}(\mathbf{x}) \geq 0\right\}. \tag{4.11}$$

Genetic algorithms (GAs) are capable of solving nonlinear optimization problems with high-dimensional search spaces [110]. Herein, a method of applying GAs to the problem (4.11) is used. The objective is to generate an upper bound on the contour value that will be used to define the boundary of the ROA estimate. GAs are usually formulated to maximize a fitness function f_{fit}, so a particular fitness function for the minimization problem (4.11) can be constructed as

$$f_{\mathrm{fit}}(\mathbf{x}) = -V(\mathbf{x}) - p(\mathbf{x}), \tag{4.12}$$

where $p(\mathbf{x})$ is an additive penalty function used to enforce the constraint of optimization problem (4.11). It assumes a large positive value M when the constraint is not met and zero when the constraint is met:

$$p(\mathbf{x}) = \begin{cases} 0, & \text{if } \frac{dV(\mathbf{x})}{dt} \geq 0 \\ M, & \text{otherwise.} \end{cases} \tag{4.13}$$

4.2 Multifrequency Averaging

Power electronic circuits exhibit periodic switching in steady state, and this switching gives rise to switching ripple in the currents and voltages of the circuit. SSA models have been used in many applications shown in Section 2.1. These models are averaged over one switching period and, as a result, do not convey the switching behavior of the circuits. ROA esimation has been performed using SSA models of power electronic systems [40–44], but these systems have generally satisfied a small ripple assumption [19].

MFA models are applied herein for estimating ROAs of converters. In such models, the average behavior as well as low-order components of the ripple behavior can be predicted. The MFA method and the properties of partial-Fourier-series approximations that are useful for the use of the MFA method are described in Section 2.2.1–2.2.5.

In feedback control, a modulation signal $m(t)$ is constructed and used to control the switching of the converter. Herein, naturally sampled PWM with trailing edge modulation described in Section 2.4.2 is considered. In this setting, the switching function $q(t)$ is the result of comparing the modulation signal with a sawtooth carrier $c(t)$. If the modulation signal is represented using a Kth-order approximation, the nominal duty cycle D, which describes the percentage of "on-time" of the switching function $q(t)$ in each switching cycle, can be found by equating the reconstructed modulation signal with the sawtooth carrier, which yields [20]

$$h(\mathbf{m}, D) = \boldsymbol{\theta}^{\mathrm{T}}(DT)\mathbf{m} - D = 0, \tag{4.14}$$

where T is the switching period. The resulting solution D should be projected if necessary to lie in $[0, 1]$. It has been shown in [20] that the use of averages in (2.38)–(2.40) to generate $q(t)$ is valid in closed-loop configurations when D is relatively slowly

varying. Alternative methods of solving the algebraic relationship in (4.14) have been proposed. In [20], an additional state variable is added. One or more Newton steps are employed in [29]. Herein, the algebraic relationship is enforced as part of the model order reduction described below.

4.3 Reduced-Order Multifrequency Averaging

In an MFA model, each state variable in the original model is represented using $2K + 1$ state variables. This increases the order of the system model and increases the dimensionality of the search space in (4.11). In [20], a condensed MFA (CMFA) approach is presented, but this approach requires a constant Jacobian matrix, a condition that does not hold for nonlinear systems. Herein, an alternative method of model order reduction described in [111] is used. A Kth-order approximated MFA model of a system can be described as

$$\frac{d\mathbf{x}_f}{dt} = \mathbf{f}(\mathbf{x}_f, \mathbf{x}_h, D) \tag{4.15}$$

$$\frac{d\mathbf{x}_h}{dt} = \mathbf{g}(\mathbf{x}_f, \mathbf{x}_h, D) \tag{4.16}$$

$$h(\mathbf{x}_f, \mathbf{x}_h, D) = 0 \tag{4.17}$$

where vectors $\mathbf{x}_f$ and $\mathbf{x}_h$ collect the fundamental averages (e.g., x_0) and harmonic averages (e.g., x_{1c}, x_{1s}, ...) of the state variables, respectively. Conventional state-space averaging only considers the fundamental averages in (4.15). Herein, $\mathbf{x}_f$ and $\mathbf{x}_h$ are treated as "slow" and "fast" components with respect to time. A similar approach is used in [20], where a selective modal analysis reduction procedure is utilized to arrive a CMFA model. This decomposition is made possible by a Jacobian matrix that is independent of operating point, precluding the use of this method for nonlinear systems. Therefore, an RMFA model using a singular perturbation approach [112] to reduce the Kth-order full system to a fundamental system that approximately

accounts for the interaction between the "slow" (i.e., (4.15)) and "fast" (i.e., (4.16)) subsystems is used:

$$\frac{d\bar{\mathbf{x}}_f}{dt} = \mathbf{f}\left(\bar{\mathbf{x}}_f, \bar{\mathbf{x}}_h, \bar{D}\right) \tag{4.18}$$

$$\mathbf{g}\left(\bar{\mathbf{x}}_f, \bar{\mathbf{x}}_h, \bar{D}\right) = \mathbf{0} \tag{4.19}$$

$$h(\bar{\mathbf{x}}_f, \bar{\mathbf{x}}_h, \bar{D}) = 0 \tag{4.20}$$

where $\bar{\mathbf{x}}_f$, $\bar{\mathbf{x}}_h$, and $\bar{D}$ in the RMFA model correspond to $\mathbf{x}_f$, $\mathbf{x}_h$, and D, respectively, in the MFA model. The "fast" component $\bar{\mathbf{x}}_h$ is solved using the steady-state relationship obtained by setting $d\bar{\mathbf{x}}_h/dt = \mathbf{0}$ in (4.16). The vinculum notation is used here to differentiate the variables of the MFA and RMFA models, but this notation is not used below.

Generally, $\mathbf{x}_h$ is implicit in (4.19) and can not be expressed explicitly as a function of $\mathbf{x}_f$. Likewise, the duty cycle D in (4.20) cannot be solved explicitly. Therefore, given $\mathbf{x}_f$, it is necessary to solve

$$\mathbf{g}\left(\mathbf{x}_f, \mathbf{x}_h, D\right) = \mathbf{0} \tag{4.21}$$

$$h\left(\mathbf{x}_f, \mathbf{x}_h, D\right) = 0 \tag{4.22}$$

for $\mathbf{x}_h$ and D. Since the solution $\mathbf{x}_h$ and D to the nonlinear equations (4.21) and (4.22) cannot be expressed explicitly, the Newton-Raphson method is applied here for estimating the solution using numerical iteration. The kth iteration of the Newton-Raphson method is given by

$$\begin{bmatrix} \mathbf{x}_h^{(k+1)} \\ D^{(k+1)} \end{bmatrix} = \begin{bmatrix} \mathbf{x}_h^{(k)} \\ D^{(k)} \end{bmatrix} - \left(\mathbf{J}^{(k)}\right)^{-1} \begin{bmatrix} \mathbf{g}(\mathbf{x}_f, \mathbf{x}_h^{(k)}, D^{(k)}) \\ h(\mathbf{x}_f, \mathbf{x}_h^{(k)}, D^{(k)}) \end{bmatrix}, \tag{4.23}$$

where $\mathbf{J}^{(k)}$ is the Jacobian matrix of $[\mathbf{g}(\cdot,\cdot,\cdot)\ h(\cdot,\cdot,\cdot)]^{\mathrm{T}}$ evaluated at $\mathbf{x}_f$, $\mathbf{x}_h^{(k)}$, and $D^{(k)}$. The algorithm stops if convergence is reached:

$$\left\| \begin{bmatrix} \mathbf{g}^{(k)} \\ h^{(k)} \end{bmatrix} \right\| \leq \epsilon, \tag{4.24}$$

where ϵ is the given tolerance. Alternatively, a fixed number of iterations may be performed.

The speed of convergence to the solution in the Newton Raphson method depends on the selection of initial guess value. The initial guess value of $\mathbf{x}_h^{(0)}$ is usually zero. An appropriate initial guess for the duty cycle is based on m_0, which can be calculated using the fundamental averages $\mathbf{x}_f$. The initial value $D^{(0)}$ can be set to m_0. Alternatively, a single Newton step can be used to calculate

$$D^{(0)} = m_0 - \frac{h(\mathbf{x}_f, \mathbf{0}, m_0)}{h'(\mathbf{x}_f, \mathbf{0}, m_0)}, \tag{4.25}$$

where $h'(\cdot,\cdot,\cdot)$ is the partial derivative of $h(\cdot,\cdot,\cdot)$ with respect to D.

With small values of ϵ (on the order of 10^{-6}), no more than five Newton-Raphson steps are required for convergence for the system studied herein. The RMFA model allows the effects of switching harmonics to be included in the model without increasing the model order, permitting the effects of switching ripple to be considered in stability analysis.

4.4 Region of Attraction Estimation with Reduced-Order Multifrequency Averaging

It is proposed herein to utilize the RMFA model of a system in order to perform ROA estimation. In this way, the effects of switching ripple on the stability of the system

can be considered without increasing the model order. The proposed method is as follows:

1. The MFA model of the system under consideration is constructed using the properties in Section 4.2 and partitioned as in (4.15)–(4.17).

2. The equilibrium point of interest is identified.

3. The Jacobian matrix of the MFA model is determined at the equilibrium point such that

$$\mathbf{J}_{MFA} = \left[\begin{array}{c|cc} \frac{\partial \mathbf{f}}{\partial \mathbf{x}_f} & \frac{\partial \mathbf{f}}{\partial \mathbf{x}_h} & \frac{\partial \mathbf{f}}{\partial D} \\ \hline \frac{\partial \mathbf{g}}{\partial \mathbf{x}_f} & \frac{\partial \mathbf{g}}{\partial \mathbf{x}_h} & \frac{\partial \mathbf{g}}{\partial D} \\ \frac{\partial h}{\partial \mathbf{x}_f} & \frac{\partial h}{\partial \mathbf{x}_h} & \frac{\partial h}{\partial D} \end{array}\right] = \left[\begin{array}{cc} \mathbf{J}_{11} & \mathbf{J}_{12} \\ \mathbf{J}_{21} & \mathbf{J}_{22} \end{array}\right]. \tag{4.26}$$

4. The Jacobian matrix of the RMFA model is given by

$$\mathbf{J}_{RMFA} = \mathbf{J}_{11} - \mathbf{J}_{12}\mathbf{J}_{22}^{-1}\mathbf{J}_{21}. \tag{4.27}$$

5. The Jacobian matrix of the RMFA model is used with the results of Section 4.1 to construct a Lyapunov function for the RMFA model.

6. A GA is used to solve the optimization problem in (4.11) using the fitness function in (4.12). The Lyapunov derivative is evaluated using the RMFA model.

7. The determined contour value c defines the boundary of the ROA estimate.

4.5 Case Study: System

As a case study of the proposed use of RMFA models to perform ROA estimation, the buck converter shown in Figure 4.1 is studied. The buck converter feeds a constant power load, which can represent a downstream converter that draws constant power irrespective of changes to input voltage. An active droop controller shown in

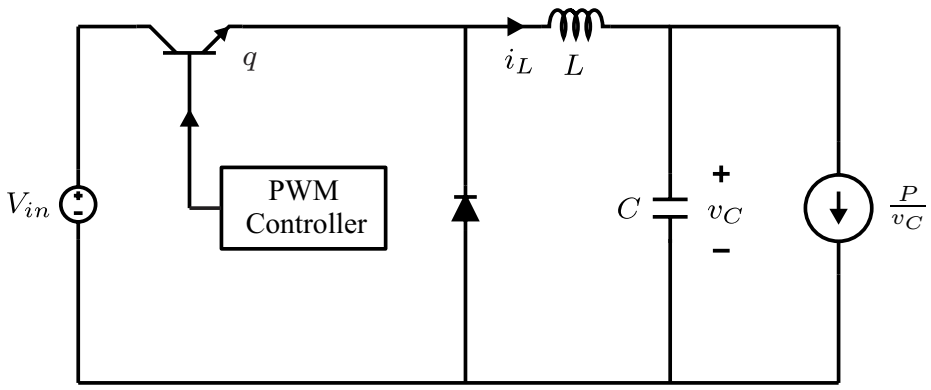

Figure 4.1: Buck converter with a constant power load.

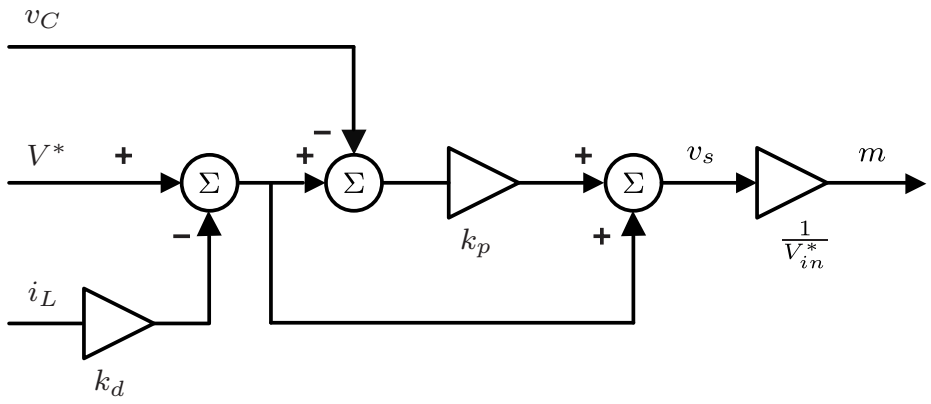

Figure 4.2: Active droop controller

Table 4.1: Parameters of Dc/Dc Buck Converter

f	2 kHz	L	1.52 mH	C	167 µF
V_{in}^*	250 V	k_p	2.2	k_d	0.8 V/A
V_{in}	250 V	V^*	200 V	P	2.5 kW
V_{in0}	250 V	V_0^*	200 V	P_0	2.5 kW
V_{inkc}	0 V	V_{kc}^*	0 V	P_{kc}	0 W
V_{inks}	0 V	V_{ks}^*	0 V	P_{ks}	0 W

Figure 4.2 is used to regulate the output voltage of the converter. The parameters of the system are given in Table 4.1. The detailed and MFA models of the system are described below.

4.5.1 Detailed Model

The detailed model of the buck converter with a constant power load is given as

$$L\frac{di_L}{dt} = V_{in}q - v_C \tag{4.28}$$

$$C\frac{dv_C}{dt} = i_L - \frac{P}{v_C} \tag{4.29}$$

where q is the switching function that takes values of zero and one corresponding to the transistor being open or closed, respectively.

Active droop control is a commonly used feedback control technique for regulating the output voltage of a converter [113–115]. Herein, the inductor current is sensed and fed back to adjust the output voltage reference V^*. The modulation signal $m(t)$ required to regulate the output voltage is calculated using an adjusted output voltage error and a feed forward adjusted output voltage reference as the input to the controller, depicted in Figure 4.2. The detailed model of the active droop controller can be described as

$$v_s = V^* - k_d i_L + k_p(V^* - k_d i_L - v_C) \tag{4.30}$$

$$m = \frac{v_s}{V_{in}^*} \tag{4.31}$$

where k_d and k_p are control parameters and V_{in}^* is the nominal value of the input voltage V_{in}. The modulation signal is used to compute the switching function in naturally sampled PWM with trailing edge modulation, shown in Section 2.4.2.

4.5.2 MFA Model

By applying the properties described in Section 4.2, an MFA model of the converter system is developed. If each signal in the detailed model described in (4.28) and (4.29) is approximated by a Kth-order series, then the following MFA model for the

buck circuit arises:

$$L(\mathbf{T}\mathbf{i}_L + \frac{d\mathbf{i}_L}{dt}) = \mathbf{\Phi}(\mathbf{V}_{in})\mathbf{q} - \mathbf{v}_C \tag{4.32}$$

$$C(\mathbf{T}\mathbf{v}_C + \frac{d\mathbf{v}_C}{dt}) = \mathbf{i}_L - \mathbf{\Phi}(\mathbf{v}_C)^{-1}\mathbf{P}. \tag{4.33}$$

Similarly, the MFA model of the active droop controller described in (4.30) and (4.31) can be given as

$$\mathbf{v}_s = \mathbf{V}^* - k_d\mathbf{i}_L + k_p(\mathbf{V}^* - k_d\mathbf{i}_L - \mathbf{v}_C) \tag{4.34}$$

$$\mathbf{m} = \frac{\mathbf{v}_s}{V_{in}^*}. \tag{4.35}$$

The relationship between the modulation average vector $\mathbf{m}$ and the duty cycle D is given in (4.14), and the duty cycle can be used in (2.38)–(2.40) to find the average vector of the switching function $\mathbf{q}$.

4.6 Case Study: Results

In order to demonstrate the proposed use of RMFA models is ROA estimation, ROA estimation is performed for the system described above using both the traditional SSA model and the proposed RMFA model. The GA used for these studies is GOSET [116], an open-source MATLAB toolbox, using its default parameters with a population size of 200 and 200 generations. The RMFA model used herein is based on a first-order approximation of the switching ripple.

4.6.1 ROA Estimation in Average Space

Both the SSA and the RMFA models are averaged models, and their corresponding ROA estimates are computed in terms of the averaged inductor current and capacitor voltage. The ROA estimates derived from these models are shown in Figure 4.3. It is

observed that the ROA estimate derived from the RMFA model, which includes the effects of switching ripple, is smaller than that derived from the SSA model.

Two trajectories, one (A) originating from inside the ROA estimate derived from the RMFA model and the other (B) originating from outside the ROA estimate derived from the RMFA model but inside the ROA estimate derived from the SSA model, are simulated using the detailed model. The simulated trajectories include switching harmonics, but these trajectories are averaged such that

$$\bar{x}(t) = \frac{1}{T}\int_{t-T}^{t} x(\tau)\ d\tau. \tag{4.36}$$

It is observed that the trajectory A originating inside the ROA estimate predicted by the RMFA model converges to the equilibrium point without leaving the ROA estimate. Furthermore, the trajectory B originating outside the ROA estimate predicted by the RMFA model does not approach the equilibrium point. The trajectory approaches but does not enter the ROA estimate predicted by the RMFA model as it oscillates with increasing amplitude until voltage collapse occurs. This suggests that the "ROA estimate" predicted by the SSA model is not a true estimate of the ROA.

4.6.2 ROA Estimation in Instantaneous Space

In order to study the properties of the ROA estimates predicted by each method more carefully, it is necessary to understand the relationship between averaged and instantaneous values. Any averaged value $\mathbf{x}_f$ corresponds to an instantaneous value $\mathbf{x}(t)$ that contains fundamental and harmonic components. While the ROA estimate associated with the RMFA model shown in Figure 4.3 is expressed in terms of $\mathbf{x}_f$, the boundary of the same ROA estimate will be time-varying if expressed in terms $\mathbf{x}(t)$. In particular, each point on the boundary of the ROA estimate in the average space will correspond to an oscillating value in the instantaneous space.

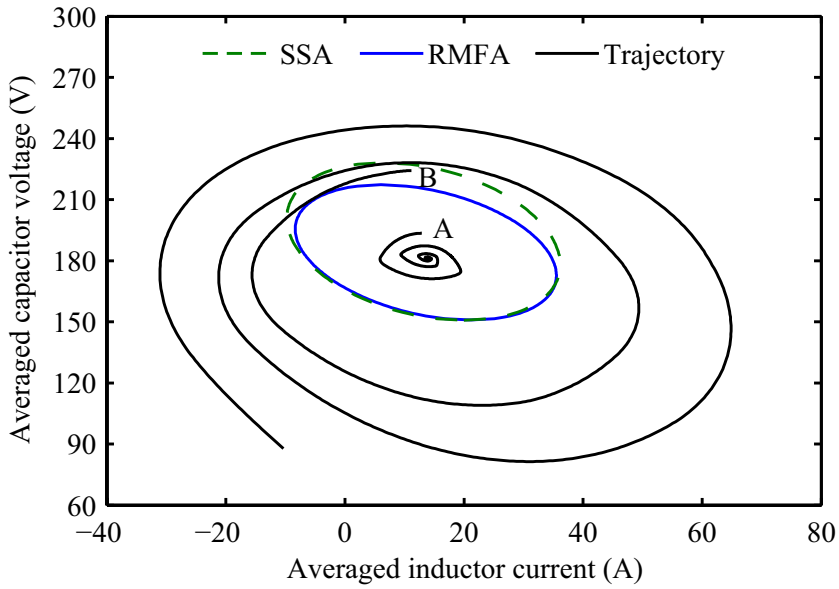

Figure 4.3: Region of attraction estimates predicted by the state-space-averaging and reduced-order-multifrequency-averaging models in the average space and two example averaged trajectories predicted by the detailed model

In particular, any fundamental average $\mathbf{x}_f$ is associated with resulting harmonic averages $\mathbf{x}_h$ by virtue of (4.21) and (4.22). These average values can be mapped to an instantaneous value using (2.21). If the phase angle is defined such that $\theta = \omega t$, then any average value can be mapped to an instantaneous value for any phase angle θ. This relationship is important when comparing results from the detailed model, which uses instantaneous values, to the RMFA model, which uses averaged values. In the case of the SSA model, which lacks any harmonic information, an identity mapping is assumed.

Having established relationships between the averaged and instantaneous values, it is possible to transform the ROA estimates predicted by the models from the average space to the instantaneous space. This transformation is shown in Figure 4.4–4.6 for three values of delay angle: $\theta = 0°$, $120°$, and $240°$. It can be seen that the ROA boundary predicted by the RMFA model shifts with respect to phase angle in the instantaneous space. For comparison, the instantaneous space is gridded from -40 A

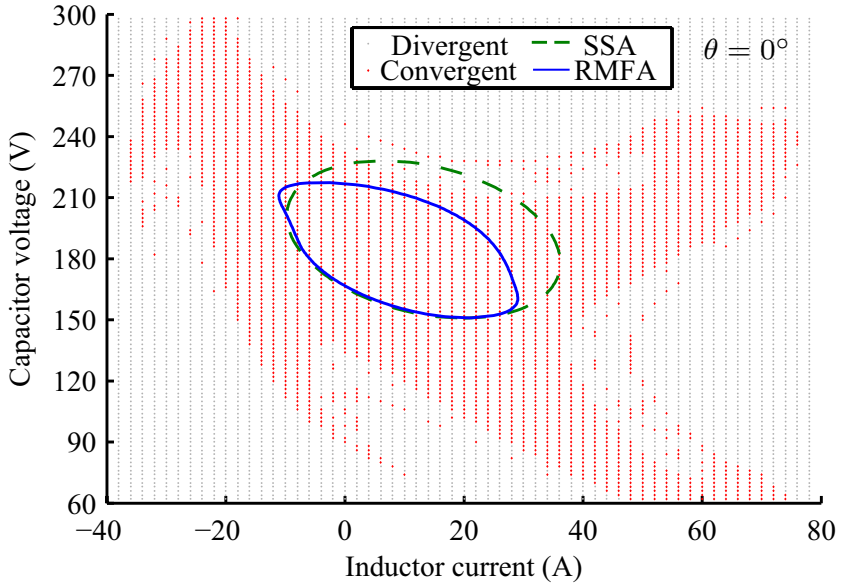

Figure 4.4: Region of attraction estimates predicted by the state-space-averaging and reduced-order-multifrequency-averaging models in the instantaneous space for phase angle of 0° and convergent/divergent status of grid points predicted by the detailed model

to 40 A with a spacing of 2 A for the inductor current and from 60 V to 300 V with a spacing of 2 V for the capacitor voltage. The detailed model is simulated starting at each grid point and for each phase angle. The detailed model is simulated for 0.4 s, and a trajectory is deemed convergent if the final value is within 1% of the steady-state range of the inductor current and the capacitor voltage as predicted by the detailed model (i.e., $[5.5, 22.2]$ A and $[178, 185]$ V). Otherwise, the trajectory is deemed divergent. The convergent/divergent status of each grid point is also shown in Figure 4.4–4.6. It can be observed that the shifting ROA estimate predicted by the RMFA model remains inside the ROA suggested by the grid of detailed model simulated trajectories. Furthermore, the ROA estimate predicted by the SSA models include points from which divergent trajectories originate for each of the three phase angles depicted.

In order to remove the phase angle dependence of the ROA estimate predicted by the RMFA model in the instantaneous space, the intersection of the ROA estimates

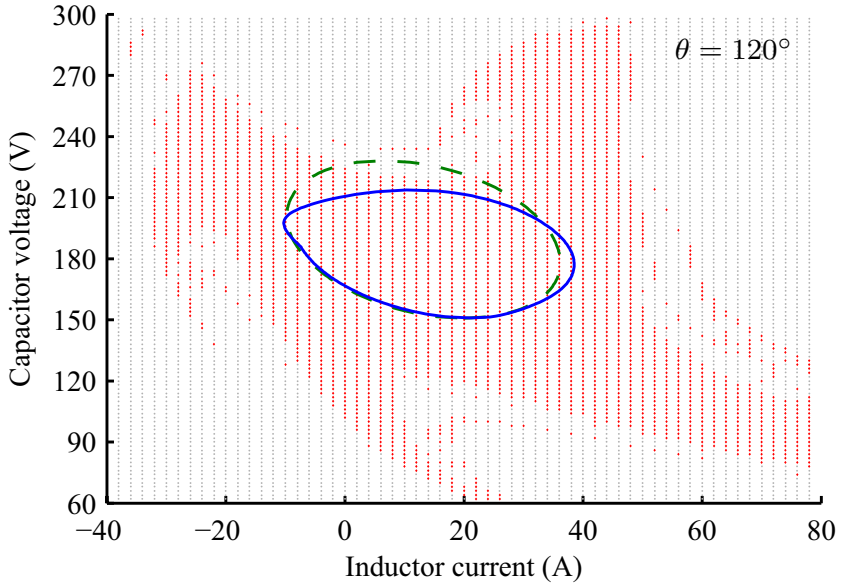

Figure 4.5: Region of attraction estimates predicted by the state-space-averaging and reduced-order-multifrequency-averaging models in the instantaneous space for phase angle of 120° and convergent/divergent status of grid points predicted by the detailed model

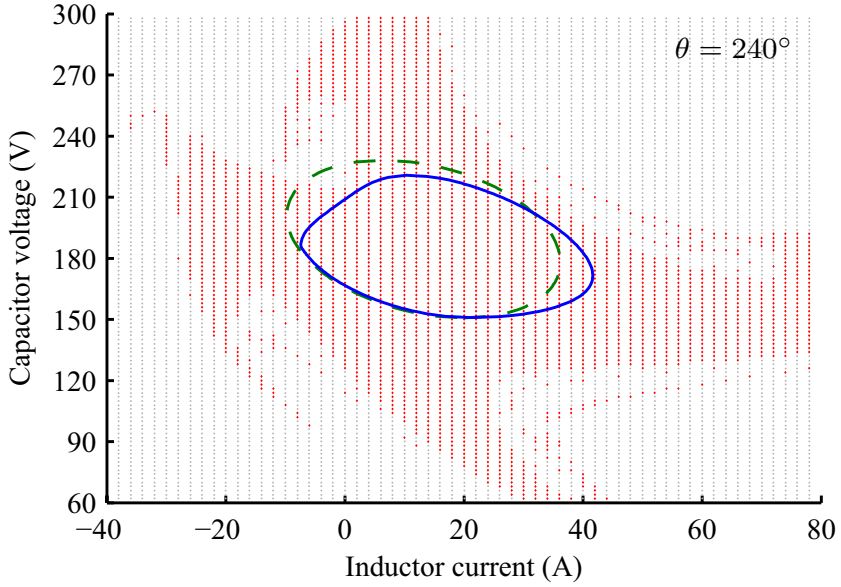

Figure 4.6: Region of attraction estimates predicted by the state-space-averaging and reduced-order-multifrequency-averaging models in the instantaneous space for phase angle of 240° and convergent/divergent status of grid points predicted by the detailed model

for each phase angle was calculated. Phase angles spanning 0° to 360° with a spacing of 2.4° are considered. The resulting intersection representing the ROA estimate predicted by the RMFA model in the instantaneous space as well as the ROA estimate predicted by the SSA model are shown in Figure 4.7. Furthermore, points in grid of the instantaneous space are deemed convergent if the trajectories are convergent for each of the phase angles. If a trajectory originating at the point is divergent for any of the phase angles, the point is deemed divergent. The initial conditions for the trajectories A and B shown in Figure 4.3 are also shown in Figure 4.7. The convergent points are points within the instantaneous space for which trajectories originating at these points at any time will converge to the equilibrium point. It can be seen that the ROA estimate predicted by the RMFA model only includes convergent points. The ROA estimate predicted by the SSA model includes points for which there exists times at which a trajectory originating at one of these points is divergent. While the use of the traditional SSA model yields inaccurate ROA estimates, it is clear that the use of the RMFA model for ROA estimation results in an ROA estimate that is more accurate and that does not appear to contain any divergent trajectories.

4.6.3 Experimental Results

In order to validate the proposed use of RMFA models in ROA estimation as described in Section 4.4, the buck converter and the feedback controller with the parameters given in Table 4.1 are studied experimentally. The converter is loaded with a pulse-width-modulated voltage source inverter supplying power to a three-phase balanced resistive load. The inverter output is tightly regulated, resulting in approximately constant inverter power consumption irrespective of dc voltage variations. The operating point of the converter is determined by its reference voltage V^*. Reference voltages corresponding to the initial conditions of trajectories A and B in Figure 4.3 are considered. The reference voltage is stepped to the value given in Table 4.1,

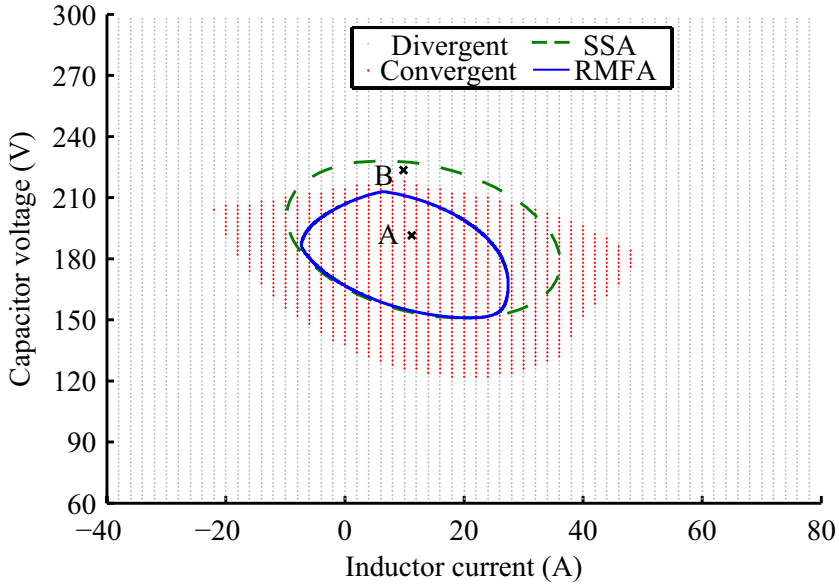

Figure 4.7: Region of attraction estimates predicted by the state-space-averaging and reducted-order-multifrequency-averaging models in the instantaneous space, convergent/divergent status of grid points predicted by the detailed model for all phase angles, and initial conditions of trajectories A and B

and the resulting capacitor voltage is observed. The capacitor voltage corresponding to trajectory A, which originates inside the ROA estimate predicted by the RMFA model, is shown in Figure 4.8. The capacitor voltage includes the expected switching ripple, but it can be seen that the capacitor voltage exhibits a stable step response and settles to the new equilibrium point. In contrast, the capacitor voltage corresponding to trajectory B, which originates outside the ROA estimate predicted by the RMFA model but inside the ROA estimate predicted by the SSA model, is shown in Figure 4.9. The initial voltage exhibits similar switching ripple. Unlike the trajectory depicted in Figure 4.3, a voltage collapse is not observed. This is because the inverter cannot behave like a constant power load over the entire range of voltages. Instead, the capacitor voltage exhibits an undesirable limit cycle behavior. This oscillation is low frequency (approximately 500 Hz) with respect to switching frequency of 2 kHz. The magnitude of the oscillation (approximately 20 V, peak-to-peak) also far exceeds the magnitude of the switching ripple (approximately 7 V, peak-to-peak). Thus, the

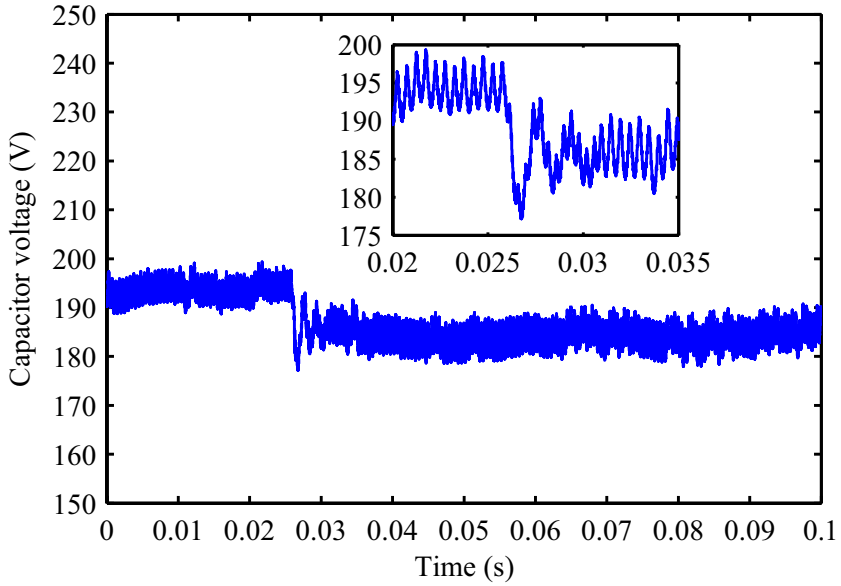

Figure 4.8: Experimentally measured capacitor voltage for step voltage reference voltage change corresponding to trajectory A (low-pass filtered with a time constant of 10 µs to remove measurement noise)

trajectory originating from within the ROA estimate predicted by the RMFA model is seen experimentally to be stable, but the trajectory originating from outside the ROA estimate predicted by the RMFA model but inside the ROA estimate predicted by the SSA model is seen experimentally to be unstable.

4.7 Conclusion

The use of RMFA models for ROA estimation is proposed as an alternative to the traditional use of SSA models. As RMFA models are capable of representing the switching behavior without increasing model order, they are suited for stability analysis even in cases where the switching ripple is considerable. It is shown that the ROA estimates produced by the SSA model can overestimate the true ROA of a system. Example trajectories are studied to illustrate how trajectories originating outside of the ROA estimate predicted by the RMFA model but inside the ROA estimate predicted by the SSA model can be divergent. Exhaustive gridding of the state-space

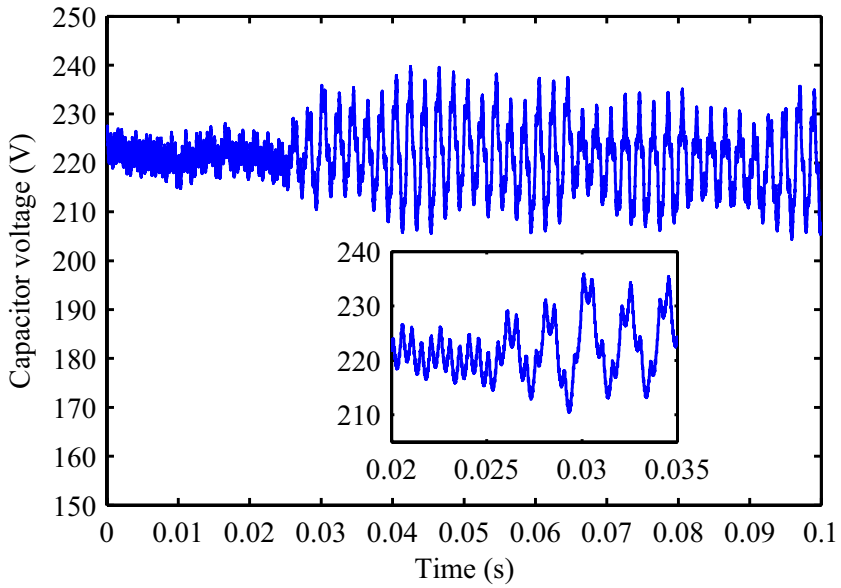

Figure 4.9: Experimentally measured capacitor voltage for step voltage reference voltage change corresponding to trajectory B (low-pass filtered with a time constant of 10 µs to remove measurement noise)

is employed to demonstrate that the ROA estimate predicted by the RMFA model contains no points from which divergent trajectories originate. This observation is further validated experimentally. In particular, the trajectory located within the ROA estimate predicted by the RMFA model is found to be stable experimentally, but the trajectory located outside the ROA estimate predicted by the RMFA model but inside the ROA estimate predicted by the SSA model is found to be unstable experimentally. Thus, the use of RMFA models for ROA estimation is found to be more accurate than the use of SSA models for systems in which the switching ripple is not negligible.

CHAPTER 5

MULTIFREQUENCY AVERAGING IN DIGITALLY CONTROLLED PWM CONVERTERS

Discrete-time controllers have attracted increasing interest due to the rapid evolution of digital integrated circuit technologies applied to signal processors, analog to digital converters and digital to analog converters [89–91]. Discrete-time models have been traditionally studied to model power electronic converters and the discrete-time controllers as discussed in Section 2.3. These models carefully describe the nonlinear dynamics of the systems but generally require relatively long simulation run times (compared to averaged models) because the simulation time step of the discrete-time models is limited by the sampling rate. It has been shown in Section 2.1 that the SSA models have been studied specifically to design and analyze discrete-time controllers. Theses approaches start from the linearized model of the converter power stage and the continuous-time controller. The discrete-time model is derived from the SSA model of the controller using discretization approximations (e.g., forward or backward Euler, bilinear). However, the successful application of the SSA models have been limited to power electronic converters that satisfy a small ripple assumption. MFA model has been shown in Section 2.2 to be capable of predicting the average behavior as well as low-order components of the ripple behavior. In this chapter, a continuous-time MFA representation of discrete-time systems is proposed. The contributions of this work are (i) the proposal of a method of representing discrete-time systems using continuous-time MFA, (ii) demonstration of the failure of traditional MFA model and proposed ISMFA model in Chapter 3 and the success of proposed method herein on a digitally controlled PWM converter, (iii) experimental validation of the results.

The remainder of this chapter is organized as follows. The continuous-time MFA representation of discrete-time systems is proposed in Section 5.1. The MFA model of a continuous-time MFA model of a discrete-time controller is described in Section 5.2. Also the state-space model of the delayed duty cycle introduced by the zero-order-hold in the DPWM is provided in Section 5.2. Simulation studies demonstrating the proposed model during transient and steady-state intervals are presented in Section 5.3. Experimental validation is described in Section 5.4. A concluding summary and remarks are provided in Section 5.5.

5.1 MFA Representation of Discrete-Time System

In this section, an approach for representing discrete-time systems using continuous-time MFA models is proposed. A general discrete-time system is considered:

$$\mathbf{X}[n+1] = \mathbf{A}\mathbf{X}[n] + \mathbf{B}\mathbf{U}[n] \tag{5.1}$$

$$\mathbf{Y}[n] = \mathbf{C}\mathbf{X}[n] + \mathbf{D}\mathbf{U}[n], \tag{5.2}$$

where $\mathbf{X} \in \mathbb{R}^{n_x}$ is the state vector, $\mathbf{U} \in \mathbb{R}^{n_u}$ is the input vector, and $\mathbf{Y} \in \mathbb{R}^{n_y}$ is the output vector. The sampling rate of the discrete-time system is assumed to be an integer multiple of the switching frequency, such that the sampling period is $T_p = T/N$, where T is the switching period.

The state vector can be expressed as $\mathbf{X}[n] = [x_1[n]\ x_2[n]\ \ldots\ x_{n_x}[n]]^{\mathrm{T}}$. Each component can be approximated using a (discrete-time) average vector such that

$$x_j[n] \approx \boldsymbol{\theta}_n^{\mathrm{T}} \mathbf{x}_j[n] \tag{5.3}$$

for $j \in \{1, 2, \ldots, n_x\}$, where ϕ represents an angular offset between the switching and sampling times and $\boldsymbol{\theta}_n = \boldsymbol{\theta}(T_p(n + \phi/(2\pi)))$ (from (2.24)). It is assumed that the

average vector $\mathbf{x}_j[n]$ changes relatively slowly, and it can be written as

$$\mathbf{x}_j[n] = [x_{jf}[n]\ \mathbf{x}_{jh}^{\mathrm{T}}[n]]^{\mathrm{T}} \tag{5.4}$$

where $x_{jf}[n]$ and $\mathbf{x}_{jh}[n]$ are the fundamental average and the harmonic average vector of $\mathbf{x}_j[n]$, respectively.

If $\mathbf{X}_f[n]$ and $\mathbf{X}_h[n]$ are defined as

$$\mathbf{X}_f[n] = [x_{1f}[n]\ x_{2f}[n]\ \ \ldots\ \ x_{n_x f}[n]]^{\mathrm{T}} \tag{5.5}$$

$$\mathbf{X}_h[n] = [\mathbf{x}_{1h}^{\mathrm{T}}[n]\ \mathbf{x}_{2h}^{\mathrm{T}}[n]\ \ \ldots\ \ \mathbf{x}_{n_x h}^{\mathrm{T}}[n]]^{\mathrm{T}}, \tag{5.6}$$

then the discrete-time state vector can be approximated as

$$\mathbf{X}[n] \approx \left[\mathbf{I}_{n_x}\ \mathbf{I}_{n_x} \otimes \bar{\boldsymbol{\theta}}_n^{\mathrm{T}}\right] \begin{bmatrix} \mathbf{X}_f[n] \\ \mathbf{X}_h[n] \end{bmatrix}, \tag{5.7}$$

where $\mathbf{I}_l$ is the $l \times l$ identity matrix, $\bar{\boldsymbol{\theta}}_n$ is $\boldsymbol{\theta}_n$ with the first element removed, and $\otimes$ is the Kronecker product operator. Likewise, the the input vector and the output vector can be approximated using the average vectors such that

$$\mathbf{U}[n] \approx \left[\mathbf{I}_{n_u}\ \mathbf{I}_{n_u} \otimes \bar{\boldsymbol{\theta}}_n^{\mathrm{T}}\right] \begin{bmatrix} \mathbf{U}_f[n] \\ \mathbf{U}_h[n] \end{bmatrix} \tag{5.8}$$

$$\mathbf{Y}[n] \approx \left[\mathbf{I}_{n_y}\ \mathbf{I}_{n_y} \otimes \bar{\boldsymbol{\theta}}_n^{\mathrm{T}}\right] \begin{bmatrix} \mathbf{Y}_f[n] \\ \mathbf{Y}_h[n] \end{bmatrix}, \tag{5.9}$$

where the average vectors are again assumed to change relatively slowly.

Substitution of (5.7)–(5.9) into (5.1) and (5.2) yields a discrete-time MFA representation of the discrete-time state-space model:

$$\mathbf{X}_f[n+1] = \mathbf{A}\mathbf{X}_f[n] + \mathbf{B}\mathbf{U}_f[n] \tag{5.10}$$

$$\left(\mathbf{I}_{n_x} \otimes \bar{\boldsymbol{\theta}}_{n+1}^{\mathrm{T}}\right) \mathbf{X}_h[n+1] = \mathbf{A}\left(\mathbf{I}_{n_x} \otimes \bar{\boldsymbol{\theta}}_n^{\mathrm{T}}\right) \mathbf{X}_h[n] + \mathbf{B}\left(\mathbf{I}_{n_u} \otimes \bar{\boldsymbol{\theta}}_n^{\mathrm{T}}\right) \mathbf{U}_h[n] \tag{5.11}$$

$$\mathbf{Y}_f[n] = \mathbf{C}\mathbf{X}_f[n] + \mathbf{D}\mathbf{U}_f[n] \tag{5.12}$$

$$\left(\mathbf{I}_{n_x} \otimes \bar{\boldsymbol{\theta}}_n^{\mathrm{T}}\right) \mathbf{Y}_h[n] = \mathbf{C}\left(\mathbf{I}_{n_x} \otimes \bar{\boldsymbol{\theta}}_n^{\mathrm{T}}\right) \mathbf{X}_h[n] + \mathbf{D}\left(\mathbf{I}_{n_u} \otimes \bar{\boldsymbol{\theta}}_n^{\mathrm{T}}\right) \mathbf{U}_h[n]. \tag{5.13}$$

It is shown in Appendix C that

$$\mathbf{A}\left(\mathbf{I}_{n_x} \otimes \bar{\boldsymbol{\theta}}_n^{\mathrm{T}}\right) = \left(\mathbf{I}_{n_x} \otimes \bar{\boldsymbol{\theta}}_n^{\mathrm{T}}\right)(\mathbf{A} \otimes \mathbf{I}_{2K}) \tag{5.14}$$

$$\mathbf{B}\left(\mathbf{I}_{n_u} \otimes \bar{\boldsymbol{\theta}}_n^{\mathrm{T}}\right) = \left(\mathbf{I}_{n_x} \otimes \bar{\boldsymbol{\theta}}_n^{\mathrm{T}}\right)(\mathbf{B} \otimes \mathbf{I}_{2K}) \tag{5.15}$$

$$\mathbf{C}\left(\mathbf{I}_{n_x} \otimes \bar{\boldsymbol{\theta}}_n^{\mathrm{T}}\right) = \left(\mathbf{I}_{n_x} \otimes \bar{\boldsymbol{\theta}}_n^{\mathrm{T}}\right)(\mathbf{C} \otimes \mathbf{I}_{2K}) \tag{5.16}$$

$$\mathbf{D}\left(\mathbf{I}_{n_u} \otimes \bar{\boldsymbol{\theta}}_n^{\mathrm{T}}\right) = \left(\mathbf{I}_{n_x} \otimes \bar{\boldsymbol{\theta}}_n^{\mathrm{T}}\right)(\mathbf{D} \otimes \mathbf{I}_{2K}), \tag{5.17}$$

where K is the MFA approximation order. Substituting (5.14) and (5.15) into (5.11) gives

$$\mathbf{I}_{n_x} \otimes \bar{\boldsymbol{\theta}}_{n+1}^{\mathrm{T}} \mathbf{X}_h[n+1] = \left(\mathbf{I}_{n_x} \otimes \bar{\boldsymbol{\theta}}_n^{\mathrm{T}}\right)(\mathbf{A} \otimes \mathbf{I}_{2K})\mathbf{X}_h[n] + \left(\mathbf{I}_{n_x} \otimes \bar{\boldsymbol{\theta}}_n^{\mathrm{T}}\right)(\mathbf{B} \otimes \mathbf{I}_{2K})\mathbf{U}_h[n] \tag{5.18}$$

The relationship between $\bar{\boldsymbol{\theta}}_n$ and $\bar{\boldsymbol{\theta}}_{n+1}$ can be expressed as

$$\bar{\boldsymbol{\theta}}_n^{\mathrm{T}} = \bar{\boldsymbol{\theta}}_{n+1}^{\mathrm{T}} \mathbf{P} \tag{5.19}$$

where $\mathbf{P} \in \mathbb{R}^{2K \times 2K}$ is a block diagonal matrix with the kth 2×2 block element $\mathbf{p}_k$ given by

$$\mathbf{p}_k = \begin{bmatrix} \cos(\frac{2k\pi}{N}) & -\sin(\frac{2k\pi}{N}) \\ \sin(\frac{2k\pi}{N}) & \cos(\frac{2k\pi}{N}) \end{bmatrix} \tag{5.20}$$

for $k \in \{1, 2, \ldots, K\}$. Therefore,

$$\mathbf{I}_{n_x} \otimes \bar{\boldsymbol{\theta}}_n^{\mathrm{T}} = \mathbf{I}_{n_x} \otimes \left(\bar{\boldsymbol{\theta}}_{n+1}^{\mathrm{T}} \mathbf{P}\right) = \left(\mathbf{I}_{n_x} \otimes \bar{\boldsymbol{\theta}}_{n+1}^{\mathrm{T}}\right) \left(\mathbf{I}_{n_x} \otimes \mathbf{P}\right). \tag{5.21}$$

Substituting (5.21) into (5.18) and left multiplying by the pseudoinverse of $\mathbf{I}_{n_x} \otimes \bar{\boldsymbol{\theta}}_{n+1}^{\mathrm{T}}$ results in

$$\begin{aligned} \mathbf{X}_h[n+1] &= \left(\mathbf{I}_{n_x} \otimes \mathbf{P}\right) \left(\mathbf{A} \otimes \mathbf{I}_{2K}\right) \mathbf{X}_h[n] + \left(\mathbf{I}_{n_x} \otimes \mathbf{P}\right) \left(\mathbf{B} \otimes \mathbf{I}_{2K}\right) \mathbf{U}_h[n] \\ &= \left(\mathbf{A} \otimes \mathbf{P}\right) \mathbf{X}_h[n] + \left(\mathbf{B} \otimes \mathbf{P}\right) \mathbf{U}_h[n]. \end{aligned} \tag{5.22}$$

Likewise, substituting (5.16) and (5.17) into (5.13) and left multiplying the pseudoinverse of $\mathbf{I}_{n_x} \otimes \bar{\boldsymbol{\theta}}_n^{\mathrm{T}}$ results in

$$\mathbf{Y}_h[n] = \left(\mathbf{C} \otimes \mathbf{I}_{2K}\right) \mathbf{X}_h + \left(\mathbf{D} \otimes \mathbf{I}_{2K}\right) \mathbf{U}_h. \tag{5.23}$$

Thus, the discrete-time MFA representation of the discrete-time system in (5.1) and (5.2) is given by

$$\mathbf{X}_f[n+1] = \mathbf{A}\mathbf{X}_f[n] + \mathbf{B}\mathbf{U}_f[n] \tag{5.24}$$

$$\mathbf{X}_h[n+1] = \left(\mathbf{A} \otimes \mathbf{P}\right) \mathbf{X}_h[n] + \left(\mathbf{B} \otimes \mathbf{P}\right) \mathbf{U}_h[n] \tag{5.25}$$

$$\mathbf{Y}_f[n] = \mathbf{C}\mathbf{X}_f[n] + \mathbf{D}\mathbf{U}_f[n] \tag{5.26}$$

$$\mathbf{Y}_h[n] = \left(\mathbf{C} \otimes \mathbf{I}_{2K}\right) \mathbf{X}_h[n] + \left(\mathbf{D} \otimes \mathbf{I}_{2K}\right) \mathbf{U}_h[n]. \tag{5.27}$$

This discrete-time MFA representation represents the behavior of the discrete-time system of order n_x using a discrete-time MFA system of order $(2K+1)n_x$, which is identical to the relationship between continuous-time systems and their MFA representations.

This discrete-time MFA approach actually describe the nonlinear dynamics of the discrete-time systems but generally require long simulation run times (compared with averaged models) because the simulation time step of the discrete-time models is limited by the sampling period or the switching period. It is possible to represent the discrete-time MFA model using a number of alternative transformations (e.g., forward or backward Euler, bilinear). If the bilinear transformation is applied to the z-domain expression of the discrete-time MFA model in (5.24)–(5.27), such that

$$z \approx \frac{1 + \frac{sT_p}{2}}{1 - \frac{sT_p}{2}}, \tag{5.28}$$

then the time-domain expression of the resultant continuous-time s-domain model can be described as

$$\frac{d\mathbf{Z}_f}{dt} = (\mathbf{A} - \mathbf{I}_{n_x})\,\mathbf{X}_f + \mathbf{B}\mathbf{U}_f \tag{5.29}$$

$$\frac{d\mathbf{Z}_h}{dt} = (\mathbf{A} \otimes \mathbf{P} - \mathbf{I}_{2Kn_x})\,\mathbf{X}_h + (\mathbf{B} \otimes \mathbf{P})\,\mathbf{U}_h \tag{5.30}$$

$$\mathbf{Y}_f = \mathbf{C}\mathbf{X}_f + \mathbf{D}\mathbf{U}_f \tag{5.31}$$

$$\mathbf{Y}_h = (\mathbf{C} \otimes \mathbf{I}_{2K})\mathbf{X}_h + (\mathbf{D} \otimes \mathbf{I}_{2K})\mathbf{U}_h, \tag{5.32}$$

where $\mathbf{Z}_f$ and $\mathbf{Z}_h$ are defined in terms of $\mathbf{X}_f$ and $\mathbf{U}_f$, $\mathbf{X}_h$ and $\mathbf{U}_h$, respectively, such that

$$\mathbf{Z}_f = \frac{T_p}{2}(\mathbf{A} + \mathbf{I}_{n_x})\mathbf{X}_f + \frac{T_p}{2}\mathbf{B}\mathbf{U}_f \tag{5.33}$$

$$\mathbf{Z}_h = \frac{T_p}{2}(\mathbf{A} \otimes \mathbf{P} + \mathbf{I}_{2Kn_x})\mathbf{X}_h + \frac{T_p}{2}(\mathbf{B} \otimes \mathbf{P})\mathbf{U}_h. \tag{5.34}$$

5.2 Discrete-Time Feedback Controller

Discrete-time feedback controller has attracted increasing interest because of the ease of digital implementation. Compared with analog implementations, digital imple-

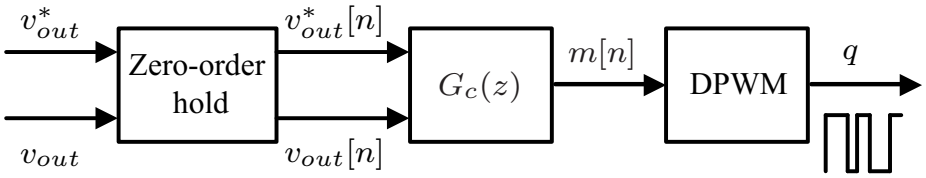

Figure 5.1: Discrete-time voltage-mode DPWM controller.

mentations have lower sensitivity to parameter variation, higher design flexibility, and better communication capability [34–39]. In this section, a discrete-time feedback controller which employs the voltage-mode control principle (e.g., [78, 79, 117]) for output voltage regulation shown in Figure 5.1 is set forth. The zero-order hold samples the output voltage v_{out} and the output voltage command v^*_{out} for discretization. The sampling rate of zero-order hold is assumed to be an integer multiple of the switching frequency, such that the sampling period is $T_p = T/N$, where T is the switching period. The discrete-time $v_{out}[n]$ and $v^*_{out}[n]$ are fed into a discrete-time compensator $G_c(z)$ for calculating the modulation signal $m[n]$. It is followed by a digital pulse-width modulator (DPWM) to produce the switching function q that corresponds to the calculated modulation signal $m[n]$.

This section is broken into two subsections covering the continuous-time MFA representation of the discrete-time compensator and the DPWM.

5.2.1 Discrete-Time Compensator

A discrete-time PI compensator, such as that depicted in Figure 5.2, is a commonly used discrete-time feedback compensator for regulating the output voltage due to its simplicity and flexibility of design (e.g., [82–84]). This compensator calculates the discrete-time modulation signal $m[n]$ using the discrete-time output voltage error as the input to the controller and a discrete-time feedforward voltage command $v^*_{out}[n]$.

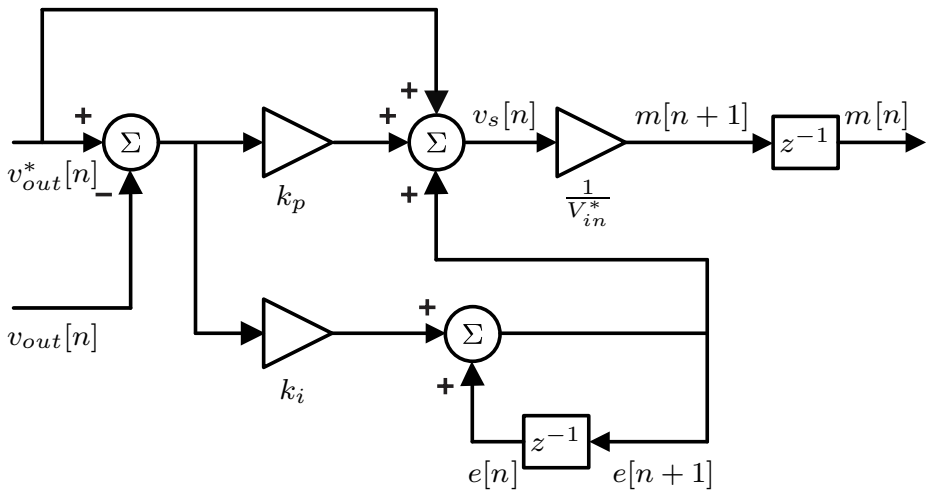

Figure 5.2: Discrete-time PI compensator.

The PI compensator can be described as

$$e[n+1] = e[n] + k_i(v^*_{out}[n] - v_{out}[n]) \tag{5.35}$$

$$v_s[n] = e[n+1] + v^*_{out}[n] + k_p(v^*_{out}[n] - v_{out}[n]) \tag{5.36}$$

$$m[n+1] = \frac{1}{V^*_{in}} v_s[n] \tag{5.37}$$

where k_p and k_i are control parameters and V^*_{in} is the nominal value of the input voltage V_{in}.

If each signal is approximated by a Kth-order (discrete-time) Fourier series, then applying the proposed continuous-time MFA representation of the discrete-time system described in (5.29)–(5.32) yields the following

$$\frac{dw_f}{dt} = k_i(v^*_{outf} - v_{outf}) \tag{5.38}$$

$$\frac{d\mathbf{w}_h}{dt} = (\mathbf{P} - \mathbf{I}_{2K})\mathbf{e}_h + k_i\mathbf{P}(\mathbf{v}^*_{outh} - \mathbf{v}_{outh}) \tag{5.39}$$

$$\mathbf{v}_s = \mathbf{e} + \mathbf{v}^*_{out} + (k_p + k_i)(\mathbf{v}^*_{out} - \mathbf{v}_{out}) \tag{5.40}$$

$$\frac{dr_f}{dt} = -m_f + \frac{1}{V^*_{in}} v_{sf} \tag{5.41}$$

$$\frac{d\mathbf{r}_h}{dt} = -\mathbf{I}_{2K}\mathbf{m}_h + \frac{1}{V^*_{in}}\mathbf{P}\mathbf{v}_{sh}. \tag{5.42}$$

where the subscript f and h represent the fundamental average and the harmonic average vector, respectively, w_f, $\mathbf{w}_h$, r_f and $\mathbf{r}_h$ are defined as

$$w_f = T_p e_f + \frac{T_p}{2} k_i (v^*_{outf} - v_{outf}) \tag{5.43}$$

$$\mathbf{w}_h = \frac{T_p}{2}(\mathbf{P} + \mathbf{I}_{2K})\mathbf{e}_h + \frac{T_p}{2} k_i \mathbf{P}(\mathbf{v}^*_{outh} - \mathbf{v}_{outh}) \tag{5.44}$$

$$r_f = \frac{T_p}{2} m_f + \frac{T_p}{2} \frac{1}{V^*_{in}} v_{sf} \tag{5.45}$$

$$\mathbf{r}_h = \frac{T_p}{2} \mathbf{m}_h + \frac{T_p}{2} \frac{1}{V^*_{in}} \mathbf{P}\mathbf{v}_{sh}. \tag{5.46}$$

5.2.2 DPWM

A DPWM is to produce the switching function q that corresponds to the calculated discrete-time modulation signal $m[n]$. Herein, uniformly sampled DPWM is considered. Uniformly sampled DPWM is similar to uniformly sampled PWM shown in Section 2.4.2. In this setting, the discrete-time modulation signal is regularly sampled through a zero-order hold at the beginning of the switching period before being compared with the carrier c and stored in a shadow register for the use during that period (e.g., [85]). An example showing the switching function produced by the uniformly sampled DPWM with trailing edge modulation is illustrated in Figure 5.3. It can be observed that the switching instant does not depend on the ripple of modulation signal explicitly; rather, it depends on the value of the modulation signal at the beginning of the switching cycle.

If the modulation signal is approximated by a Kth-order (discrete-time) Fourier series, then the value of $m[n]$ (the value that is used by the DPWM implementation) is

$$D[n] \approx m_0 + \sum_{k=1}^{K} m_{kc}. \tag{5.47}$$

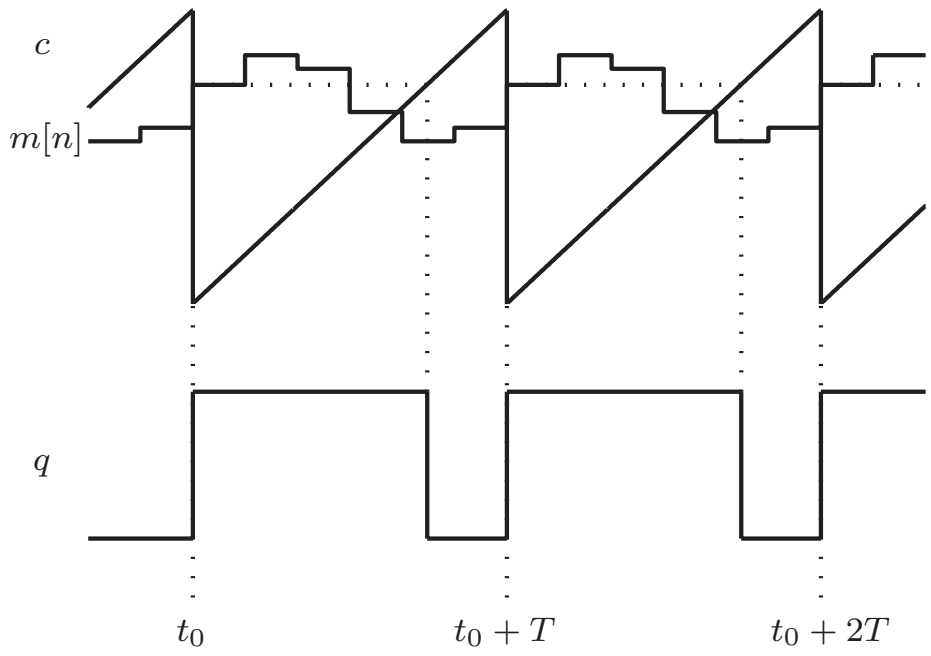

Figure 5.3: Switching function produced by uniformly sampled DPWM ($N = 6$).

It is possible to represent the discrete-time duty cycle $D[n]$ with the continuous-time representation $D(t)$. It is also noted that the zero-order hold introduces an effective average delay of $T/2$ on the continuous-time duty cycle $D(t)$ [118]. The continuous model of this delay can be approximated by applying the following first-order approximation:

$$e^{-\frac{T}{2}s} \approx \frac{1}{1+\frac{T}{2}s}. \tag{5.48}$$

The resultant state-space equation of the delayed duty cycle $\tilde{D}$ is given by

$$\frac{d\tilde{D}}{dt} \approx -\frac{2}{T}\tilde{D} + \frac{2}{T}D. \tag{5.49}$$

Application of (2.38)–(2.40) yields the average vector $\mathbf{q}$ which in turn drives the MFA model of the buck converter.

Table 5.1: Parameters of Dc/Dc Buck Converter for Simulation Studies

V_{in}	250 V	L	0.6818 mH	R_1	11.2565 Ω
V_{in}^*	250 V	R_L	422.3 mΩ	R_2	8.4129 Ω
v_{out}^*	120 V	C	150.34 µF	k_p	0.2
f	5 kHz	R_C	75.2 mΩ	k_i	0.05

5.3 Simulation Studies

Several simulation studies are described to demonstrate the proposed continuous-time MFA representation of discrete-time systems. In particular, the buck converter shown in Figure 3.1 with the discrete-time feedback controller shown in Figure 5.1 and the parameters given in Table 5.1 is studied. In the discrete-time feedback controller, the sampling rate is given by the switching frequency and the sampling instants are synchronized with the uniformly sampled DPWM. A detailed model, a traditional MFA model, an ISMFA model using the method proposed in Chapter 3 and an MFA model using the proposed MFA representation of the discrete-time feedback controller (DMFA) are constructed for simulation studies. Each approach involves the representation of the discrete-time compensator and the DPWM. In the DMFA model, the proposed method of continuous-time MFA representation of discrete-time systems described in Section 5.1 is applied to represent the discrete-time compensator. In the MFA and ISMFA models, the discrete-time compensator described by (5.35)–(5.37) is directly approximated by the same transformation as in DMFA model (i.e., bilinear transformation), such that

$$\frac{d\bar{w}}{dt} = k_i(v_{out}^* - v_{out}) \tag{5.50}$$

$$v_s = e + v_{out}^* + (k_p + k_i)(v_{out}^* - v_{out}) \tag{5.51}$$

$$\frac{d\bar{r}}{dt} = -m + \frac{1}{V_{in}^*}v_s, \tag{5.52}$$

where $\bar{w}$ and $\bar{r}$ are defined as

$$\bar{w} = T_p e + \frac{T_p}{2} k_i (v^*_{out} - v_{out}) \tag{5.53}$$

$$\bar{r} = \frac{T_p}{2} m + \frac{T_p}{2} \frac{1}{V^*_{in}} v_s. \tag{5.54}$$

This continuous-time approximation of the discrete-time compensator is then approximated by MFA representation. The uniformly sampled DPWM in the MFA model is treated as naturally sampled PWM and the switching time at which the modulation signal crosses the sawtooth carrier in each switching cycle is solved by one iteration of Newton's method described in [24]. ISMFA and DMFA models does not involve the algebraic complexity associated with uniformly sampled DPWM. In this setting, the value of the modulation signal at the beginning of the switching period (the value that is used by the DPWM implementation) is approximated by (5.47). Also, the delay introduced by the zero-order hold in this setting is represented by (5.49) in these two models.

5.3.1 Comparison of Steady-State Behavior of MFA, ISMFA and DMFA Models

To demonstrate the accuracy and efficiency of the proposed DMFA model in portraying the steady-state behavior of the system, simulations of output voltage and inductor current for a detailed model, an (first-order) MFA model, an (first-order) ISMFA model and a (first-order) DMFA model with a constant load R_1 are shown in Figure 5.4. To avoid discontinuous mode in the start transient, the reference voltage is slowly ramped to the desired value in $[0, 0.05]$ s. The simulation for each model is carried out on a personal computer (Intel(R) Core(TM) i7-3770 CPU @ 3.40 GHz, 8.00 GB RAM, 64-bit Operating System) for 0.2 s. Table 5.2 compares the dc value and rms error of inductor current and output voltage and simulation runtimes in

Table 5.2: Comparison of dc value and rms error of inductor current and output voltage and simulation runtimes for detailed (DET), (first-order) MFA, (first-order) ISMFA and (first-order) DMFA models

Models	Inductor current (A)		Output voltage (V)		Runtimes (s)
	dc	rms error	dc	rms error	
DET	10.73	0	120.75	0	2.28
MFA	10.66	5.1384	120.00	0.7554	0.23
ISMFA	10.66	5.1384	120.00	0.7554	0.86
DMFA	10.72	5.1144	120.62	0.1439	0.20

each model. The rms error of inductor current or output voltage in each model is calculated based on the following formula

$$f_{\text{rms}} = \sqrt{\frac{1}{t_2 - t_1} \int_{t_1}^{t_2} (f(t) - f_{\text{det}})^2 dt}. \tag{5.55}$$

Herein, the rms error is calculated over one switching period such that $t_2 - t_1 = T$ and f_{det} is given by the inductor current or output voltage in detailed model. It can be seen that the (first-order) MFA, ISMFA and DMFA models accurately predict the inductor current with respect to the detailed model. It can be observed that close agreement exists between the output voltage as predicted by the DMFA and detailed models. However, the MFA and ISMFA models are shown to be not capable of predicting the correct steady-state output voltage. It can be observed that the detailed model takes 10 times more simulation runtimes than the MFA and DMFA models and 2 times more simulation runtimes than the ISMFA model.

5.3.2 Comparison of Transient Behavior of MFA and DMFA Models

To demonstrate the proposed DMFA model in portraying the transient behavior of the system, a step load change from R_1 to R_2 is applied and the comparison of

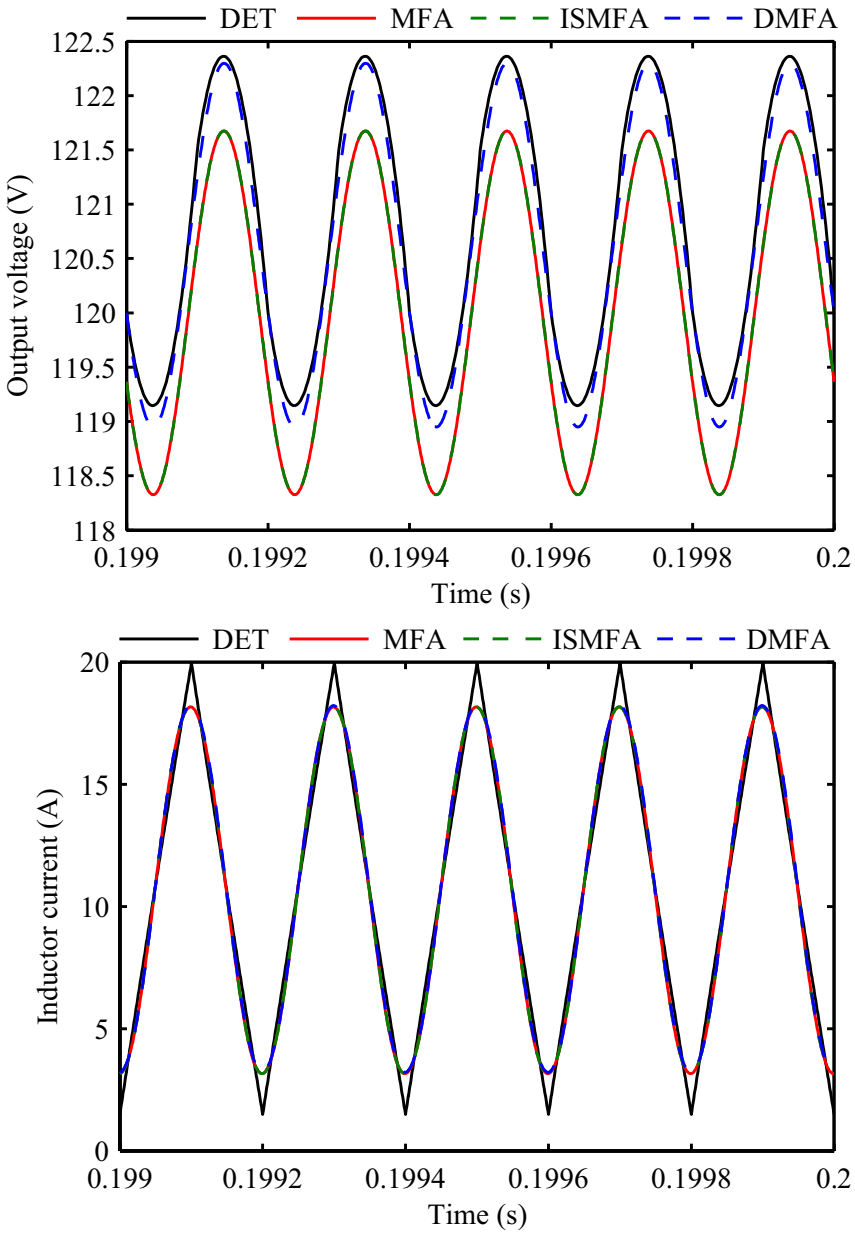

Figure 5.4: Simulation results of steady-state inductor current and output voltage for detailed (DET), (first-order) MFA, ISMFA and DMFA models.

output voltage and inductor current for a detailed model, an (first-order) MFA, an (first-order) ISMFA model and a (first-order) DMFA model is shown in Figure 5.5. It can be seen that the (first-order) MFA, ISMFA and DMFA models accurately predict the inductor current with respect to the detailed model. It can be observed that the output voltage predicted by the DMFA model matches the detailed model very

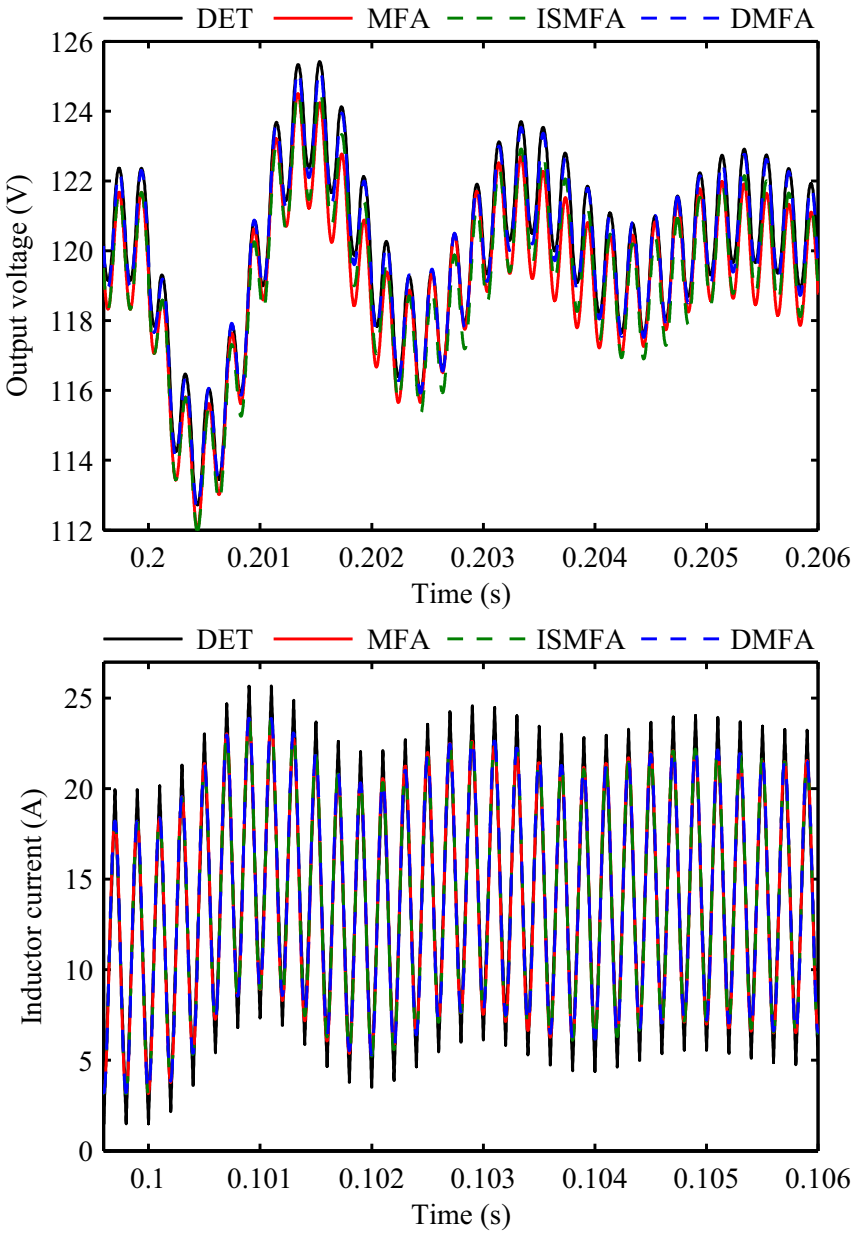

Figure 5.5: Simulation results of transient inductor current and output voltage for detailed (DET), (first-order) MFA, ISMFA and DMFA models.

well, while the MFA and ISMFA models show a deviation to the detailed model. To further demonstrate the proposed DMFA model, the rms error of inductor current and output voltage in the transient interval from 0.2 s to 0.206 s is calculated based on the formula in (5.55) and shown in Table 5.3. It can be seen that the DMFA model accurately predict the rms error in the transient with respect to the detailed model.

Table 5.3: Comparison of rms error of inductor current and output voltage for detailed (DET), (first-order) MFA, ISMFA and (first-order) DMFA models

Models	Inductor current (A) rms error	Output voltage (V) rms error
DET	0	0
MFA	8.5606	0.8423
ISMFA	8.5606	0.7390
DMFA	8.5359	0.1551

Table 5.4: Parameters of Dc/Dc Buck Converter for Experimental Validation

V_{in}	250 V	L	1.5 mH	R_1	11.2565 Ω
V_{in}^*	250 V	R_L	422.3 mΩ	R_2	8.4129 Ω
v_{out}^*	150 V	C	150.34 µF	k_p	0.2
f	5 kHz	R_C	75.2 mΩ	k_i	0.05

5.4 Experimental Validation

In order to validate the proposed DMFA model, the buck converter and the discrete-time feedback controller with the parameters given in Table 5.4 are studied experimentally. The digital control is implemented in a TMS320F28335 microcontroller. The discrete-time PI control is implemented by sampling the output voltage at the sampling rate equal to the switching frequency. The sampling instants are synchronized with the uniformly sampled DPWM. The uniformly sampled DPWM is implemented using a shadow register to implement the zero-order hold depicted in Figure 5.1. A step load resistance change from R_1 to R_2 is applied, and the inductor current and output voltage are measured experimentally and compared with the simulation output of a detailed model. This comparison is shown in Figure 5.6. It can be seen that the inductor current and the output voltage predicted by the DMFA model match the experimentally measured inductor current and output voltage very well.

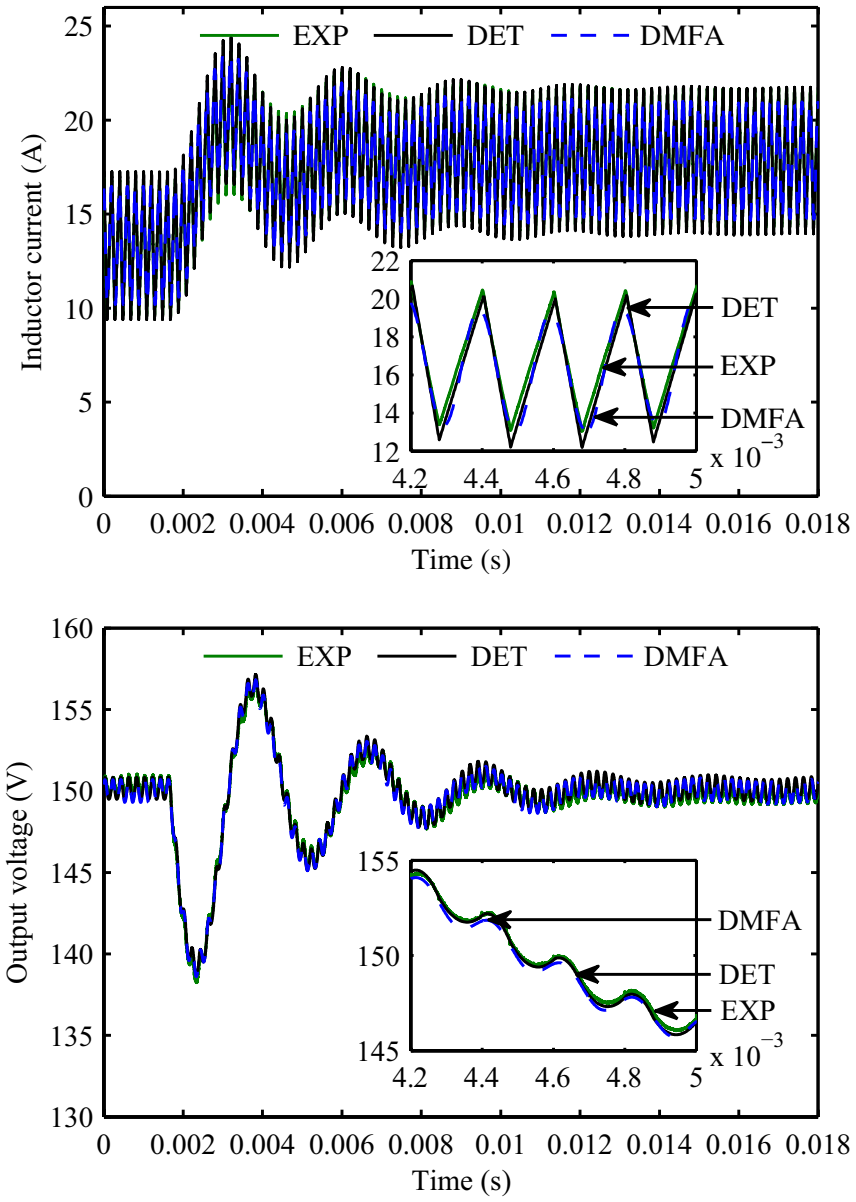

Figure 5.6: Step load change experimental (EXP) and simulation results for detailed (DET) and (first-order) DMFA models. The experimental measurements are low-pass filtered with a time constant of 2 μs to remove measurement noise.

5.5 Conclusion

The continuous-time MFA representation of discrete-time systems is proposed. Simulation results of both transient and steady-state responses show that the proposed model provides an accurate prediction of system behavior. The proposed model is

validated experimentally by consideration of step load changes with a digitally controlled PWM buck converter. It is shown that the proposed method is capable of predicting the transient and steady-state behavior predicted by the detailed model and measured experimentally.

CHAPTER 6

CONCLUSIONS AND FUTURE WORK

In this chapter, a concluding summary of this work is presented and areas of future work are suggested.

In this work, an MFA method is explored for the analysis and design of power electronic systems. This technique is capable of portraying the average behavior as well as the ripple behavior of power electronic systems. In this work, the MFA method is extended to represent uniformly sampled PWM converters. The proposed method also addresses a numerical stability issue that is observed in the traditional MFA representations. Simulation results of both transient and steady-state responses show that the proposed method provides an accurate prediction of system behavior and its small-signal behavior. The proposed method is validated experimentally by consideration of step load changes with a uniformly sampled dc-dc PWM buck converter. It is shown that the proposed method is capable of predicting the transient and steady-state behavior predicted by the detailed model and measured experimentally.

Then, a reduced-order MFA method is proposed to perform ROA estimations using Lyapunov techniques. The proposed reduced-order MFA method is capable of representing the effects of switching ripple on the behavior of the system and is, therefore, more capable of predicting the influence of the switching ripple on the stability of the system. The proposed method in performing ROA estimations using Lyapunov techniques is demonstrated in simulation studies and validated experimentally using a naturally sampled PWM converter with constant power load. The use of the proposed method for ROA estimation is found be be more accurate than the use of SSA models for power electronic converters in which the switching ripple is not negligible.

Finally, a method of continuous-time MFA representation of discrete-time systems is proposed. The proposed method relies on the discrete-time MFA representation

of the discrete-time systems and approximation transformations from discrete-time models to continuous-time models. The proposed method is demonstrated in simulation studies and validated experimentally using a digitally controlled PWM converter. It is shown that the proposed method is capable of predicting the transient and steady-state behavior predicted by the detailed model.

It is noted that the studies considered in this work are for buck converters and that the results could be applied equally to other power electronic systems or even to other systems that exhibit periodic oscillation in steady state. The extension of the MFA method proposed in this work makes the modeling and simulation of complicated power electronic systems highly accurate (compared to SSA models) while highly numerically efficient (compared to detailed models). It helps designers gain better understanding of circuit operation, select appropriate circuit component types and values, choose control topologies, and estimate circuit performance. Further, a reduced-order MFA method, along with a genetic algorithm based procedure, is proposed in this work to perform ROA estimations of power electronic systems. Such a procedure provides the ROA estimates with sufficient accuracy and efficiency, rather than working directly with detailed models. It helps design power electronic systems with high robustness and reliability, where the circuit performance will meet specifications even with anticipated perturbations in operation conditions.

There are several topics in which this work may be extended. These topics are described in more detail below.

The MFA method has been studied for PWM control (e.g, naturally sampled PWM and uniformly sampled PWM), but has not been extended to hysteresis current control, peak current control, or other control methods. In hysteresis control, the switching of the power electronic systems does not always have constant frequency. Therefore, the state variables (e.g, inductor current and capacitor voltage) in the systems are not quasiperiodic signals and cannot be directly approximated by MFA

representation. To extend the applicability of the MFA method to hysteresis control, the representation of state variables and time-varying switching frequency should be studied carefully. Future work would focus on the construction of MFA representation which is suitable for hysteresis controlled power electronic systems.

The MFA method has been applied to model three-phase inverters [61]. Therein, the MFA representation for the time-varying fundamental components of the three-phase state variables and the duty cycle is constructed. The fundamental components are changing relatively slowly with respect to the small-ripple switching components and have relatively large magnitude. Therein,it is assumed that the small-ripple switching components in the MFA model are negligible. However, the small-ripple switching components might be significant with lower switching frequency. This motivates one to seek complete MFA representation for the state variables in inverters. In Section 2.2, a quasiperiodic signal $x(t)$ can be approximated by a partial Fourier series described in (2.21) and (2.22). This representation might be extended by considering the fundamental components and switching (i.e., small-ripple) components such that

$$\begin{aligned} x(t) \approx x_0(t) &+ \sum_{n=1}^{N} (\bar{x}_{nc}(t)\cos(n\bar{\omega}t) + \bar{x}_{ns}(t)\sin(n\bar{\omega}t)) \\ &+ \sum_{k=1}^{K} (\hat{x}_{kc}(t)\cos(k\hat{\omega}t) + \hat{x}_{ks}(t)\sin(k\hat{\omega}t)) \end{aligned} \tag{6.1}$$

where $x_0(t)$, $\bar{x}_{nc}(t)$, $\bar{x}_{ns}(t)$, $\hat{x}_{kc}(t)$ and $\hat{x}_{ks}(t)$ are real-valued TFS coefficients referred to as the index-0, index-nc, index-ns, index-kc and index-ks averages, respectively, $\bar{\omega}$ and $\hat{\omega}$ are fundamental angular frequency and switching angular frequency, respectively. This series is a Nth-Kth-order approximation of $x(t)$. An average vector of length $(2(N+K)+1)$ can be constructed from the TFS coefficients in (6.1):

$$\mathbf{x} = [x_0 \ \bar{x}_{1c} \ \bar{x}_{1s} \ \ldots \ \bar{x}_{Nc} \ \bar{x}_{Ns} \ \hat{x}_{1c} \ \hat{x}_{1s} \ \ldots \ \hat{x}_{Kc} \ \hat{x}_{Ks}]^{\mathrm{T}}. \tag{6.2}$$

With this vector, (6.1) can be reconstructed as $x(t) \approx \mathbf{C}(t)\mathbf{x}$, where $\mathbf{C}(t)$ is defined as

$$\mathbf{C}(t) = [1 \ \cos(\bar{\omega}t) \ \sin(\bar{\omega}t) \ \ldots \ \cos(N\bar{\omega}t) \ \sin(N\bar{\omega}t) \\ \cos(\hat{\omega}t) \ \sin(\hat{\omega}t) \ \ldots \ \cos(K\hat{\omega}t) \ \sin(K\hat{\omega}t)]. \quad (6.3)$$

This complete MFA representation carefully describes the fundamental averages and the switching averages, and might be suitable for modeling three-phase inverters. However, the MFA representation for the feedback controllers in three-phase inverters remains complicated. Future work would focus on using this complete MFA method to model the three-phase inverters.

It has been shown in Chapter 4 that the proposed RMFA model is capable of predicting the effects of switching ripple on the behavior of the power electronic systems, and is more capable of predicting the influence of the switching ripple on the stability of the system than the SSA model. The full-order MFA model is found to be more accurate than the RMFA model in predicting the ripple behavior of the power electronic systems. Such a model allows the effects of switching harmonics to be included in the model with increasing the model order, permitting the effects of switching ripple to be considered in stability analysis. However, the use of MFA models for ROA estimation is found to be less accurate than the use of proposed RMFA models. This extraordinary phenomenon might be attributed to the method which is used herein to select the Lyaponuv functions for the full-order MFA models. Future work would focus on the construction of Lyapunov functions which are suitable for ROA estimation using full-order MFA models.

Appendix A

STABILITY ANALYSIS OF MFA MODEL

The MFA model of the buck converter given in Subsection 3.4.2 is linearized about the equilibrium point. The Jacobian matrix is given by

$$\mathbf{J} = \begin{bmatrix} -5.80\times10^{1} & -2.31\times10^{0} & 0 & -6.99\times10^{2} & -4.62\times10^{1} & 0 & 6.58\times10^{2} & 6.58\times10^{2} & 0 \\ 3.68\times10^{0} & -5.19\times10^{1} & -6.28\times10^{4} & 7.35\times10^{1} & -5.79\times10^{2} & 0 & -1.05\times10^{3} & -1.05\times10^{3} & 0 \\ 2.80\times10^{0} & 6.28\times10^{4} & -5.56\times10^{1} & 5.59\times10^{1} & 5.59\times10^{1} & -6.52\times10^{2} & -7.97\times10^{2} & -7.97\times10^{2} & 0 \\ 5.94\times10^{3} & 0 & 0 & -9.90\times10^{2} & 0 & 0 & 0 & 0 & 0 \\ 0 & 5.94\times10^{3} & 0 & 0 & -9.90\times10^{2} & -6.28\times10^{4} & 0 & 0 & 0 \\ 0 & 0 & 5.94\times10^{3} & 0 & -6.28\times10^{4} & -9.90\times10^{2} & 0 & 0 & 0 \\ -3.51\times10^{0} & 0 & 0 & -7.02\times10^{1} & 0 & 0 & 0 & 0 & 0 \\ 0 & -3.51\times10^{0} & 0 & 0 & -7.02\times10^{1} & 0 & 0 & 0 & -6.28\times10^{4} \\ 0 & 0 & -3.51\times10^{0} & 0 & 0 & -7.02\times10^{1} & 0 & 6.28\times10^{4} & 0 \end{bmatrix} \tag{A.1}$$

The eigenvalues of the Jacobian matrix are

$$\lambda_1 = \left(-6.6754 \times 10^{1}\right) \text{ rad/s} \tag{A.2}$$

$$\lambda_{2,3} = \left(-4.9048 \times 10^{2} \pm j1.9755 \times 10^{3}\right) \text{ rad/s} \tag{A.3}$$

$$\lambda_{4,5} = \left(-5.1266 \times 10^{2} \pm j6.4672 \times 10^{4}\right) \text{ rad/s} \tag{A.4}$$

$$\lambda_{6,7} = \left(-5.8792 \times 10^{2} \pm j6.0947 \times 10^{4}\right) \text{ rad/s} \tag{A.5}$$

$$\lambda_{8,9} = \left(5.7007 \times 10^{1} \pm j6.2878 \times 10^{4}\right) \text{ rad/s} \tag{A.6}$$

Appendix B

STABILITY ANALYSIS OF ISMFA MODEL

The ISMFA model of the buck converter given in Section 3.4.2 is linearized about the equilibrium point. The constant matrices in the time-varying Jacobian matrix in (3.34) are given by

$$\mathbf{A}_0 = \begin{bmatrix} -5.8\times10^{1} & -2.3\times10^{0} & 0 & -7.0\times10^{2} & -4.6\times10^{1} & 0 & 6.6\times10^{2} & 6.6\times10^{2} & 0 \\ -1.9\times10^{1} & -5.0\times10^{5} & -6.2\times10^{4} & -3.7\times10^{2} & -1.0\times10^{3} & 5.2\times10^{3} & 5.3\times10^{3} & 5.3\times10^{3} & 0 \\ 3.2\times10^{1} & 6.2\times10^{4} & -5.0\times10^{5} & 6.4\times10^{2} & -4.6\times10^{3} & -6.5\times10^{2} & -9.1\times10^{3} & -9.1\times10^{3} & 0 \\ 5.9\times10^{3} & 0 & 0 & -9.9\times10^{2} & 0 & 0 & 0 & 0 & 0 \\ 0 & 5.9\times10^{3} & -4.7\times10^{4} & 0 & -5.0\times10^{5} & -5.5\times10^{4} & 0 & 0 & 0 \\ 0 & 4.7\times10^{4} & 5.9\times10^{3} & 0 & 5.5\times10^{4} & -5.0\times10^{5} & 0 & 0 & 0 \\ -3.5\times10^{0} & 0 & 0 & -7.0\times10^{1} & 0 & 0 & 0 & 0 & 0 \\ 0 & -3.5\times10^{0} & 2.8\times10^{1} & 0 & -7.0\times10^{1} & 5.6\times10^{2} & 0 & -5.0\times10^{5} & -6.3\times10^{4} \\ 0 & -2.8\times10^{1} & -3.5\times10^{0} & 0 & -5.6\times10^{2} & -7.0\times10^{1} & 0 & 6.3\times10^{4} & -5.0\times10^{5} \end{bmatrix} \tag{B.1}$$

$$\mathbf{A}_1 = \begin{bmatrix} 2.2\times10^{1} & 5.0\times10^{5} & -4.4\times10^{2} & 4.5\times10^{2} & 4.5\times10^{2} & -5.2\times10^{3} & -6.3\times10^{3} & -6.3\times10^{3} & 0 \\ 0 & 0 & 0 & 0 & 0 & 0 & 0 & 0 & 0 \\ 0 & 0 & 0 & 0 & 0 & 0 & 0 & 0 & 0 \\ 0 & 0 & 4.7\times10^{4} & 0 & 5.0\times10^{5} & -7.9\times10^{3} & 0 & 0 & 0 \\ 0 & 0 & 0 & 0 & 0 & 0 & 0 & 0 & 0 \\ 0 & 0 & 0 & 0 & 0 & 0 & 0 & 0 & 0 \\ 0 & 0 & -2.8\times10^{1} & 0 & 0 & -5.6\times10^{2} & 0 & 5.0\times10^{5} & 0 \\ 0 & 0 & 0 & 0 & 0 & 0 & 0 & 0 & 0 \\ 0 & 0 & 0 & 0 & 0 & 0 & 0 & 0 & 0 \end{bmatrix} \tag{B.2}$$

$$\mathbf{A}_2 = \begin{bmatrix} -2.9\times10^{1} & 4.1\times10^{2} & 5.0\times10^{5} & -5.9\times10^{2} & 4.6\times10^{3} & 0 & 8.3\times10^{3} & 8.3\times10^{3} & 0 \\ 0 & 0 & 0 & 0 & 0 & 0 & 0 & 0 & 0 \\ 0 & 0 & 0 & 0 & 0 & 0 & 0 & 0 & 0 \\ 0 & -4.7\times10^{4} & 0 & 0 & 7.9\times10^{3} & 5.0\times10^{5} & 0 & 0 & 0 \\ 0 & 0 & 0 & 0 & 0 & 0 & 0 & 0 & 0 \\ 0 & 0 & 0 & 0 & 0 & 0 & 0 & 0 & 0 \\ 0 & 2.8\times10^{1} & 0 & 0 & 5.6\times10^{2} & 0 & 0 & 0 & 5.0\times10^{5} \\ 0 & 0 & 0 & 0 & 0 & 0 & 0 & 0 & 0 \\ 0 & 0 & 0 & 0 & 0 & 0 & 0 & 0 & 0 \end{bmatrix} \tag{B.3}$$

A symmetric, positive definite matrix $\mathbf{P}$ which yields (3.37) is found by solving a linear matrix inequality problem. One solution is

$$\mathbf{P} = \begin{bmatrix} 3.9\times10^{-1} & 1.2\times10^{-2} & -1.6\times10^{-2} & -3.9\times10^{-2} & 1.9\times10^{-3} & 3.7\times10^{-4} & -2.8\times10^{-2} & -2.5\times10^{-3} & 4.8\times10^{-3} \\ 1.2\times10^{-2} & 2.4\times10^{2} & 6.9\times10^{-1} & 2.1\times10^{-1} & -8.2\times10^{0} & 7.2\times10^{0} & -3.0\times10^{0} & -1.2\times10^{1} & 4.3\times10^{-1} \\ -1.6\times10^{-2} & 6.9\times10^{-1} & 2.4\times10^{2} & -2.8\times10^{-1} & -6.7\times10^{0} & -8.4\times10^{0} & 4.1\times10^{0} & -1.8\times10^{-1} & -1.2\times10^{1} \\ -3.9\times10^{-2} & 2.1\times10^{-1} & -2.8\times10^{-1} & 4.9\times10^{-2} & 1.8\times10^{-2} & 2.9\times10^{-2} & -4.6\times10^{-2} & -1.1\times10^{-2} & 1.3\times10^{-2} \\ 1.9\times10^{-3} & -8.2\times10^{0} & -6.7\times10^{0} & 1.8\times10^{-2} & 1.6\times10^{2} & -1.2\times10^{-1} & -2.6\times10^{-1} & -1.2\times10^{1} & 2.4\times10^{-1} \\ 3.7\times10^{-4} & 7.2\times10^{0} & -8.4\times10^{0} & 2.9\times10^{-2} & -1.2\times10^{-1} & 1.6\times10^{2} & -4.2\times10^{-1} & 3.3\times10^{-1} & -1.2\times10^{1} \\ -2.8\times10^{-2} & -3.0\times10^{0} & 4.1\times10^{0} & -4.6\times10^{-2} & -2.6\times10^{-1} & -4.2\times10^{-1} & 1.7\times10^{-1} & 1.7\times10^{-1} & -1.9\times10^{-1} \\ -2.5\times10^{-3} & -1.2\times10^{1} & -1.8\times10^{-1} & -1.1\times10^{-2} & -1.2\times10^{1} & 3.3\times10^{-1} & 1.7\times10^{-1} & 1.9\times10^{2} & 1.8\times10^{0} \\ 4.8\times10^{-3} & 4.3\times10^{-1} & -1.2\times10^{1} & 1.3\times10^{-2} & 2.4\times10^{-1} & -1.2\times10^{1} & -1.9\times10^{-1} & 1.8\times10^{0} & 1.9\times10^{2} \end{bmatrix} \tag{B.4}$$

Appendix C

PROOF OF MIXED-KRONECKER-PRODUCT PROPERTY

The purpose of this appendix is to prove the mixed-Kronecker-product property given by

$$\mathbf{X}(\mathbf{I}_j \otimes \mathbf{Y}) = (\mathbf{I}_i \otimes \mathbf{Y})(\mathbf{X} \otimes \mathbf{I}_k) \tag{C.1}$$

where $\mathbf{X} \in \mathbb{R}^{i \times j}$, $\mathbf{Y} \in \mathbb{R}^{1 \times k}$ and $\mathbf{I}_n$ is the $n \times n$ identity matrix.

It has been stated in [119] that

$$\left(\mathbf{I}_j \otimes \mathbf{Y}^{\mathrm{T}}\right) \mathrm{vec}(\mathbf{X}_l) = \mathrm{vec}\left(\mathbf{Y}^{\mathrm{T}} \mathbf{X}_l \mathbf{I}_j\right) = \mathrm{vec}\left(\mathbf{Y}^{\mathrm{T}} \mathbf{X}_l\right) \tag{C.2}$$

where $\mathbf{X}_l \in \mathbb{R}^{1 \times j}$ is the lth row in $\mathbf{X}$ for $l \in [1, i]$ and $\mathrm{vec}(\bullet)$ denotes the vectorization of $\bullet$ formed by stacking the columns of $\bullet$ into a single column vector. The vectorization of $\mathbf{X}_l$ can be expressed as

$$\mathrm{vec}(\mathbf{X}_l) = \mathbf{X}_l^{\mathrm{T}}. \tag{C.3}$$

Substituting (C.3) into (C.2) and taking the transpose results in

$$\mathbf{X}_l(\mathbf{I}_j \otimes \mathbf{Y}) = \left(\mathrm{vec}\left(\mathbf{Y}^{\mathrm{T}} \mathbf{X}_l\right)\right)^{\mathrm{T}}. \tag{C.4}$$

It can be shown that

$$\begin{aligned} \left(\mathrm{vec}\left(\mathbf{Y}^{\mathrm{T}} \mathbf{X}_l\right)\right)^{\mathrm{T}} &= \left[(\mathbf{Y}^{\mathrm{T}} x_{l1})^{\mathrm{T}} \ (\mathbf{Y}^{\mathrm{T}} x_{l2})^{\mathrm{T}} \ \ldots \ (\mathbf{Y}^{\mathrm{T}} x_{lj})^{\mathrm{T}}\right] \\ &= [x_{l1}\mathbf{Y} \ x_{l2}\mathbf{Y} \ \ldots \ x_{lj}\mathbf{Y}] \\ &= \mathbf{X}_l \otimes \mathbf{Y} \end{aligned} \tag{C.5}$$

where x_{lm} is the mth element in $\mathbf{X}_l$ for $m \in [1, j]$. Substituting (C.5) into (C.4) results in

$$\mathbf{X}_l(\mathbf{I}_j \otimes \mathbf{Y}) = \mathbf{X}_l \otimes \mathbf{Y}. \tag{C.6}$$

Because $\mathbf{X}_l \in \mathbb{R}^{1\times j}$ is the lth row in $\mathbf{X}$ for $l \in [1, i]$, it can be shown that

$$\mathbf{X}(\mathbf{I}_j \otimes \mathbf{Y}) = \mathbf{X} \otimes \mathbf{Y}. \tag{C.7}$$

Applying the property of Kronecker product, the term $\mathbf{X} \otimes \mathbf{Y}$ in the above equation can be expressed as

$$\mathbf{X} \otimes \mathbf{Y} = (\mathbf{I}_i\mathbf{X}) \otimes (\mathbf{Y}\mathbf{I}_k) = (\mathbf{I}_i \otimes \mathbf{Y})(\mathbf{X} \otimes \mathbf{I}_k). \tag{C.8}$$

Substituting (C.8) into (C.7) results in

$$\mathbf{X}(\mathbf{I}_j \otimes \mathbf{Y}) = (\mathbf{I}_i \otimes \mathbf{Y})(\mathbf{X} \otimes \mathbf{I}_k). \tag{C.9}$$

Appendix D

HARDWARE PROTOTYPE

D.1 Prototype of Dc-Dc Converter

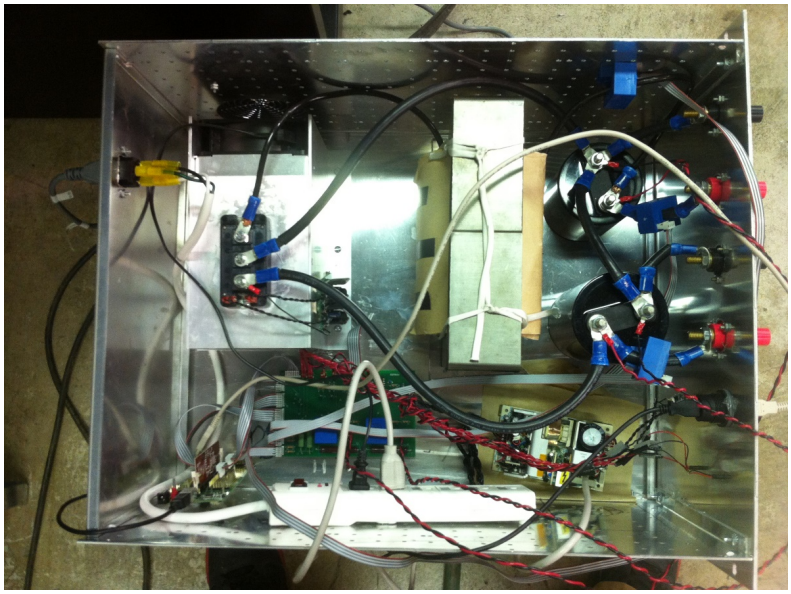

Figure D.1: Overall prototype.

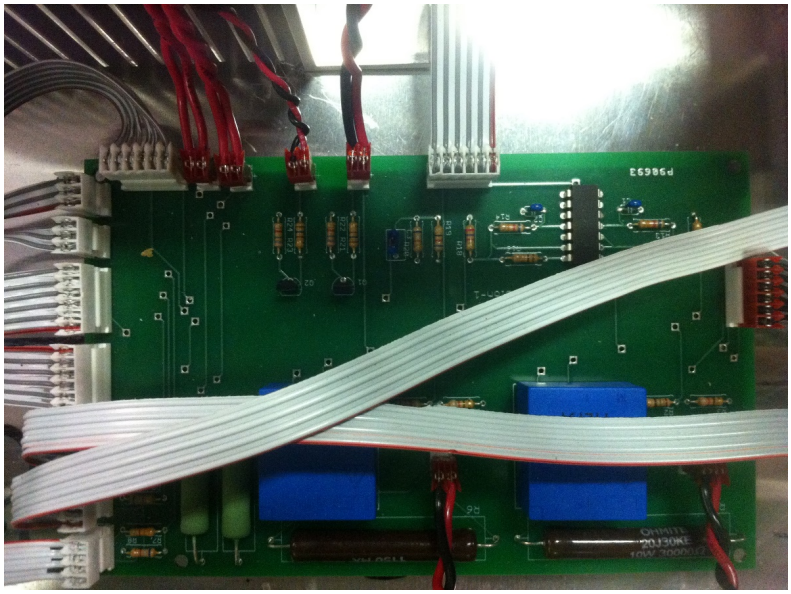

Figure D.2: PCB board.

The overall hardware prototype of the bidirectional dc-dc converter is shown Figure D.1. The capacitance ratings on the high side capacitor and the low side capacitor are 470 µF and 167 µF, respectively. The inductor is constructed with two magnetic E-cores and copper film. The inductance at 10 kHz is measured as 1.5 mH. The PCB board shown in Figure D.2 is implemented for signal sensing and circuit protection for the dc-dc converter.

D.2 Prototype of Three-Phase Dc-Ac Inverter

The hardware prototype of the switching network in the three-phase dc-ac inverter is shown Figure D.3. The capacitance rating on the dc link capacitor is 680 µF. The three-phase LC filter in the three-phase dc-ac inverter is shown in Figure D.4. The inductance rating on the line inductor and the capacitance rating on the line-line capacitor are 0.276 mH and 8 µF, respectively. The PCB board shown in Figure D.5 is implemented for signal sensing and circuit protection for the dc-ac inverter.

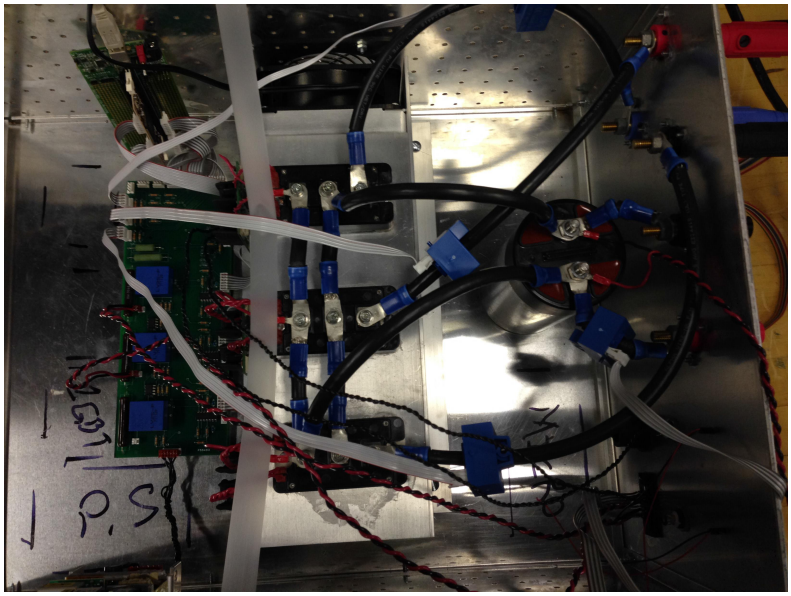

Figure D.3: Three-phase switching network.

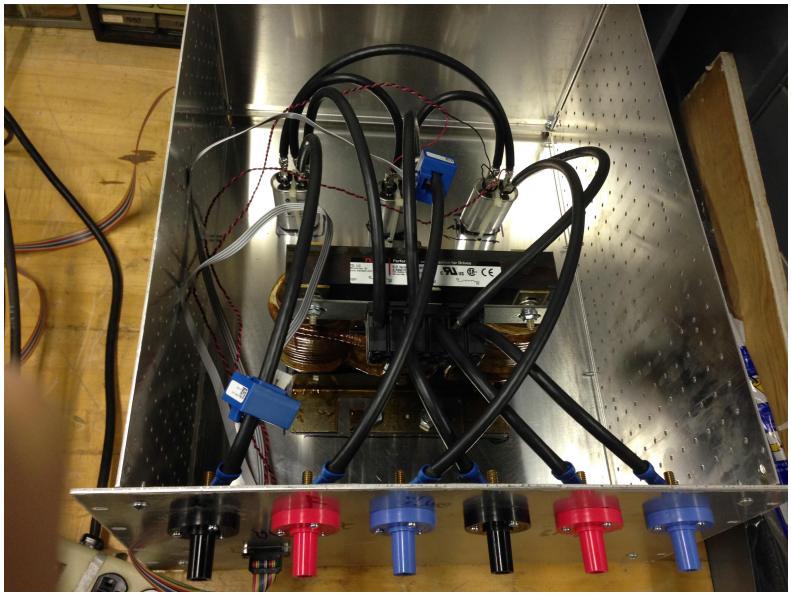

Figure D.4: Three-phase LC filter.

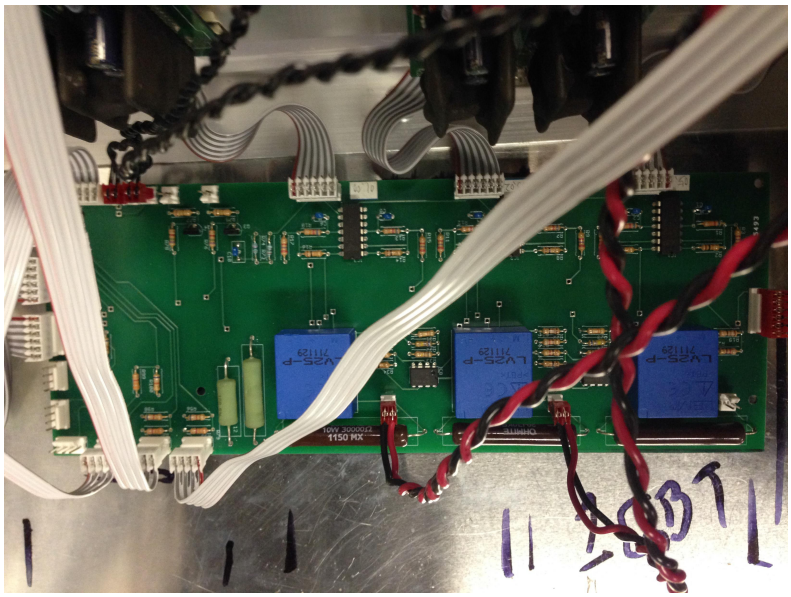

Figure D.5: PCB board.

REFERENCES

[1] H. Deng, X. Duan, N. Sun, Y. Ma, A. Q. Huang, and D. Chen, "Monolithically integrated boost converter based on 0.5 μm CMOS process," *IEEE Trans. Power Electron.*, vol. 20, no. 3, pp. 628–638, May 2005.

[2] C. Y. Leung, P. K. T. Mok, and K. N. Leung, "A 1 V integrated current-mode boost converter in standard 3.3/5-V CMOS technologies," *IEEE J. Solid-State Circuits*, vol. 40, no. 11, pp. 2265–2274, Nov. 2005.

[3] T. Y. Man, P. Mok, and M. J. Chan, "A 0.9 V input discontinuous-conduction-mode boost converter with CMOS-control rectifier," *IEEE J. Solid-State Circuits*, vol. 43, no. 9, pp. 2036–2046, Sept. 2008.

[4] Y. Nakase, S. Hirose, T. Goda, K. Hu, H. Onoda, Y. Ido, H. Kono, W. Kong, W. Zhang, T. Oishi, S. Mori, and T. Shimizu, "0.8 V start-up 92% efficiency on-chip boost dc-dc converters for battery operation micro-computers," in *2011 IEEE Asian Solid State Circuits Conf.*, Nov. 2011, pp. 21–24.

[5] S. Bandyopadhyay, Y. K. Ramadass, and A. P. Chandrakasan, "20 μA to 100 mA dc-dc converter with 2.8-4.2 V battery supply for portable applications in 45 nm CMOS," *IEEE J. Solid-State Circuits*, vol. 46, no. 12, pp. 2807–2820, Dec. 2011.

[6] J. R. de Britto, F. V. R. da Silva, E. A. A. Coelho, L. C. de Freitas, V. J. Farias, and J. B. Vieira, "Proposal of a dc-dc converter with wide conversion range used in photovoltaic systems and utility power grid for the universal voltage range," in *25th Annu. IEEE Appl. Power Electron. Conf. and Expo., 2010.*, Feb. 2010, pp. 2258–2263.

[7] J. T. Hawke, H. S. Krishnamoorthy, and P. N. Enjeti, "A new utility-scale power converter for large fuel cell power plants with individual stack power control," in *27th Annu. IEEE Appl. Power Electron. Conf. and Expo., 2012*, Feb. 2012, pp. 1482–1488.

[8] Y. Nishida, S. Nakamura, N. Aikawa, S. Sumiyoshi, H. Yamashita, and H. Omori, "A novel type of utility-interactive inverter for photovoltaic system," in *29th Annu. Conf. of the IEEE Ind. Electron. Soc., 2003.*, vol. 3, Nov. 2003, pp. 2338–2343.

[9] T. Shimizu, K. Wada, and N. Nakamura, "Flyback-type single-phase utility interactive inverter with power pulsation decoupling on the dc input for an ac photovoltaic module system," *IEEE Trans. Power Electron.*, vol. 21, no. 5, pp. 1264–1272, Sept. 2006.

[10] L. Liu, H. Li, Z. Wu, and Y. Zhou, "A cascaded photovoltaic system integrating segmented energy storages with self-regulating power allocation control and wide range reactive power compensation," *IEEE Trans. Power Electron.*, vol. 26, no. 12, pp. 3545–3559, Dec. 2011.

[11] S. Kim, M. H. Todorovic, and P. N. Enjeti, "Three-phase active harmonic rectifier (AHR) to improve utility input current THD in telecommunication power distribution system," *IEEE Trans. Ind. Appl.*, vol. 39, no. 5, pp. 1414–1421, Sept. 2003.

[12] R. W. Brockett and J. R. Wood, "Electrical networks containing controlled switches," *Addendum to IEEE Symp. on Circuit Theory*, Apr. 1974.

[13] R. D. Middlebrook and S. Ćuk, "A general unified approach to modeling switching power converters stages," in *Power Electron. Specialists Conf.*, 1976, pp. 18–34.

[14] C. T. Rim, G. B. Joung, and G. H. Cho, "A state-space modeling of nonideal dc-dc converters," in *Power Electron. Specialists Conf. Record*, Apr. 1988, pp. 943–950.

[15] M. Bilgic and M. Ehsani, "Analysis of inductor-converter bridge by means of state-space averaging technique (superconducting magnet energy storage)," in *Power Electron. Specialists Conf. Record*, Apr. 1988, pp. 116–121.

[16] V. Moreno-Font, A. El Aroudi, J. Calvente, R. Giral, and L. Benadero, "Dynamics and stability issues of a single-inductor dual-switching dc-dc converter," *IEEE Trans. Circuits Syst. I, Reg. Papers*, vol. 57, no. 2, pp. 415–426, 2010.

[17] J. Leppaaho and T. Suntio, "Dynamic characteristics of current-fed superbuck converter," *IEEE Trans. Power Electron.*, vol. 26, no. 1, pp. 200–209, 2011.

[18] J. Mahdavi, A. Emaadi, M. Bellar, and M. Ehsani, "Analysis of power electronic converters using the generalized state-space averaging approach," *IEEE Trans. Circuits Syst. I, Fundam. Theory Appl.*, vol. 44, no. 8, pp. 767–770, Aug. 1997.

[19] J. Xu and C. Q. Lee, "A unified averaging technique for the modeling of quasi-resonant converters," *IEEE Trans. Power Electron.*, vol. 13, no. 3, pp. 556–563, May. 1998.

[20] V. A. Caliskan, O. C. Verghese, and A. M. Stankovic, "Multifrequency averaging of dc/dc converters," *IEEE Trans. Power Electron.*, vol. 14, no. 1, pp. 124–133, Jan. 1999.

[21] J. W. van der Woude, W. L. de Koning, and Y. Fuad, "Stability aspects of a multifrequency model of a PWM converter," *Int. J. Control*, vol. 76, no. 3, pp. 309–317, 2003.

[22] A. Emadi, "Modeling and analysis of multiconverter dc power electronic systems using the generalized state-space averaging method," *IEEE Trans. Ind. Electron.*, vol. 51, no. 3, pp. 661–668, Jun. 2004.

[23] C. Gaviria, E. Fossas, and R. Grino, "Robust controller for a full-bridge rectifier using the IDA approach and GSSA modeling," *IEEE Trans. Circuits Syst. I, Reg. Papers*, vol. 52, no. 3, pp. 609–616, March 2005.

[24] Y. Chen, A. Davoudi, and P. L. Chapman, "Multifrequency modeling of a multiple-input dc-dc converter," in *IEEE Power Electron. Specialists Conf., 2008*, Jun. 2008, pp. 4604–4610.

[25] B. Puskaric, "Modeling of single phase four quadrant converter using a multifrequency averaging approach," in *35th Ann. Conf. of IEEE Ind. Electron., 2009*, Nov. 2009, pp. 639–644.

[26] Z. Ye, P. Jain, and P. Sen, "Phasor-domain modeling of resonant inverters for high-frequency ac power distribution systems," *IEEE Trans. Power Electron.*, vol. 24, no. 4, pp. 911–923, Apr. 2009.

[27] C. Bernal, E. Oyarbide, P. Molina, and A. Mediano, "Multi-frequency model of a single switch ZVS class E inverter," in *2010 IEEE Int. Symp. Ind. Electron.*, July 2010, pp. 939–944.

[28] R. Zhao, S.-Y. Yu, and A. Kwasinski, "Modeling of multiple-input dc-dc converters considering input-coupling effects," in *2011 IEEE Energ. Convers. Congr. and Expo.*, Sept. 2011, pp. 698–705.

[29] H. Behjati, L. Niu, A. Davoudi, and P. Chapman, "Alternative time-invariant multi-frequency modeling of PWM dc-dc converters," *IEEE Trans. Circuits Syst. I, Reg. Papers*, vol. 60, no. 11, pp. 3069–3079, 2013.

[30] S. Sanders, J. Noworolski, X. Liu, and G. Verghese, "Generalized averaging method for power conversion circuits," in *21st Annu. IEEE Power Electron. Specialists Conf., 1990*, 1990, pp. 333–340.

[31] J.-W. Jung and M. Hawksford, "An oversampled digital PWM linearization technique for digital-to-analog conversion," *IEEE Trans. Circuits Syst. I, Reg. Papers*, vol. 51, no. 9, pp. 1781–1789, 2004.

[32] D. VandeSype, K. DeGusseme, F. DeBelie, A. VandenBossche, and J. Melkebeek, "Small-signal z-domain analysis of digitally controlled converters," *IEEE Trans. Power Electron.*, vol. 21, no. 2, pp. 470–478, 2006.

[33] M. Hartmann, S. Round, H. Ertl, and J. Kolar, "Digital current controller for a 1 MHz, 10 kW three-phase Vienna rectifier," *IEEE Trans. Power Electron.*, vol. 24, no. 11, pp. 2496–2508, 2009.

[34] A. Syed, E. Ahmed, and D. Maksimovic, "Digital PWM controller with feedforward compensation," in *Nineteenth Annu. IEEE Appl. Power Electron. Conf. and Expo., 2004*, vol. 1, 2004, pp. 60–66.

[35] Z. Zhao and A. Prodic, "Continuous-time digital controller for high-frequency dc-dc converters," *IEEE Trans. Power Electron.*, vol. 23, no. 2, pp. 564 –573, Mar. 2008.

[36] S. Chattopadhyay and S. Das, "A digital current-mode control technique for dc-dc converters," *IEEE Trans. Power Electron.*, vol. 21, no. 6, pp. 1718–1726, Nov. 2006.

[37] X. Zhang and D. Maksimovic, "Multimode digital controller for synchronous buck converters operating over wide ranges of input voltages and load currents," *IEEE Trans. Power Electron.*, vol. 25, no. 8, pp. 1958–1965, Aug. 2010.

[38] M. Barai, S. SenGupta, and J. Biswas, "Digital controller for DVS-enabled dc-dc converter," *IEEE Trans. Power Electron.*, vol. 25, no. 3, pp. 557–573, Mar. 2010.

[39] J. A. Abu Qahouq and V. Arikatla, "Online closed-loop autotuning digital controller for switching power converters," *IEEE Trans. Ind. Electron.*, vol. 60, no. 5, pp. 1747–1758, May 2013.

[40] B. P. Loop, S. D. Sudhoff, S. H. Żak, and E. L. Zivi, "Estimating regions of asymptotic stability of power electronics systems using genetic algorithms," *IEEE Trans. Control Syst. Technol.*, vol. 18, no. 5, pp. 1011–1022, Sept. 2010.

[41] A. Griffo and J. Wang, "Large signal stability analysis of 'more electric' aircraft power systems with constant power loads," *IEEE Trans. Aerosp. Electron. Syst.*, vol. 48, no. 1, pp. 477–489, Jan. 2012.

[42] P. Magne, D. Marx, B. Nahid-Mobarakeh, and S. Pierfederici, "Large-signal stabilization of a dc-link supplying a constant power load using a virtual capacitor: Impact on the domain of attraction," *IEEE Trans. Ind. Appl.*, vol. 48, no. 3, pp. 878–887, May 2012.

[43] D. Marx, P. Magne, B. Nahid-Mobarakeh, S. Pierfederici, and B. Davat, "Large signal stability analysis tools in dc power systems with constant power loads and variable power loads—A review," *IEEE Trans. Power Electron.*, vol. 27, no. 4, pp. 1773–1787, Apr. 2012.

[44] W. Du, J. Zhang, Y. Zhang, and Z. Qian, "Stability criterion for cascaded system with constant power load," *IEEE Trans. Power Electron.*, vol. 28, no. 4, pp. 1843–1851, Apr. 2013.

[45] D. J. Packard, "Discrete modeling and analysis of switching regulators," Ph.D. dissertation, California Institute of Technology, Pasadena, Nov. 1976.

[46] G. C. Verghese, M. E. Elbuluk, and J. G. Kassakian, "A general approach to sampled-data modeling for power electronic circuits," *IEEE Trans. Power Electron.*, vol. PE-1, no. 2, pp. 76–89, Apr. 1986.

[47] F. Huliehel and S. Ben-Yaakov, "Low-frequency sampled-data models of switched mode dc-dc converters," *IEEE Trans. Power Electron.*, vol. 6, no. 1, pp. 55–61, Jan. 1991.

[48] J. G. Kassakian, M. F. Schlecht, and G. C. Verghese, *Principles of Power Electronics*. Boston, MA: Addison-Wesley, 1991.

[49] V. Rajasekaran, J. Sun, and B. S. Heck, "Bilinear discrete-time modeling for enhanced stability prediction and digital control design," *IEEE Trans. Power Electron.*, vol. 18, no. 1, pp. 381–389, Jan. 2003.

[50] D. Maksimovic and R. Zane, "Small-signal discrete-time modeling of digitally controlled pwm converters," *IEEE Trans. Power Electron.*, vol. 22, no. 6, pp. 2552–2556, Nov. 2007.

[51] S. R. Sanders and G. C. Verghese, "Lyapunov-based control for switched power converters," *IEEE Trans. Power Electron.*, vol. 7, no. 1, pp. 17–24, Jan. 1992.

[52] H. Sira-Ramirez and M. Prada-Rizzo, "Nonlinear feedback regulator design for the Ćuk converter," *IEEE Trans. Autom. Control*, vol. 37, no. 8, pp. 1173–1180, Aug. 1992.

[53] G. Escobar, R. Ortega, H. Sira-Ramirez, J. Vilain, and I. Zein, "An experimental comparison of several nonlinear controllers for power converters," *IEEE Trans. Control Syst.*, vol. 19, no. 1, pp. 66–82, Feb. 1999.

[54] C. Kranz, "Complete digital control method for pwm dcdc boost converter," in *34th Annu. IEEE Power Electron. Specialist Conf., 2003.*, vol. 2, Jun. 2003, pp. 951–956.

[55] M. Tajuddin, N. A. Rahim, I. Daut, B. Ismail, and M. F. Mohammed, "State space averaging technique of power converter with digital pid controller," in *IEEE Region 10 Conf., 2009.*, Jan. 2009, pp. 1–6.

[56] D. Maksimovic, A. M. Stankovic, V. J. Thottuvelil, and G. C. Verghese, "Modeling and simulation of power electronic converters," *Proceedings of the IEEE*, vol. 89, no. 6, pp. 898–912, Jun. 2001.

[57] R. Priewasser, M. Agostinelli, C. Unterrieder, S. Marsili, and M. Huemer, "Modeling, control, and implementation of dc-dc converters for variable frequency operation," *IEEE Trans. Power Electron.*, vol. 29, no. 1, pp. 287–301, Jan. 2014.

[58] F. C. Lee, "High-frequency quasi-resonant converter technologies," *Proceedings of the IEEE*, vol. 76, no. 4, pp. 377–390, Apr. 1988.

[59] J. Xu and C. Q. Lee, "A unified averaging technique for the modeling of quasi-resonant converters," *IEEE Trans. Power Electron.*, vol. 13, no. 3, pp. 556–563, May 1998.

[60] M. Jalla, A. Emadi, G. Williamson, and B. Fahimi, "Modeling of multiconverter more electric ship power systems using the generalized state space averaging method," in *30th Annu. Conf. IEEE Ind. Electron. Society*, vol. 1, Nov. 2004, pp. 508–513.

[61] Z. Lin and H. Ma, "Modeling and analysis of three-phase inverter based on generalized state space averaging method," in *39th Annu. Conf. IEEE Ind. Electron. Society*, Nov. 2013, pp. 1007–1012.

[62] A. Emadi, "Modeling of power electronic loads in ac distribution systems using the generalized state-space averaging method," *IEEE Trans. Ind. Electron.*, vol. 51, no. 5, pp. 992–1000, Oct. 2004.

[63] Y. Fuad, W. L. De Koning, and J. W. van der Woude, "On the stability of the pulsewidth-modulated Ćk converter," *IEEE Trans. Circuits Syst. II, Exp. Briefs*, vol. 51, no. 8, pp. 412–420, Aug. 2004.

[64] J. J. Rico, M. Madrigal, and E. Acha, "Dynamic harmonic evolution using the extended harmonic domain," *IEEE Trans. Power Del.*, vol. 18, no. 2, pp. 587–594, Apr. 2003.

[65] A. Stankovic, H. Lev-Ari, and M. Perisic, "Analysis and implementation of model-based linear estimation of dynamic phasors," *IEEE Transactions on Power Systems*, vol. 19, no. 4, pp. 1903–1910, Nov. 2004.

[66] J. A. d. de la Serna, "Dynamic phasor estimates for power system oscillations," *IEEE Trans. Instrum. Meas.*, vol. 56, no. 5, pp. 1648–1657, Oct. 2007.

[67] R. K. Mai, Z. Y. He, L. Fu, W. He, and Z. Q. Bo, "Dynamic phasor and frequency estimator for phasor measurement units," *IET Transm. Distrib. Gener.*, vol. 4, no. 1, pp. 73–83, Jan. 2010.

[68] R. W. Erickson and D. Maksimovic, *Fundamentals of Power Electronics*. Norwell, MA: Kluwer Academic, 2001.

[69] A. R. Brown and R. D. Middlebrook, "Sampled-data modeling of switching regulators," in *Proc. IEEE Power Electron. Spec. Conf.*, 1981, pp. 349–369.

[70] M. di Bernardo and F. Vasca, "Discrete-time maps for the analysis of bifurcations and chaos in dc/dc converters," *IEEE Trans. Circuits Syst. I, Fundam. Theory Appl.*, vol. 47, no. 2, pp. 130–143, Feb. 2000.

[71] J. H. B. Deane and D. C. Hamill, "Analysis, simulation and experimental study of chaos in the buck converter," in *21st Annu. IEEE Power Electron. Spec. Conf., 1990*, 1990, pp. 491–498.

[72] Y. Cho and J.-S. Lai, "Digital plug-in repetitive controller for single-phase bridgeless pfc converters," *IEEE Trans. Power Electron.*, vol. 28, no. 1, pp. 165–175, Jan. 2013.

[73] X. Zhang, J. W. Spencer, and J. M. Guerrero, "Small-signal modeling of digitally controlled grid-connected inverters with lcl filters," *IEEE Trans. Ind. Electron.*, vol. 60, no. 9, pp. 3752–3765, Sept. 2013.

[74] L. Corradini, E. Orietti, P. Mattavelli, and S. Saggini, "Digital hysteretic voltage-mode control for dc-dc converters based on asynchronous sampling," *IEEE Trans. Power Electron.*, vol. 24, no. 1, pp. 201–211, Jan. 2009.

[75] M. M. Peretz and S. Ben-Yaakov, "Time-domain design of digital compensators for pwm dc-dc converters," *IEEE Trans. Power Electron.*, vol. 27, no. 1, pp. 284–293, Jan. 2012.

[76] L. Corradini, A. Bjeletić, R. Zane, and D. Maksimović, "Fully digital hysteretic modulator for dc-dc switching converters," *IEEE Trans. Power Electron.*, vol. 26, no. 10, pp. 2969–2979, Oct. 2011.

[77] P. T. Krein, *Elements of Power Electronics.* New York, NY: Oxford University Press, 1991.

[78] A. P. Dancy, R. Amirtharajah, and A. P. Chandrakasan, "High-efficiency multiple-output dc-dc conversion for low-voltage systems," *IEEE Trans. Very Large Scale Integr. (VLSI) Syst.*, vol. 8, no. 3, pp. 252–263, Jun. 2000.

[79] A. V. Peterchev, J. Xiao, and S. R. Sanders, "Architecture and ic implementation of a digital vrm controller," *IEEE Trans. Power Electron.*, vol. 18, no. 1, pp. 356–364, Jan. 2003.

[80] P. Xu, J. Wei, and F. C. Lee, "Multiphase coupled-buck converter-a novel high efficient 12 V voltage regulator module," *IEEE Trans. Power Electron.*, vol. 18, no. 1, pp. 74–82, Jan. 2003.

[81] K. Jin, M. Xu, and F. C. Lee, "A switching-capacitor pwm dc-dc converter and its variations," *IEEE Trans. Power Electron.*, vol. 25, no. 1, pp. 24–32, Jan. 2010.

[82] G.-Y. Wei and M. Horowitz, "A low power switching power supply for self-clocked systems," in *Int. Symp. Low Power Electron. and Design*, Aug. 1996, pp. 313–317.

[83] L. Guo, "Implementation of digital PID controllers for dc-dc converters using digital signal processors," in *2007 IEEE Int. Conf. Electro/Inf. Technol.*, May 2007, pp. 306–311.

[84] S. Lee and J. Burm, "A dc-dc buck converter with using a digital PID regulator based on a simple control algorithm," in *2011 10th Int. Sym. Signals, Circuits and Systems*, Jul. 2011, pp. 1–4.

[85] R. R. Boudreaux and R. M. Nelms, "Simulation and modeling of a dc-dc converter controlled by an 8-bit microcontroller," in *Twelfth Annu. Appl. Power Electron. Conf. and Expo., 1997*, vol. 2, Feb. 1997, pp. 963–969.

[86] G. Walker and G. Ledwich, "Bandwidth considerations for multilevel converters," *IEEE Trans. Power Electron.*, vol. 14, no. 1, pp. 74–81, 1999.

[87] L. Dixon, *Average Current Mode Control of Switching Power Supply.* Texas Instruments Inc., 2001.

[88] J. Dudrik, M. Bodor, and V. Ruscin, "Zero-voltage and zero-current switching dc-dc converter with controlled output rectifier," in *14th Int. Power Electron. and Motion Control Conf., 2010*, Sept. 2010, pp. T1–39–T1–44.

[89] M. P. Kazmierkowski, M. Jasinski, and G. Wrona, "DSP-based control of grid-connected power converters operating under grid distortions," *IEEE Trans. Ind. Electron.*, vol. 7, no. 2, pp. 204–211, May 2011.

[90] C. Buccella, C. Cecati, and H. Latafat, "Digital control of power converters–A survey," *IEEE Trans. Ind. Informat.*, vol. 8, no. 3, pp. 437–447, Aug. 2012.

[91] M. Shahbazi, P. Poure, S. Saadate, and M. R. Zolghadri, "FPGA-based reconfigurable control for fault-tolerant back-to-back converter without redundancy," *IEEE Trans. Ind. Electron.*, vol. 60, no. 8, pp. 3360–3371, Aug. 2013.

[92] S. D. Sudhoff, K. A. Corzine, S. F. Glover, H. J. Hegner, and H. N. Robey, Jr., "DC link stabilized field oriented control of electric propulsion systems," *IEEE Trans. Energy Convers.*, vol. 13, no. 1, pp. 27–33, Mar. 1998.

[93] X. Feng, J. Liu, and F. C. Lee, "Impedance specifications for stable dc distributed power systems," *IEEE Trans. Power Electron.*, vol. 17, no. 2, pp. 157–162, Mar. 2002.

[94] S. D. Sudhoff and S. F. Glover, "Modeling techniques, stability, analysis, and design criteria for dc power systems with experimental validation," *Soc. Autom. Eng., J. Aerosp.*, vol. 107, no. 1, pp. 52–67, 1998.

[95] ——, "Three-dimensional stability analysis of dc power electronics based systems," in *31st Annu. IEEE Power Electron. Specialists Conf., 2000*, vol. 1, Jun. 2000, pp. 101–106.

[96] G. O. Kalcon, G. P. Adam, O. Anaya-Lara, S. Lo, and K. Uhlen, "Small-signal stability analysis of multi-terminal VSC-based dc transmission systems," *IEEE Trans. Power Electron.*, vol. 27, no. 4, pp. 1818–1830, Nov. 2012.

[97] S. Q. Bu, W. Du, H. F. Wang, Z. Chen, L. Y. Xiao, and H. F. Li, "Probabilistic analysis of small-signal stability of large-scale power systems as affected by penetration of wind generation," *IEEE Trans. Power Electron.*, vol. 27, no. 2, pp. 762–770, May 2012.

[98] T. Knüppel, J. N. Nielsen, K. H. Jensen, A. Dixon, and J. Ostergaard, "Small-signal stability of wind power system with full-load converter interfaced wind turbines," *IET Renew. Power Gen.*, vol. 6, no. 2, pp. 79–91, Mar. 2012.

[99] J. Lee, "An optimization-driven framework for the computation of the controlling UEP in transient stability analysis," *IEEE Trans. Autom. Control*, vol. 49, no. 1, pp. 115–119, Jan. 2004.

[100] H.-D. Chiang, *Direct Methods for Stability Analysis of Electric Power Systems: Theoretical Foundation, BCU Methodologies, and Applications.* New York, NY: Wiley, 2011.

[101] N. Yorino, E. Popov, Y. Zoka, Y. Sasaki, and H. Sugihara, "An application of critical trajectory method to BCU problem for transient stability studies," *IEEE Trans. Power Sys.*, vol. 28, no. 4, pp. 4237–4244, Nov. 2013.

[102] S. K. Mazumder, A. Nayfeh, and D. Borojevic, "A nonlinear approach to the analysis of stability and dynamics of standalone and parallel dc-dc converters," in *16th Annu. IEEE Appl. Power Electron. Conf. Expo., 2001*, vol. 2, Mar. 2001, pp. 784–790.

[103] A. Davoudi and J. Jatskevich, "Parasitics realization in state-space average-value modeling of PWM dc-dc converters using an equal area method," *IEEE Trans. Circuits Syst. I, Reg. Papers*, vol. 54, no. 9, pp. 1960–1967, 2007.

[104] R. Lai, F. Wang, R. Burgos, D. Boroyevich, D. Jiang, and D. Zhang, "Average modeling and control design for Vienna-type rectifiers considering the dc-link voltage balance," *IEEE Trans. Power Electron.*, vol. 24, no. 11, pp. 2509–2522, 2009.

[105] S. Sudhoff, B. Loop, J. Byoun, and A. Cramer, "A new procedure for calculating immittance characteristics using detailed computer simulations," in *IEEE Power Electron. Spec. Conf., 2007*, 2007, pp. 901–908.

[106] P. J. Antsaklis and A. N. Michel, *Linear Systems.* New York: McGraw-Hill, 1997.

[107] T. Hu, A. Teel, and L. Zaccarian, "Stability and performance for saturated systems via quadratic and nonquadratic lyapunov functions," *IEEE Trans. Autom. Control*, vol. 51, no. 11, pp. 1770–1786, Nov. 2006.

[108] M. Anghel, F. Milano, and A. Papachristodoulou, "Algorithmic construction of lyapunov functions for power system stability analysis," *IEEE Trans. Circuits and Syst. I: Reg. Papers*, vol. 60, no. 9, pp. 2533–2546, Sept. 2013.

[109] B. P. Loop, "Estimating regions of asymptotic stability of nonlinear systems with applications to power electronics systems," Ph.D. dissertation, Dept. Elect. Comput. Eng., Purdue Univ., West Lafayette, IN, 2005.

[110] H. Schwefel, *Evolution and Optimum Seeking.* New York, NY: Wiley, 1995.

[111] F. Pan and A. M. Cramer, "Reduced-order multifrequency averaging in naturally sampled pwm converters," in *2014 IEEE Energy Convers. Congress Expo.*, Sep. 2014.

[112] P. V. Kokotović, H. K. Khalil, and J. O'Reilly, *Singular Perturbation Methods in Control: Analysis and Design.* London, U.K.: Academic, 1986.

[113] K. Yao, K. Lee, M. Xu, and F. Lee, "Optimal design of the active droop control method for the transient response," in *IEEE Appl. Power Electron. Conf. and Expo., 2003*, vol. 2, 2003, pp. 718–723.

[114] S. Mishra, "Design-oriented analysis of modern active droop-controlled power supplies," *IEEE Trans. Ind. Electron.*, vol. 56, no. 9, pp. 3704–3708, Sept. 2009.

[115] Y. Yan, P.-H. Liu, and F. Lee, "Small signal analysis and design of active droop control using current mode equivalent circuit model," in *IEEE Appl. Power Electron. Conf. and Expo., 2014*, Mar. 2014, pp. 2809–2816.

[116] Y. Lee and S. D. Sudhoff, *Genetic optimization and system engineering tool (GOSET) ver. 2.6 manual*, Sch. Elect. Comput. Eng., Purdue Univ., West Lafayette, IN, 2014.

[117] B. Patella, A. Prodic, A. Zirger, and D. Maksimovic, "High-frequency digital pwm controller ic for dc-dc converters," *IEEE Transactions on Power Electronics*, vol. 18, no. 1, pp. 438–446, 2003.

[118] G. F. Franklin, J. D. Powell, and M. L. Workman, *Digital Control of Dynamic Systems.* Ellis-Kagle Press, 2006.

[119] R. A. Horn and C. R. Johnson, *Topics in Matrix Analysis.* Cambridge, UK: Cambridge University Press, 1991.

VITA

Fei Pan received his B.S. in electrical engineering from Southeast University in 2008. He was with the Advanced Photonics Center (APC) at Southeast University from 2008 to 2010. Since then he has pursued a Ph.D. in electrical engineering at University of Kentucky. His research interests include power electronics, power systems, and controls.